Sonja Hartner

Electrical properties of gas-phase synthesized nanoparticles

Cuvillier Verlag Göttingen
Internationaler wissenschaftlicher Fachverlag

Electrical properties of gas-phase synthesized nanoparticles

Electrical properties of gas-phase synthesized nanoparticles

Der Fakultät für Ingenieurwissenschaften, Abteilung Maschinenbau und Verfahrenstechnik der

Universität Duisburg-Essen

zur Erlangung des akademischen Grades

einer

Doktorin der Ingenieurwissenschaften

Dr.-Ing.

genehmigte Dissertation

von

Sonja Hartner
aus
Dinslaken

Referent: Prof. Dr. Christof Schulz
Korreferent: Prof. Dr. Roland Schmechel
Tag der mündlichen Prüfung: 07.05.2012

Bibliografische Information der Deutschen Nationalbibliothek
Die Deutsche Nationalbibliothek verzeichnet diese Publikation in der Deutschen Nationalbibliografie; detaillierte bibliografische Daten sind im Internet über http://dnb.d-nb.de abrufbar.

1. Aufl. - Göttingen: Cuvillier, 2012
Zugl.: Duisburg-Essen, Univ., Diss., 2012

978-3-95404-221-0

Nonnenstieg 8, 37075 Göttingen
Telefon: 0551-54724-0
Telefax: 0551-54724-21
www.cuvillier.de

1. Auflage, 2012
Gedruckt auf säurefreiem Papier

978-3-95404-221-0

Abstract

Zinc oxide (ZnO) doped with aluminum receives increasing attention for being an alternative material for the established but much more expensive indium tin oxide (ITO) due to the fact, that it has comparable electrical and optical properties. The electrical properties of mechanically compacted pellets prepared from nanosized ZnO powders are investigated using impedance spectroscopy. The impedance of the samples is measured in hydrogen and in synthetic air between room temperature and 400°C. In both atmospheres, the measurements show two different electrical transport processes depending on the temperature and the doping level. In synthetic air, the conductivity increases for doping concentrations up to 7.74% of aluminum and collapses for higher doping levels. In hydrogen atmosphere, the conductivity decreases with rising doping level of Al. This behavior can be explained by generation of free charge carriers due to the incorporation of hydrogen and doping with aluminum, respectively. At higher temperatures and at high doping concentrations, scattering processes at grain boundaries as well as lattice defects increasingly affect the charge carrier transport processes leading to a decreasing overall conductivity. The electrical conductivity shows reversible behavior when the atmosphere is changed from hydrogen to ambient conditions and back.
To replace ITO in applications, transparent conductive layers with good electrical and optical properties are required. ZnO dispersions are prepared and printed on pre-structured substrates by ink-jet printing to investigate the electrical and sensing properties of printed films. The properties are measured without any annealing steps from room temperature up to 200°C in ambient conditions and in hydrogen atmosphere using impedance spectroscopy. Compared to the measurements in air, the resistance in hydrogen decreases by a factor of five even at room temperature. The ink-jet printed ZnO films with nanosized particles can be used as sensor without any annealing or post-processing for sensing.

Silicon (Si) nanoparticles are envisioned for a broad range of applications, ranging from electroluminescent devices over biomarkers and lithium ion batteries to solar cells. One of the major challenges with respect to these applications is to effectively stabilize the silicon particles against oxidation. Electrical properties of as-prepared as well as functionalized silicon nanoparticles are investigated. The native oxide shell of the as-prepared silicon nanoparticles is removed and the electrical properties are measured and a re-oxidation of the silicon nanoparticles can be observed after a few hours. A fast and efficient process to functionalize silicon nanoparticles with n-alkenes is introduced. The freshly etched particles are subsequently grafted with even-numbered n-alkenes from C_6 to C_{18} in order to prevent the particles from re-oxidation. FTIR spectra are used to confirm the successful attachment of the organic molecules and provide insight into the binding mechanism. Electrical properties are investigated by impedance spectroscopy showing the effect of surface functionalization on the conductivity of compacted nanoparticle ensembles. It is observed that particles covered with alkenes from C_6 to C_{12} exhibit higher conductivity than the as-prepared materials, while surface functionalization with C_{14} and higher leads to almost insulating nanoparticle arrays. Despite freshly etched silicon nanoparticles, dodecene-terminated particles showed the best conductivity as well as a very good long-term stability against oxidation. FTIR spectroscopy indicated that particles stabilized with C_6 to C_{10} are less stable due to a creeping re-oxidation. The most promising results is the functionalization of silicon nanoparticles with alkenes with twelve carbon atoms (C_{12}). A variable range hopping transport mechanism or a charge carrier limited transport mechanism exist for all silicon nanoparticles. Especially for the functionalized particles, a dependence of the hopping distances can be observed. This does not mean that the charge carriers use the shortest way but the energetically most advantageous.

Kurzzusammenfassung

Zur Zeit wird Zinkoxid (ZnO) als aussichtsreicher Kandidat zum Ersatz des sehr teuren Indium Zinn Oxids (ITO) angesehen, da es vergleichbare elektrische und optische Eigenschaften zum ITO besitzt. Die elektrischen Eigenschaften von mechanisch kompaktierten Formkörpern aus ZnO-Nanopartikeln werden mittels der Impedanzspektroskopie untersucht. Die Impedanz der Proben wird in Wasserstoffatmosphäre und synthetischer Luft bis hin zu 400°C untersucht. Die Messungen in Wasserstoffumgebung und synthetischer Luft zeigen unterschiedliche Ergebnisse, abhängig von Temperatur und Dotierkonzentration. In synthetischer Luft steigt die Leitfähigkeit bis zu einer Dotierkonzentration mit Aluminium (Al) von 7,7% an und bricht für höhere Al-Konzentrationen ein. Unter Wasserstoffatmosphäre sinkt die Leitfähigkeit mit zunehmender Al-Dotierkonzentration. Dieses Verhalten kann mit einer Bildung von freien Ladungsträgern aufgrund der Wasserstoffdotierung aus der Umgebung und der entsprechend ansteigenden Al-Konzentration erklärt werden. Zu höheren Temperaturen und Dotierkonzentrationen treten vermehrt Stoßprozesse an Korngrenzen und Gitterdefekten auf, die den Transport der Ladungsträger unterbrechen. Die unterschiedliche Leitfähigkeit zeigt reversibles Verhalten, wenn von Wasserstoffatmosphäre zu synthetischer Luft und zurück gewechselt wird.

Für die Anwendung von ZnO für transparent leitfähige Filme und Sensoren aus kostengünstigen Materialien, werden stabile Dispersionen mit sehr kleinen (halb-) leitenden Partikeln im Nanometerbereich benötigt. Stabile ZnO-Dispersionen wurden hergestellt und auf vorstrukturierte Substrate mittels Ink-Jet Druckverfahren aufgebracht. Die elektrischen Senoreigenschaften der gedruckten Schichten wurden bis 200°C in Umgebungsluft vermessen. Vor den Impedanzmessungen wurden die Schichten nicht ausgeheilt. Verglichen zu den Messungen in Luft wurde beobachtet, dass sich der Widerstand der Schicht unter Wasserstoffatmosphäre bei Raumtemperatur um einen Faktor von fünf reduziert. Die hergestellten, gedruck-

ten ZnO-Schichten zeigen ein gutes Anprechverhalten auf Wasserstoff und sind ohne vorherige Ausheilprozesse zu verwenden.

Siliziumpartikel werden gegenwärtig für eine Vielzahl an Anwendungen benutzt. Diese Anwendungen reichen von elektrolumineszierenden Bauteilen über Biomarker und Lithium-Ionen Batterien bis hin zu Solarzellen. Eine der Aufgaben zur Verbesserung der Eigenschaften ist das Auffinden einer Methode zur Stabilisierung der Siliziumoberfläche gegen die Oxidation. Die vorhandene Oxidhülle um das Siliziumnanopartikel nach der Synthese wird entfernt. Die elektrischen Eigenschaften der frisch geätzen Partikel werden gemessen und eine schnelle Reoxidation der Partikel wird innerhalb von Stunden beobachtet. Ein schneller und effektiver Prozess zur Funktionalisierung mit n-Alkenen wird vorgestellt. Die Partikel werden mit unterschiedlich langen Alkenen von C_6 bis C_{18} präpariert um eine Reoxidation der Partikel nach dem Ätzprozess zu verhindern. Mit Hilfe von FTIR Messungen wird die erfolgreiche Anbringung der organischen Moleküle an die Siliziumoberfläche gezeigt. Elektrische Messungen werden mittels der Impedanzspektroskopie durchgeführt, um den Effekt der Funktionalisierung mit den unterschiedlichen Alkenen auf die elektrische Leitfähigkeit hin zu untersuchen. Es zeigt sich eine höhere Leitfähigkeit für alle Siliziumnanopartikel die mit den Alkenen von C_6 bis C_{12} funktionalisiert werden. Die Partikel, die mit Alkenen von einer Kettenlänge von C_{14} und höher funktionalisiert werden, zeigen eine sehr niedrige Leitfähigkeit, die teilweise schlechter als die von den Silizium Partikeln im Ursprungszustand ist. Die Funktionalisierung mit dem Alken C_{12} zeigt die besten Ergebnisse und ist auch nach über einen halben Jahr in den elektrischen Eigenschaften stabil. Mit FTIR Messungen wird gezeigt, dass die Partikel, die mit C_6 und C_{10} funktionalisiert werden, keine vollständige Stabilität gegen Reoxidation besitzen. Die Funktionalisierung von Silizium mit Dodecen ist am stabilsten gegenüber Reoxidation und zeigt die besten elektrischen Eigenschaften. Es ist ein "variable range hopping" Transportmechanimus für die Ladungsträger zwischen den Partikeln zu beobachten. Besonders für die funktionalisierten Partikel ist die zurückgelegte Distanz der Ladungsträger abhängig von der Art der Funktionalisierung. Dies bedeutet aber nicht, dass der Ladungsträger den kürzesten Weg nimmt, sondern den energetisch günstigsten.

Nomenclature of used symbols, abbreviation and acronyms

α	Spatial extension of the wave function
β_c	Frequency function for collisions
Γ	Degree of crystallinity
λ	Wavelength
λ	Dimensionless constant
μ_c	Chemical potential
μ	Mobility
$\omega{=}2\pi f$	Angular frequency
ϕ	Phase
ρ	Specific conductivity

σ	Specific electric conductivity
τ_c	Time to reduce number of the density of nanoparticles to the half of the initial value
$\tau_{e,h}$	Relaxation time
θ	Angle
Al	Aluminum
AZO	Aluminum doped ZnO
B	Background signal
CVS	Chemical vapor synthesis
d_{NP}	Primary particle diameter
D_0	Self diffusion coefficient
DEZn	Diethylzinc
DLS	Dynamic light scattering
e^-	Free electron
E_{Hop}	Hopping energy
E_A	Activation energy
EBL	Electron beam lithography
E	Energy
E_g	Band gap energy
EPR	Electron paramagnetic resonance

E_{S}	Surface energy
f*(E, T)*	Fermi level
FTIR	Fourier transformed infrared spectroscopy
HF	Hydrofluoric acid
I	Current
I_0	Current amplitude
ITO	Indium tin oxide
I_{t}	Exication current signal
j	Electrical current density
J	Signal from coherent scattering
k_{B}	Boltzmann constant
l	Average pathlenght between collision or scattering processes
m_{e}	Mass for electrons
m_{h}	Mass for electronic vacancies
n	Charge carrier concentration
N	Number of density of particles
N_{EF}	Density of local states
ntc	Negative temperature coefficient
$\mathrm{OH_o}$	Hydroxyl group on oxygen lattice site
$\mathrm{O_o}$	Oxygen atom on oxygen lattice site

p	Particle pressure
p_{s}	Equilibrium vapor pressure
ptc	Positive temperature coefficient
PVDF	Polyvinylidenfluorid
R_{const}	Universal gas constant
R	Resistivity
r	Hydrodynamic radius
R_{Hop}	Hopping distance
R_0	Resistivity in ambient atmosphere
r_{c}	Critical cluster size
RC	Resistivity-capacity
R_{gas}	Resistivity in gas
rH	Relative humidity
S	Sensitivity
SEM	Secondary electron microscopy
Si-NP	Silicon nanoparticles
T	Temperature
TEAl	Triethylaluminum
TEGO	Polyacrylic acid+sodium polyacrylate

TEM	Transmission electron microscopy
U	Voltage
U_0	Amplitude of voltage
U_t	Exication voltage signal
UV-Vis	Ultraviolet to visible spectroscopy
v_D	Drift velocity
v_m	Molar volume
VRH	Variable range hopping
v_th	Thermal velocity
XRD	X-ray-diffraction
ZnO	Zinc oxide
$\mathrm{Zn_{Zn}}$	Zinc atom on zinc lattice site

Contents

Acknowledgement

Ein sehr lehrreicher Teil meines Lebens geht zu Ende und ich habe immer noch das Gefühl als hätte ich erst gestern mit meiner Doktorarbeit angefangen. Ich möchte einigen Personen danken, die mich während dieser zeitlich fachlich wie auch privat sehr unterstützt haben.

Prof. Dr. Christof Schulz danke ich für die Aufnahme in seine Arbeitsgruppe und auch für die Möglichkeit bei ihm zu promovieren. Die unglaubliche Anzahl an Forschungsgebieten und die damit verbundene technische und personelle Ausstattung ist ein wichtiger Grund warum diese Arbeit in dieser Zeit und Form überhaupt möglich war. Außerdem danke ich ihm für die rekordverdächtige Schnelligkeit beim Antworten auf E-Mails und Lösen von Problemen.

Bei Herrn *Dr. Hartmut Wiggers* bedanke ich mich für das Vertrauen, dass er in mich als damalige Studentin hatte und mir schon während meines Physikstudiums die komplette Impedanzspektroskopie der Nanopartikel überlassen hat. Die Zeit war sehr lehrreich und hat mir gezeigt, dass ich sehr viel mehr schaffen kann, wenn ich mir selbst zutraue. Außerdem hat er die Betreuung dieser Arbeit fachlich übernommen und die Diskussionen zwischen einem Chemiker und einer Physikerin, die bei mir oftmals für viele Fragezeichen gesorgt haben, möchte ich nicht missen.

Am allermeisten danke ich ihm aber auch Prof. Schulz dafür, dass ich eine enorme Anzahl an internationalen Fachtagungen, insbesondere im Ausland, besuchen durfte, die mich fachlich aber auch persönlich sehr viel weiter gebracht haben. Manchmal hatte ich dass Gefühl, mehr Zeit in Hotelzimmern zu verbringen als in meiner eigenen Wohnung.

An *Frau Rosa Abts* kommt keine andere Sekretärin heran. Sie ist einfach unschlagbar in der Schnelligkeit und Genauigkeit ihrer Arbeit und dabei strahlt sie

auch noch soviel Freude und Spaß aus, dass man gleich bessere Laune hat wenn man in ihrem Büro vorbei kommt.

Es gibt ein paar Kollegen die bleibenden Einfluss auf mich hatten. Die wichtigsten sind mit Sicherheit Pascal Ifeacho, Anoop Gupta, Ingo Plümel und Moazzam Ali.
Pascal, deine Art und Weise an Dinge heranzugehen und die Ermutigung mich an Neues und vielleicht auch manchmal nicht gewolltes oder als hoffnungslos geltendes trotzdem heranzuwagen.
Ingo, ohne dich hätte ich bei so manchem Makro oder Labviewproblem wahrscheinlich schon nach kurzer Zeit einfach gekündigt. Dein breites Wissen in allen möglichen Gebieten des Programmierens ist unglaublich und du erledigst alles immer so schnell und unauffällig, dass man meinen könnte, wir hätten Zwerge im Labor, die Nachts für uns die Probleme lösen.
Anoop, I didn´t get anything at the beginning you were talking about. You had a terrible Indian accent and the speed you talked was amazing and it was hard to get what you were talking about. After a while, you spoke slower or my English got better and at the end we were joking and talking the whole time about everything. Working with you was fun and I have still not forgiven you the nasty April fools you played with me. I am also thankful that I had the opportunity to attend your marriage in Kanpur. In these very few days in India I learned to see the world with completely different eyes. Something is really missing since you left to BASF.
Moazzam, the cooperation with you was so much fun and the celebrations with cookies and coffee after we achieved something was great (everybody who needs a good coffee should go to the group of Prof. Winterer!).
I am thankful to *Prof. Winterer* who gave me the opportunity to use the material of his group and to use parts of the equipment of his group.
The idea of ink-jet printing on a sensor happened more or less by accident, because I thought *Dr. Ahmed Khalil* is somebody else than Ahmed Khalil.

Außerdem danke ich allen anderen Personen, die mich in meiner Arbeit unterstützt haben, indem sie Messungen oder Partikel für mich hergestellt haben. Insbesondere sind da *Nils Petermann* (Synthese und Chilli), *Robert Bywalez* (Funktionalisierung) und *Ervin Mehmedovic* (Presse) zu erwähnen, aber vor allem auch

mein RISE-Student *Clay Hopes* und mein Arbeitsehemann, dem Studenten *Adrian Münzer* (inzwischen B.Sc.). *Helge*, ohne deine Schokovorräte wäre ich ein Strich in der Landschaft. Bleib so wie du bist.
Ashrina, I really enjoyed to help you with every little thing and I will never forget the day we bought your carpet. I admire the way you live your life and someday I will come to visit you when you are back home in Malaysia.
Allen, die ich vergessen habe, danke ich natürlich auch, aber niemand liest sich 10 Seiten Danksagung durch.

Natürlich gibt es auch noch eine Welt außerhalb der Uni und auch den Personen die mich dort begleitet haben möchte ich danken. Hierzu gehören vor allem *Bernadette Hitzbleck* und *Nathalie Reckers*, die beide auf ihre unterschiedliche Art und Weise mich zum Lachen und vor allem Shoppen gebracht haben. Dazu gehören nun mal auch schlaflose Nächte an einem durch Schneefall gesperrten Londoner Flughafen und Salzwasser gebeutelte Planscherinnen.

Ingo, mit Dir die Zeit auch außerhalb der Uni zu verbringen ist das allerschönste. Für deine Ehrlichkeit, Direktheit und das Vertrauen kann ich dir nicht genug dankbar sein. *Mama, Papa und Martin*, ich bin Stolz eine so tolle Familie zu haben. Mama und Papa, ich bin euch Beiden unendlich dankbar mich meine Wege gehen zu lassen auch wenn ihr sie vielleicht nicht immer nachvollziehen könnt.

Duisburg, 25.01.12
Sonja Hartner

1 Introduction

The development of innovative materials is an essential part of modern research. In the recent years, researchers have been looking intensively at the use of nanomaterials due to their outstanding chemical and physical properties compared to bulk material. Today, nanostructured materials are already used, e.g., in lithium ion batteries to improve the energy storage capacity compared to batteries consisting of conventional material [1] . The influence of nanostructured materials in our lives shows a publication of ScienceDaily [2] where a rate of up to four new applications each week based on nanotechnology is announced.

Nanoparticles are nanomaterials with a size below 100 nm in all three dimensions. In this regime, many physical properties are size-dependent such as, e.g., the optical properties of silicon nanoparticles due to the quantum confinement. Also, the chemical reactivity increases with decreasing size due to the larger specific surface area and the particles are more affected by forces on the surface (van-der-Waals forces). The main focus of this work lies on the electrical properties of two nanomaterials systems, zinc oxide (ZnO) and silicon (Si) nanoparticles, to investigate their possible application in electronic devices.

Transparent conductive oxides (TCO) are optically transparent and electrically conductive. They are used as light transmitting electrodes in thin-film solar cells or flat-panel displays. Indium tin oxide (ITO) and ZnO are the most frequently used TCO materials for electronic applications but ITO is expensive due to the cost of the rarely available indium [3, 4]. In order to obtain cheaper devices, indium must be replaced by more abundant and therefore less expensive material with comparable optical and electrical properties [5–7]. For replacing ITO, aluminum-doped ZnO is the most promising alternative [8–11]. ZnO is a non-toxic material with a direct band gap of 3.37 eV [12] and the missing absorbance of visible light makes this material one of the best TCOs so far [9]. By using ZnO nanoparticles, it is possible to tune the optical and electrical properties in a wide range.

The optoelectronic properties of this material were investigated for progresses in light emitting diodes [13, 14], liquid crystal displays [15] or solar cells [4, 16, 17]. Also, the benefits of the large surface-to-volume ratio of the ZnO nanoparticles, which makes them a promising material for gas sensors [18, 19] and interesting for catalysis applications [14], were extensively studied. However, the electrical properties have not yet been investigated in detail. Therefore, the first part of this work aims at the characterization of the electrical transport mechanisms of ZnO nanoparticle-networks (powders). As application example, electronic devices made of ZnO nanoparticles are produced via ink-jet printing and tested. The raw ZnO nanoparticles are synthesized in the gas phase which provides control of the materials properties such as size and structural properties. Gas-phase synthesis also allows to synthesize large amounts of materials which is important to study subsequent processing steps.

The electronic properties of ZnO nanoparticles are investigated regarding doping, variable atmosphere, temperature and the influence of moisture. The resistivity can be changed by using doping by aluminum and the response of the material to different gases depends on the Al-doping level. The influence of moisture on the electrical behavior of ZnO is well known, but the influence of moisture on structural changes to the particulate material and the subsequent effect on the electrical behavior has not been investigated so far. Because this is crucial for practical applications, the respective effects have been studied in this thesis. Printable electronics made from nanoparticles enable printing of films on large areas at low cost, but only a few reports can be found for ZnO nanoparticles [20–22]

The second materials system used in this work are silicon nanoparticles. Silicon is one of the most abundant materials in the world and has the high advantage of biocompatibility and that it is already well established in the microelectronics technology [23]. One of the research fields with silicon nanoparticles are solar cells [24, 25], silicon-based lasers [26] and light-emitting diodes [27]. The electrical investigation for Si nanoparticles is rare due to the fact of the bad conductivity of the Si nanoparticles because of their stable oxide shell. It is known that the conductivity for etched Si nanoparticles is much higher but the particles have an

affinity to oxidation and a stable surface functionalization to conserve the optical and electrical properties of etched Si nanoparticles has not been found yet. Because of this, the third aim of this work is to characterize the electrical properties of silicon nanoparticles with different surface morphologies. As-prepared, etched and functionalized Si nanoparticles are investigated with a focus on the influence of the oxide shell and the lengths of organic molecules and the temporal stability of the different surface configurations. In this thesis, the Si particles are functionalized with different long-chain alkenes after the oxide shell has been removed by etching. The stability in air and the long-term stability of the functionalized Si nanoparticles are investigated and the activation energies for the transport processes of the charge carriers are calculated and compared with the thickness of the surface coverage (oxide shell or organic alkenes) and the hopping distances of the charge carriers.

2 State of the art

Semiconducting ZnO nanoparticles could be an alternative for ITO due to the stability in ambient air. ZnO is already used for a wide range of applications such as an additive in rubber [28], varistors [29], piezoelectric transducers [17], pigments in paint and suntan lotion [28, 30]. It is known, that the conductivity of aluminum doped ZnO (AZO) nanoparticles increases with higher Al content in ambient atmopshere and that the conductivity in hydrogen is even higher [31] but a detailed investigation of powders or thin films in different gases and temperature ranges is missing. In this work, the influence of the gaseous environment and the temperature-dependent conductivity of AZO nanoparticles synthesized by chemical vapor synthesis (CVS) in general are investigated. The stability of ZnO nanoparticles in ambient conditions were investigated by Ali et. al [32], having a view on the growth of ZnO nanoparticles with time. They found a significant growth of the ZnO nanoparticles in ambient conditions depending on the moisture concentration of the environment. The changing electrical properties which depend on the moisture concentration and the growth of the ZnO nanoparticles in moisture are therefore also investigated in the present work. This is done by using ZnO nanoparticles synthesized by the same route and having a similar size of about 12 nm. Another important part of this work is the production of a hydrogen sensitive ZnO thin film produced by ink-jet printing. The ink-jet printing method is already established for the production of diodes and light emitters [33, 34]. The method has some advantages compared to the preparation of thin films produced by magnetron sputtering [35] or spray pyrolysis [36]. The ink-jet printed ZnO films do not need any post-annealing and the ink-jet printing process does not require any high vacuum conditions. Also it is a very precise, selective deposition technique for particle dispersions. The selective deposition makes it possible to get well-defined patterns and structures of the ZnO film out of a dispersion and the waste of ZnO dispersion is strongly decreased compared for example with the

doctor-blade method [37]. Up to now, there are only very few publications [38] about ZnO based gassensors. Shen et al. used the ink-jet printing method to print ZnO films. The influence of the amount of different layers on the sensitivty of acetone was investigated. They found that the resistivity decreases with more ZnO layers, but the best sensitivity was found for four layers of ZnO. In this thesis it will be shown that it is possible to produce gassensors based on ZnO nanoparticles prepared by ink-jet printing which do not need any post annealing.

The second material used in this work are silicon nanoparticles synthesized in a microwave plasma reactor. The interest in silicon is resonable because it is the second most abundant element on earth and it is the best established material for the use in electronics devices [39]. It is highly available and also non-toxic. Silicon nanoparticles could increase the effectiveness of the applications in solar cells, silicon based lasers or diodes [24, 26, 27, 40, 41]. They have a big surface area and the defect concentration is high [42, 43]. The oxide shell around the silicon core decreases the electrical conductivity and the optical properties of the silicon nanoparticles [44–46] are limited. By removing this oxide shell with hydrofluoric acid the optical and electrical properties can be changed [47–50]. The problem of the hydrosilylation is the reoxidation of the surface and a method to prevent the reoxidation has to be found [51]. The functionalization with organic molecules was done by several groups before [52–56]. The silicon carbon bonds (Si-C) have a strong bonding and a low polarity [48, 57]. The optical properties of these functionalized silicon nanoparticles were already investigated deeply but the electrical properties are quite unknown. The functionalization with dodecene and octene up to 300°C are investigated by Nelles et al. [58]. Their silicon films have a thermally activated conductivity process between 7°C and 156°C which depends on the thickness and polarity of the molecules used for the functionalization. The conductivities of functionalized silicon nanoparticles are decreased to the as-prepared and etched particles which is completely different to our results.

The objective of this work is to find out the electrical properties for ZnO and silicon nanoparticles in different conditions and the properties of ink-jet printed ZnO. The particles are all synthesized from the gas-phase. The ZnO nanoparticles are synthesized via chemical vapor synthesis (CVS) in a hotwall reactor while the

silicon nanoparticles are synthesized also with CVS but in a microwave plasma reactor. The ZnO nanoparticles are prepared after the synthesis by producing a pellet consisting of compacted powder. The ZnO pellets are investigated by considering the aluminum doping, influence of changing humidity concentrations and the behavior of the electrical properties in different gaseous environments. From another part of the ZnO nanoparticles a stable dispersion is produced to perfom ink-jet printing of a thin film on an interdigital structure. The ink-jet printed film is tested with respect to its sensing properties in hydrogen atmosphere. To support the findings, additional measurements like x-ray diffraction (XRD) are performed. The main aim of the investigation of the silicon nanoparticles is the characterization of their electronic properties dependent on the type of preparation. The silicon nanoparticles are etched and functionalized with alkenes of different lenghts. To explain the findings of the electrical measurements, Fourier transformed spectroscopy (FTIR) and some other additional measurements (XRD, SEM) are also performed. The most important theory needed to understand the mechanisms are explained in the theory, chapter 3. The electrical properties of the ZnO are explained in chapter 4. The results for the ink-jet printed ZnO can be found in chapter 5 and for the silicon nanoparticles in chapter 6.

3 Theory and experimental methologies

3.1 Charge carrier transport in semiconducting materials: An overview

The Drude model provides the detailed explanation of the electrical conductivity of semiconducting materials. This model describes the scattering of charge carriers at doping atoms, phonons and lattice defects. The average thermal velocity v_{th} of the charge carriers can be defined by the relation in equation (3.1) with the mass m_{e} for electrons or for holes with m_{h}, the Boltzmann constant k_{B} and the temperature T [59]. The charge carriers move through the lattice with the thermal velocity v_{th} until they get diverted by a collision or by scattering with other charge carriers, lattice defects or doping atoms. The distance between such scattering or collision processes is defined as the mean free path l and the time between two deflection processes is defined as the relaxation time $\tau_{\mathrm{e,h}}$. The drift velocity v_{D} is known from the equation of motion for charge carriers (see equation (3.2)):

$$\frac{1}{2}mv_{\mathrm{th}} = \frac{3}{2}k_{\mathrm{B}}\ T \tag{3.1}$$

$$m\frac{dv}{dt} + \frac{m}{\tau}v_{\mathrm{th}} = -eE \tag{3.2}$$

Using the definiton of the charge carrier mobility μ

$$\mu = \frac{e\tau}{m} \tag{3.3}$$

the drift velocity can be written as

$$v_D = -\frac{e\tau E}{m} = -\mu E. \tag{3.4}$$

With the help of Ohm's law $j = \rho E$ and the definition of the electrical current density j follows that the electrical conductivity ρ can be expressed as

$$\rho = \frac{e^2 \tau n}{m} \tag{3.5}$$

and the specific conductivity σ as:

$$\sigma = \frac{1}{\rho} = \frac{1}{en\mu} \tag{3.6}$$

The electrical properties of semiconductors are explained by the energy band model. In this model a band gap separates the valence band and the conduction band. If electrons of the valence band are energetically stimulated, they can be transferred into the conduction band. By this process the material becomes conductive. With rising temperature, the Fermi level of the material changes. As shown in equation (3.7), the Fermi function depends on the temperature T, the chemical potential μ_c and the energy E [59]:

$$f(E,T) = \frac{1}{\exp(\frac{E-\mu_c}{k_B T}) + 1} \tag{3.7}$$

The energy which is needed to promote a charge carrier from the valence band into the conduction band corresponds to the distance between the conduction- and the valence band. This energy is commonly referred as the band gap energy E_g:

$$\sigma(T) \propto \exp(\frac{E_g}{2k_B T}). \tag{3.8}$$

The conductivity is proportional to the charge carrier concentration and the temperature-dependent conductivity is exponential to the band gap energy of the material. The conductivity can be changed by doping a material. If the material is p-doped (positively doped), more holes are produced in the semiconductor (figure 3.1(b)). If the material is n-doped (negatively doped), more electrons are available in the system (figure 3.1(a)). The dotted line in figure 3.1a represents the existence of additional electrons which may be easily excited to the conduction band. In a semiconductor, three different regimes can be observed for different temperatures

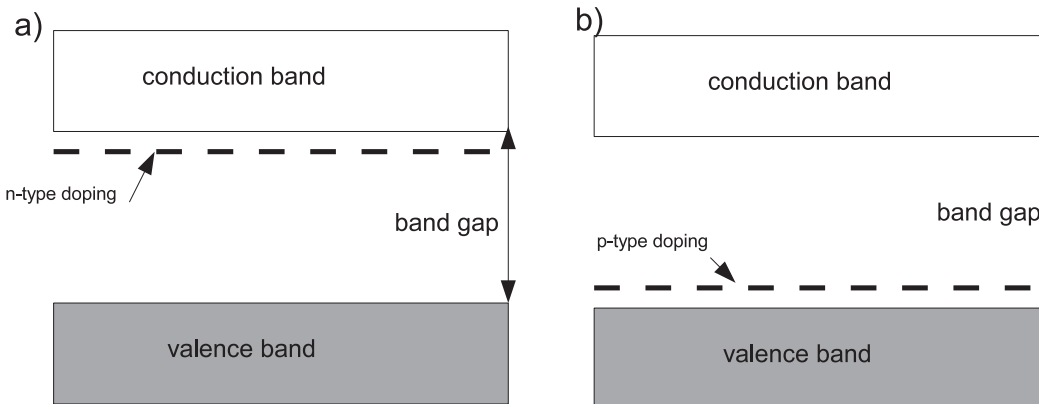

Figure 3.1: Simple band structure of ZnO

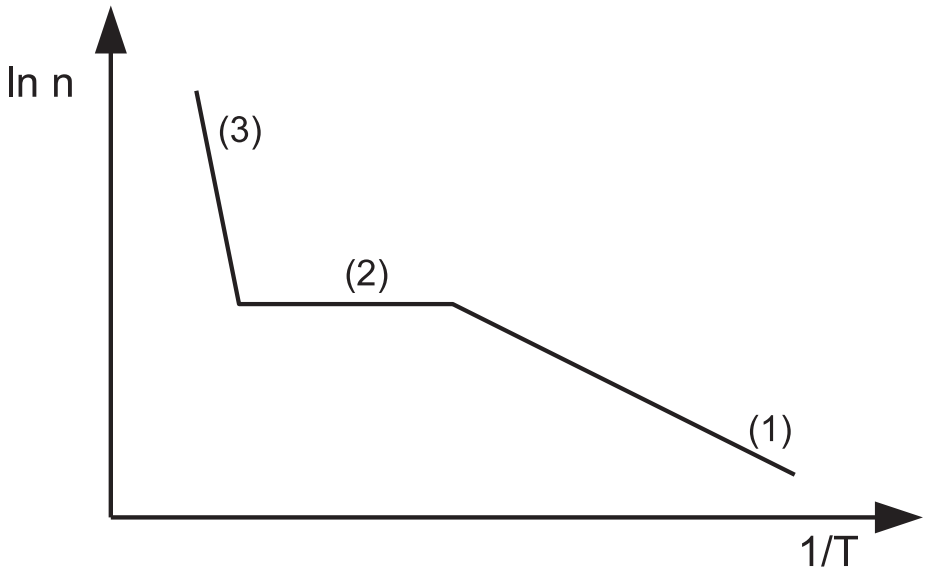

Figure 3.2: Schematic view of the given three areas of the temperature dependent conductivity for a semiconductor.

(see figure 3.2). In the low temperature regime (1) more and more impurities, donors and acceptors, ionize when the temperature rises. In the saturation range

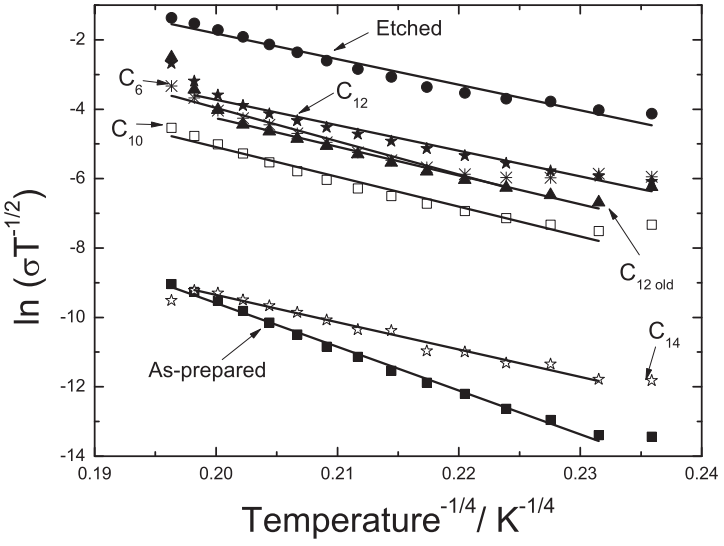

Figure 3.3: Plot of $\ln(\sigma \sqrt{T})$ as a function of $T^{-1/4}$ and the calculated slopes for each sample.

(2) all donors are ionized. The amount of charge carriers is constant but the energy is still not high enough to promote electrons into the conduction band. In the intrinsic range (3) the electrons have enough energy to reach the conduction band, and the conductivity rises with increasing temperature [60]. This theory explains the temperature-dependent conductivity measurements done in this work. There is also the possibility of a variable range hopping transport process between particles. This transport process is used in this work to explain of the transport properties for silicon nanoparticles. The theory of Mott explains the low-temperature behavior of the resistivity in disordered sytems with localized states. The possibility of hopping of electrons between two energetic states is possible when the hopping energy E_{Hop} is high enough in the system. The distance of the hopping between two energetic states is the so called hopping distance R_{Hop}. The hopping energy ranges normally between 0.1 and 0.2 eV. The fitting of the results with the theory of Mott is most promising for silicon nanoparticles. At low temperature, the electrons take longer time for the hopping process and also travel longer distances to find energetic lower levels. In figure 3.3 the plot of $\ln(\sigma \sqrt{T})$ as a function of

$T^{-1/4}$ can be seen. With the help of this plot and the theory of Mott's variable range hopping (VRH), it is possible to calculate the density of the local states N_{EF} and hence the hopping distance and the hopping energy [61–66]. The slope m of the plot in figure 3.3 in combination with a dimensionless constant λ_{vrh}, the spatial extension α of the wave function exp(-αR) and the Boltzmann constant k_B leads to equation 3.9 to calculate the density of the local states:

$$N_{\mathrm{EF}} = \frac{\lambda_{\mathrm{vrh}}\alpha}{k_{\mathrm{B}}m^4}. \tag{3.9}$$

The hopping distance R_{Hop} and the hopping energy E_{Hop} are finally calculated from equations (3.10) and (3.11):

$$R_{\mathrm{Hop}} = \left(\frac{9}{8\pi\alpha k_{\mathrm{B}}TN_{\mathrm{EF}}}\right)^{1/4}, \tag{3.10}$$

$$E_{\mathrm{Hop}} = \frac{3}{4\pi(R_{\mathrm{Hop}})^3 N_{\mathrm{EF}}}. \tag{3.11}$$

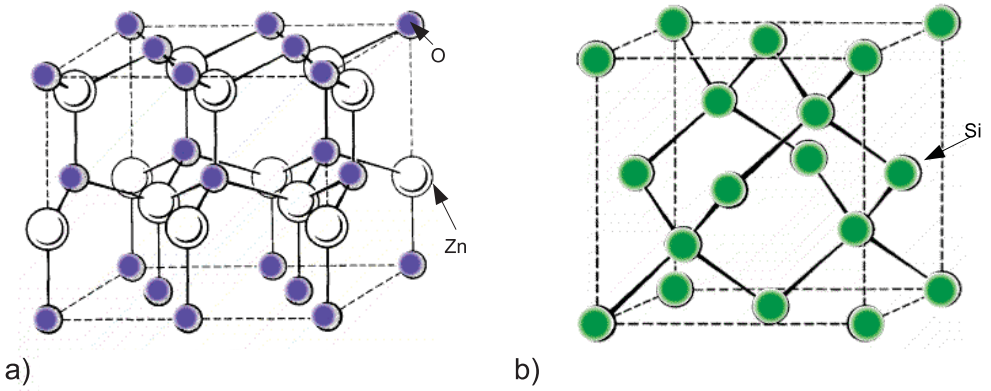

Figure 3.4: a) Wurtzite crystal structure [67]. b) Diamond crystal structure [67].

3.2 Defects and the use of the Kroeger-Vink notation

The crystal lattice of a solid material consists of a spatial arrangement of atoms characterized by long-range order or symmetry. A lattice can be built of several kinds of atoms. The silicon nanoparticles investigated in this work consist of silicon atoms in their inner core and SiO_2 in their outer shell. The ZnO nanoparticles investigated in this work are made of zinc and oxygen atoms, and by doping a third element can be built inside the lattice (i.e. aluminum). A material can be amorphous or crystalline. An amorphous material consists of irregular arranged atoms where only a short-range order can be observed. The nanoparticles used in this work all have crystalline structure. A material is of crystalline structure if the arrangenment of the atoms has a long-range order. There are different kind of arrangements of the atoms. From x-ray diffraction (XRD) measurements, it is known that the ZnO nanoparticles used here have a wurtzite structure (see figure 3.4b) and the silicon nanoparticles have a diamond structure (see figure 3.4a).

The lattices are never perfect and includes some defects. These defects are differentiated in zero-, one-, two- and three dimensional defects. To understand this work, the important defects are Schottky defects, antisites and interstitials, and they all are zero dimensional defects. Schottky defects (see figure 3.5b) are free

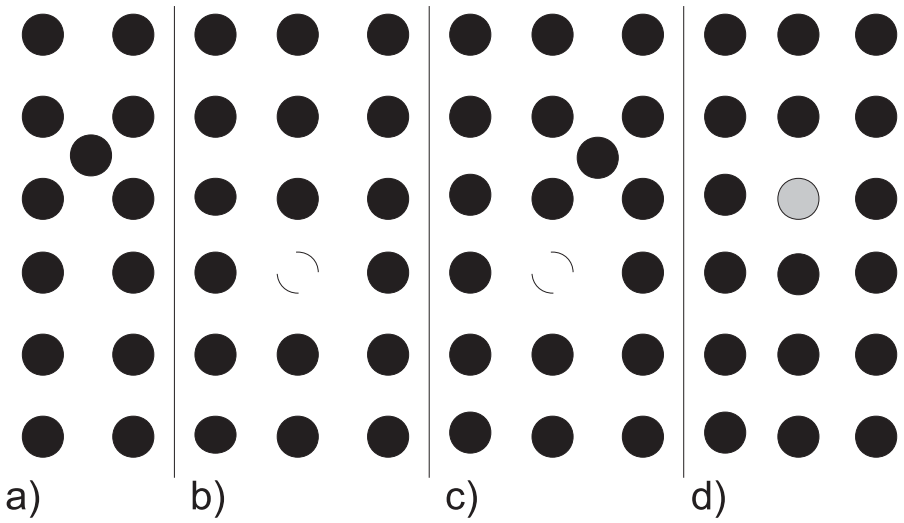

Figure 3.5: Zero-dimensional defects a) Interstital atom b) Schottky defect c) Frenkel defect d) Antisite.

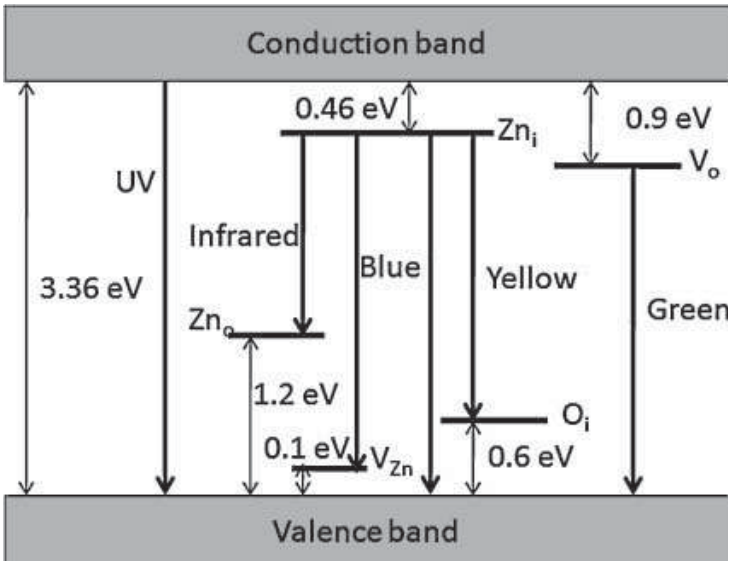

Figure 3.6: Schematic band diagram of ZnO with intrinsic point defect levels [68]

Table 3.1: Kroeger-Vink Notation

Notation	kind of defect
Zn_{Zn}^{x}	zinc atom on zinc place
Zn_{O}	zinc atom on oxygen place
O_{O}^{x}	oxygen atom on oxygen place
O_{Zn}	oxygen atom on zinc place
e^{-}	electron
$V_{O}^{\cdot\cdot}$	vacancy on oxygen place
$V_{Zn}^{\prime\prime}$	vacancy on zinc place
$Al_{Zn}^{\cdot}$	aluminum atom on zinc place,positively charged
$Al_{Zn}^{\cdot\cdot\cdot}$	aluminum atom on zinc place, triple positively charged
$Zn_{Zn}^{\prime}$	zinc atom on zinc place, negatively charged
Zn_{i}	no site (interstitial defect)
O_{i}	no site (interstitial defect)

lattice places where normally should be an atom, and they are always present in equilibrium number in solids. Frenkel defects (figure 3.5c) are couples of interstitial atoms and vacant atom sites. The number of these defects increases with the increase in temperature. Antisites (figure 3.5d) are atoms which are on places in the lattice where another kind of atoms should be and atoms on interstitial places are sitting on places where no atom should be (see figure 3.5a). Electronic defects (electrons and holes) are associated with point defect where they charge them.

The Kroeger-Vink Notation helps to describe all these defects [69]. In table 3.1 an overview of the Kroeger-Vink Notation is given for the ZnO [68]. In figure 3.6 the schematic band diagram of ZnO is shown. The energy levels of some typical defect states can be seen in this figure. Some important properties of the material, especially the optical properties, change as a function of the kind of defects of the lattice.

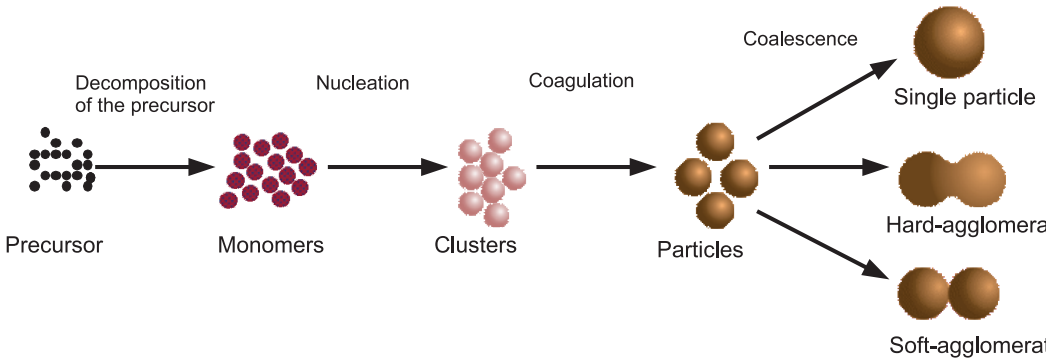

Figure 3.7: Growth of nanoparticles in the gas phase.

3.3 Synthesis

The particles investigated in this work have been synthesized in the gas-phase in a microwave-plasma reactor (Si) or in a hot wall-reactor (ZnO) using the chemical vapor synthesis [70, 71]. At first, the particle formation itself will be explained in this chapter, followed by a short introduction to the synthesis of nanoparticles with a microwave- and hot wall reactor.

3.3.1 Growth of nanoparticles in the gas phase

The particle synthesis takes place mainly in the four steps represented in figure 3.7. The decomposition of a precursor, nucleation, coagulation, and coalescence of nanoparticles. The precursors are in the gas phase when they enter the reaction zone and undergo thermal decomposition. For example, silane (SiH_4) decomposes following the net reaction in equation (3.12).

$$SiH_4 - > Si + 2H_2 \tag{3.12}$$

The following step is the creation of nuclei. Homogeneous nucleation occurs when the degree of the supersaturation is sufficient. After the nucleation the coagulation process starts if the nuclei size is bigger than the critical cluster site r_c [72]. The

critical cluster size r_c is given by equation (3.13), where V_m is the molar volume, σ the surface energy, R_{const} the universal gas constant, p the equilibrium vapour pressure of a particle at temperature T and p_S the equilibrium vapor pressure of the clusters:

$$r_c = \frac{2\sigma V_m}{R_{const} T ln(\frac{p}{p_s})}. \tag{3.13}$$

The characteristic time describing the coagulation process is τ_c, defined as the time required to reduce the nanoparticle number densitiy to the half of its initial value [73]. This time is given by equation (3.14), where β_c is the collision frequency function and N is the number density of particles.

$$\tau_c = \frac{1}{\beta_c N} \tag{3.14}$$

The last growth step of the nanoparticles inside the reactor is the coalescence step. The coalescence process strongly depends on the primary particle diameter d_{NP} and the material properties. The dependence of the coalescence time τ_S and coagulation time τ_c determines if soft agglomerates ($\tau_c \sim \tau_S$), hard agglomerates ($\tau_c < \tau_S$) or non-agglomerated ($\tau_c >> \tau_S$) nanoparticles are formed [74].

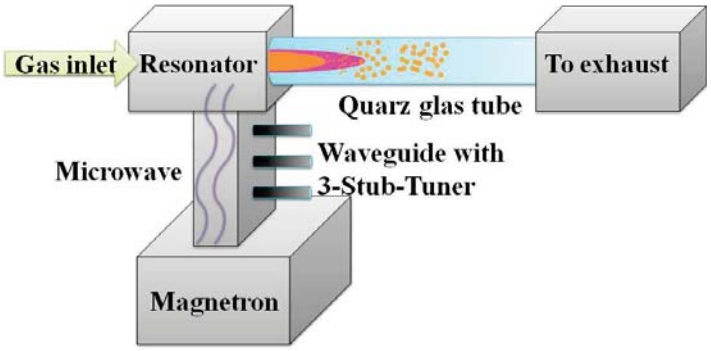

Figure 3.8: Lab scale microwave plasma reactor used for the synthesis of silicon nanoparticles [70].

3.3.2 Microwave plasma synthesis

The silicon nanoparticles investigated in this work have been synthesized in a microwave plasma reactor in the gas-phase. A schematic view of the used set-up is shown in figure 3.8. The reactor is a commercially available Cyrannus plasma source (iplas) and is connected with a 6 kW microwave generator. It has a quartz tube and a gas delivery system which injects the gas coaxially into the plasma where the decomposition of the precursor takes place. For the synthesis of silicon nanoparticles with a size used in this work of about 50 nm the reactor pressure is set to 200 mbar and a microwave frequency of 2.4 GHz is used. The used precursor is silane (SiH_4) with a flow of 150 sccm mixed with an argon flow of approximately 5 slm and a hydrogen flow of 3 slm. For the silicon nanoparticles doped with phosphorous, phosphine (PH_3) is added to the precursor gas mixture. With this synthesis route up to 10 $\frac{g}{h}$ of silicon nanoparticles can be produced.

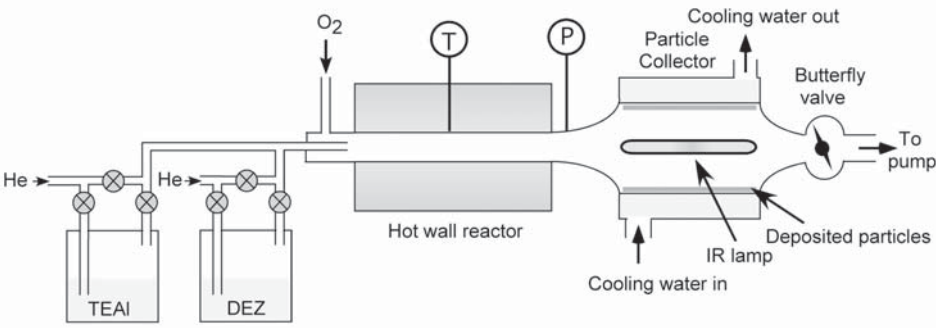

Figure 3.9: Set-up for particle synthesis in a hot-wall reactor with a subsequent thermophoretic particle collector [71].

3.3.3 Hot-wall reactor synthesis

All ZnO nanoparticles investigated in this work are synthesized in a hotwall reactor. In figure 3.9 the setup is shown. It consists of a wall-heated flow reactor, a precursor supply system and a thermophoretic particle collector. The precursor supply system consists of two bubblers. For undoped ZnO nanoparticles only one bubbler filled with diethylzinc (DEZn) is used. For doping the ZnO nanoparticles with aluminum, a second bubbler filled with triethylaluminum (TEAl) is used. The bubblers are placed in a temperature controlled oil bath to adjust the precursor vapor pressure. Helium is transported troughout the bubblers and the output flow is controlled by a mass flow controller. In order to prevent any oxidation of the precursor before they enter the oven, the pure oxygen is mixed to the precursor helium blend only immediately before the oven inlet. The synthesis pressure for all experiments is about 20 mbar. The aluminum tube inside the oven, where the particles are synthesized, has a diameter of 19 mm. The synthesis takes place always at 800 °C to guarantee full decomposition and also a safe handling of the precursors, because the decomposition of the DEZn takes place already at 400 °C [71]. The mean residence time of the precursor in the oven is 20 ms, and during this time the ZnO particles are synthesized in three main steps: nucleation, co-

agulation and coalescence (see chapter 3.3.1). The synthesized nanoparticles are collected in a thermophoretic particle collector. The temperature gradient inside the collector ranges from 800 °C (produced by an infrared lamp) down to room temperature (water cooling). The production rate is about 0.5-2 $\frac{g}{h}$.

3.4 Characterization and functionalization process

Different methods are used in this work to characterize the synthesized nanoparticles. In this chapter the most important and widespread methods are described with a view on the handling of the nanoparticles used in this work.

3.4.1 X-ray diffraction (XRD)

X-ray diffraction (XRD) is the standard method to get information about the crystallite site, chemical composition and lattice constants of a solid material. A PANalytical X-ray diffractometer (X´Pert PRO) is used to measure the diffraction pattern of the investigated materials. The atoms in a material are arranged in a 3-dimensional lattice which can be described as a series of overlapped layers. The inter-layer distance d is a characteristic property of every material (see figure 3.10 for detail). If the monochromatic beam with a wavelength of λ=1.54 Å arrives at an incident angle θ_i=2 θ, a constructive interference leads to the typical Bragg reflections according to Bragg's law:

$$n\lambda = 2d\sin\theta. \tag{3.15}$$

Ni-filtered Cu-kα radiation is used with a Cu-tube operated at 40 kV and 40 mA. The diffracted x-ray beam is detected with an X´Celerator detector. The scan resolution is 0.005° and the incident angle range is 2θ = 20°-120°. Data fitting is provided by MAUD [75]. This program uses a Rietveld refinement to get information about the structural properties of the material. The diffraction pattern are fitted starting from the parameters of bulk ZnO [76] (wurtzite lattice, $P6_3mc$ space group). The measurements for the silicon nanoparticles are fitted with the bulk parameters of Si (diamond structure, Fd_3m space group). The background signal of the measurements is fitted with a sixth-order polynomial fit.

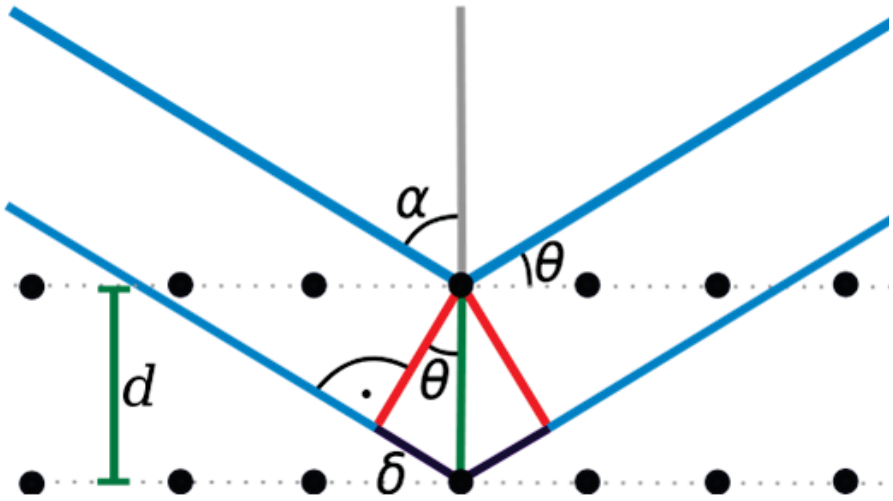

Figure 3.10: Bragg reflection in a crystal lattice.

3.4.2 Impedance spectroscopy

The impedance spectroscopy receives the response of the material on an applied frequency. The result of this measurement allows explaining different contributions to the resistivity of a material and the transport mechanism. The impedance is the complex alternating current resistivity which depends on the applied frequency on an alternating (AC) current. The excitation output U_t depends on the amplitude U_0 of the input signal, the angular frequency $\omega = 2\pi f$, and the time t and is given in equation (3.16). The resulting current I_t can be phase-shifted and has an amplitude of I_0, as described in equation (3.17).

$$U_t = U_0 \sin\omega t \tag{3.16}$$

$$I_t = I_0 \sin\omega t + \phi. \tag{3.17}$$

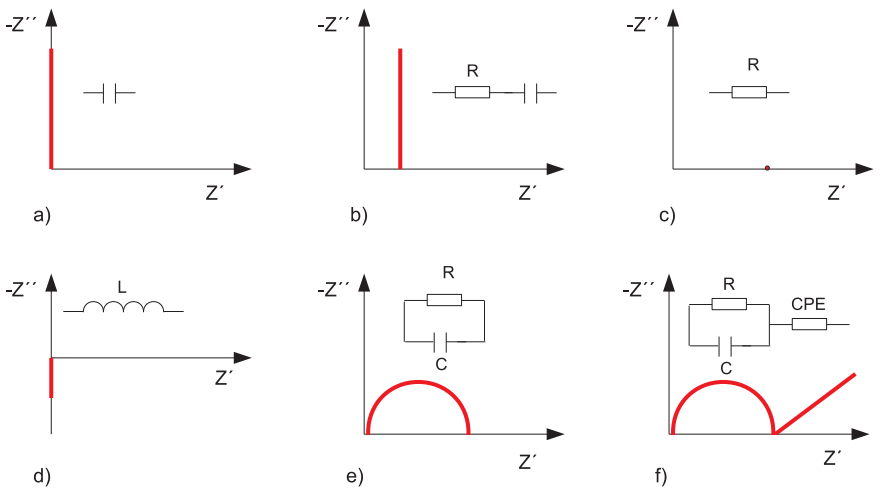

Figure 3.11: Nyquist plots for the different electronic elements a) Capacitance b) Resistance and capacitance in serial c) Resistance d) Inductance e) Resistance and capacitance in parallel f) Resistance-capacitance in parallel connected with a Warburg impedance in serial.

The impedance Z is derived from Euler relation (see equation (3.18)) and Ohm's law. $U = RI$, where U ist the voltage, I is the current and R the resistance. The relation for the impedance can be seen in equation (3.19).

$$\exp(i\phi) = \cos(\phi) + i\sin(\phi) \tag{3.18}$$

$$Z(\omega) = \frac{U_t}{I_t} = \frac{U_0 \exp(i\omega t)}{I_0 \exp(i\omega t - i\phi)} = Z_0(\cos\phi + i\sin\phi) = Z_0 \exp(i\phi). \tag{3.19}$$

Figure 3.13 shows an image of the impedance Z plotted in the complex plane. The angle between the x-axis and the vector $\vec{Z}$ represents the phase ϕ. One of the common methods for measuring the impedance is the frequency domain method. In the frequency domain method, which is applied in this work, the frequency-dependent impedance is observed by varying the frequency of the alternating current step by step. The shift between the current and the voltage gives the phase ϕ. The

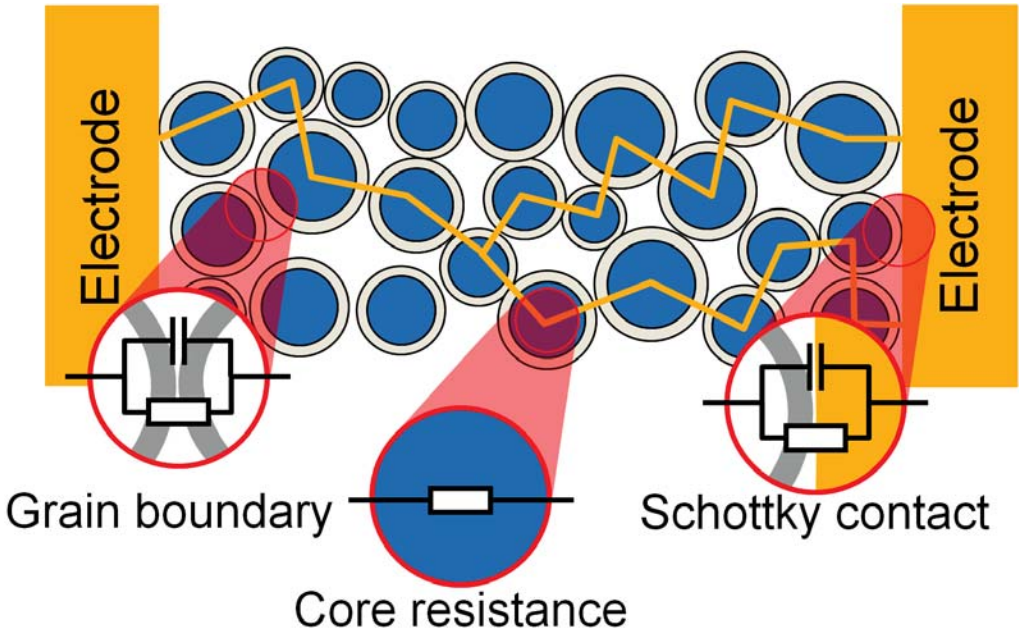

Figure 3.12: Schematic view of the electrical transport processes within the particle network. The grey area surrounding the blue particles indicates the depletion layer. An equivalent circuit is used for each contribution. The orange area around the blue particles presents the depletion area around the particle.

impedance is then calculated from the following equations (3.20):

$$Z = Z^{'} + iZ^{''} = |Z| \exp(i\phi), \tag{3.20}$$

$$|Z| = \sqrt{(Z')^2 + (Z'')^2}, \tag{3.21}$$

$$\phi = \arctan\left(\frac{Z''}{Z'}\right). \tag{3.22}$$

By using the program Visfit [77] it is possible to model circuit diagrams equivalent to the measured data, and to explain the different contributions to the impedance that occur by changing resistivity, inductivity or capacitiy. The resonant frequency of each RC-element can be calculated under the condition:

$$\omega RC = 1. \tag{3.23}$$

In figure 3.11 the Nyquist plots for different equivalent circuits are shown. In Figure 3.11a the plot for a capacitance is shown. There is no real part of the impedance. The plot for a pure resistance (see figure 3.11c) only has a real part and the serial connection of a resistance and a capacitance produces a graph combined which is shifted of the distance of the real part of the resistance(figure 3.11b). The parallel connection of a resistance and a capacitance produces a semicircle. Due to the frequency dispersion of the capacity which produces the semicircle shown in figure 3.11e. By adding the so called Warburg impedance in series to the parallel connection of a resistance and a capacitance, a semicircle with a tail in the lower frequency region and with an angle of 45° is observed (figure 3.11f). This behaviour is observed when α of the Warburg impedance is about 0.5 (see details later). In figure 3.12 the schematic view of the particle network between two electrodes is reported. The different resistivity contributions are described by equivalent circuit elements. In order to model the particle-particle contacts (the so called grain boundary) and the particle-electrode contact (Schottky contact) an RC element is used. The resistance of the core itself is described by a single resistor. The impedance function of a resistance R, capacitance C and inductance L is described with the following equations:

$Z = R$ (resistance R)

$Z = \frac{1}{i\omega C}$ (capacitance C)

$Z = i\omega L$ (inductance L).

In some system the phase deviates from ±90°. In this case a mathematical model, the CPE-element, is used. The CPE is defined by equation (3.24):

$$Z = \frac{A}{(i\omega)^{\alpha}}. \tag{3.24}$$

α:

$\alpha = 0$ (resistance R)

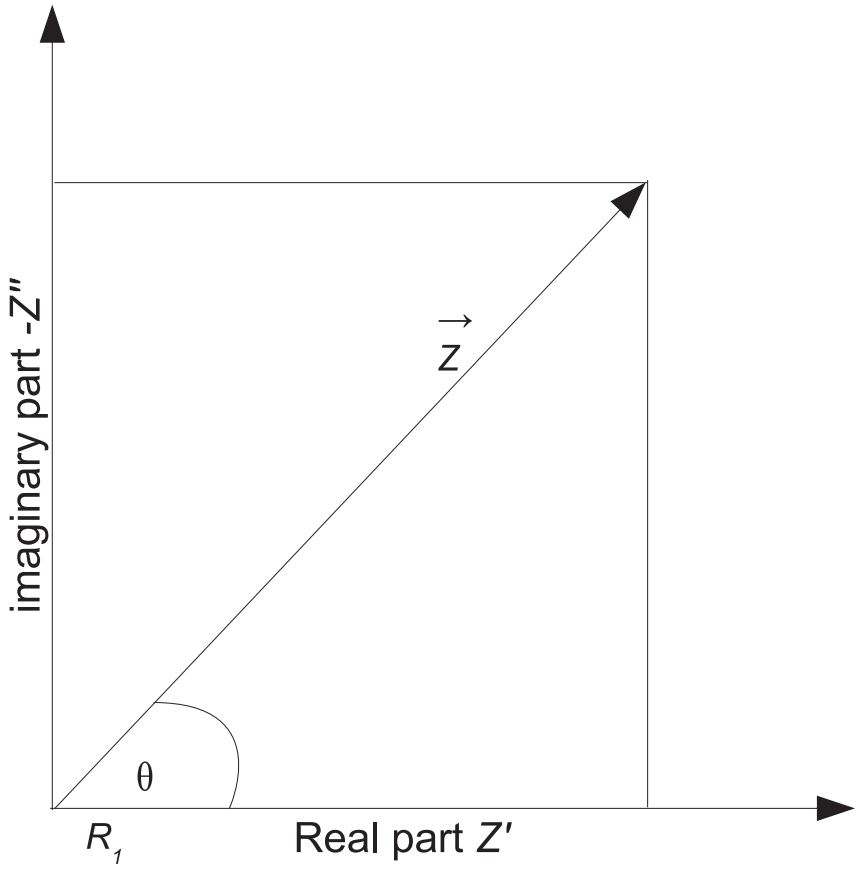

Figure 3.13: Graphical presentation of an impedance in the complex plane.

$\alpha = 1$ (capacitance C)

$\alpha = -1$ (inductance L)

$\alpha = 0.5$ (Warburg impedance, typically seen for materials with diffusion limited ionic conductivity).

In figure 3.12 the schematic view of the electrical transport processes within a porous particle network can be seen. The overall conductivity of the material depends on the surface reactivity (i.e. environmental condition) and on the charge carrier transport processes particle-particle and particle-electrode. It is always pos-

sible to have all three kinds of transport processes in one system. The resistivity of the grain boundaries contributes to the overall conductivity when the particles are small and not sintered togeher. Another contribution comes from partly depleted necks between two particles. The mean free path of the free charge carriers in this case is comparable with the size of the grains. Therefore, the number of collisions by free charge carriers in the bulk area of the particles is comparable with the number of surface collisions. Such equilibrium can be influenced by adsorbed atoms, and additional scattering can take place.

3.4.2.1 Sample preparation for the impedance measurements for compacted powders

All powders are compacted for the measurements except for the measurements of films. The initital amount of particles depends on the material. For the zinc oxide pellets about 9-10 mg of ZnO nanoparticles are used, and for the silicon pellets about 2-5 mg are used. The powder is placed in a sample holder located between two pressing plates having 5 mm diameter and polished surfaces shown in figure 3.14. The sample holder is placed in a hydraulic press and a compression force of 18 kN is applied for 30 min. This force is equivalent to a pressure of 1.02 GPa on the 5 mm pellets. SEM images of the resulting pellet can be seen in figure 3.14 (here for example a ZnO pellet) with a typical green density of 60% compared to bulk ZnO.

3.4.2.2 Measurement metrology of compacted powder

The produced pellet is sandwiched between two spring-loaded platinum disks in the measurement cell. The measurement cell is situated in a gas tight ceramic tube with gas in- and outlet. A tube furnace heats the ceramic tube and the measurement cell. For preventing short circuits between the platinum disks, their diameter matches exactly with the diameter of the ZnO pellets. In figure 3.15 a schematic view of the used measurement cell is presented. Changing the material of the metal contact did not show any influence on the results and platinum contacts were then used as the standard material. For the electrical characterization a

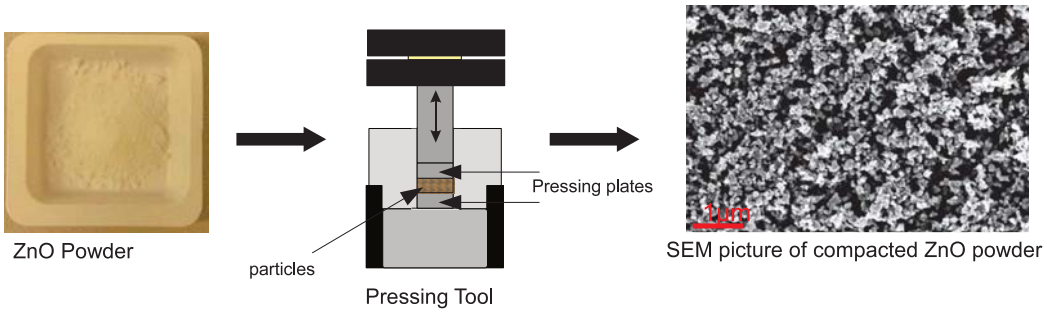

Figure 3.14: On the left hand site ZnO nanoparticles before preparation. In the middle the pressing tool for the compaction and on the right site the resulting pellet after the compaction.

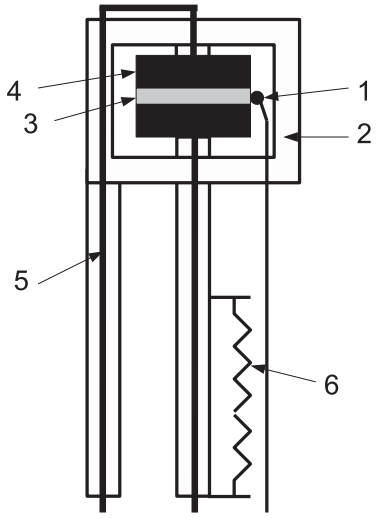

Figure 3.15: Schematic view of the used measurements cell. 1: thermocouple, 2: ceramic holder, 3: sample, 4: platinum disks and platinum electrodes, 5: platinum wires, 6: spring.

Hewlett-Packard (HP4192A) impedance spectrometer was used. All samples have been measured in the frequency range 10 Hz-10 MHz in logarithmic steps with 20 frequency points each decade. The first measurement took place at lowest temperature (around room temperature or 50 °C) and then every 25 °C the impedance

was measured until the final temperature (mostly 400 °C) was reached. The temperature was stabilized for five minutes before the acquisition of every point to allow a maximal temperature deviation of ±0.5 °C.

3.4.3 Scanning Electron Microscopy (SEM) and Electron Beam Lithography (EBL)

One part of this work deals with the possibility of creating an ink-jet printed ZnO film which may be attractive as hydrogen sensor. The used sensors are manufactured by electron beam lithography (EBL). All the process steps are performed in a clean room atmosphere to prevent any sample contamination of the samples. Silicon substrates of 5 mm lenght and width and 0.4 mm thick was used. Before measurement, the substrates were cleaned with analytical isopropanol. At the top of the cleaned substrate an electron sensitive double resist is spin-coated (see figure 3.16a and 3.16b). During the first step a resist called 200K4% is spin coated at the top of the substrate at 8000 rpm. Then the resist is tempered at 100 °C for 10 min. After that, the second resist (950K1%) is spin coated at 8000 rpm and tempered at 100 °C for 5 min. The substrate is placed in the scanning electron microscope (SEM) with an attached EBL unit. In this work a SEM (LEO 1530 (Zeiss)) with an electron beam unit with a maximum accleration voltage of 20 kV is used (Elphy Plus). The prepared substrate is exposed to an electron beam of 20 kV and a dose of 180 $\mu C/cm^2$ is needed (see figure 3.16c). During the exposure, the electrons in forward and backward scattering break the long polymer chains of the resists at the area defined by the writing electron beam. The outcome of the writing process depends on the area written and on the used resist; the necessary resolution of the resulting structure is adjustable with the used dose and takes about 16 h. After the writing process the substrate is removed from the SEM and treated in a developer (Allresist AR600-56). This developer consists of a mixture of 25% methylisobutylketon and 75% isopropanol. After 30 s, the developing process is stopped by putting the substrate into a stopper (AR600-60) for 10 s (see figure 3.16d). Further details of the resulting resist profiles can be found elsewhere [78, 79]. After the developing and stopping process of the resist, the sample is moved to a high vacuum coater. Here, a gold film of about 50 nm is evaporated

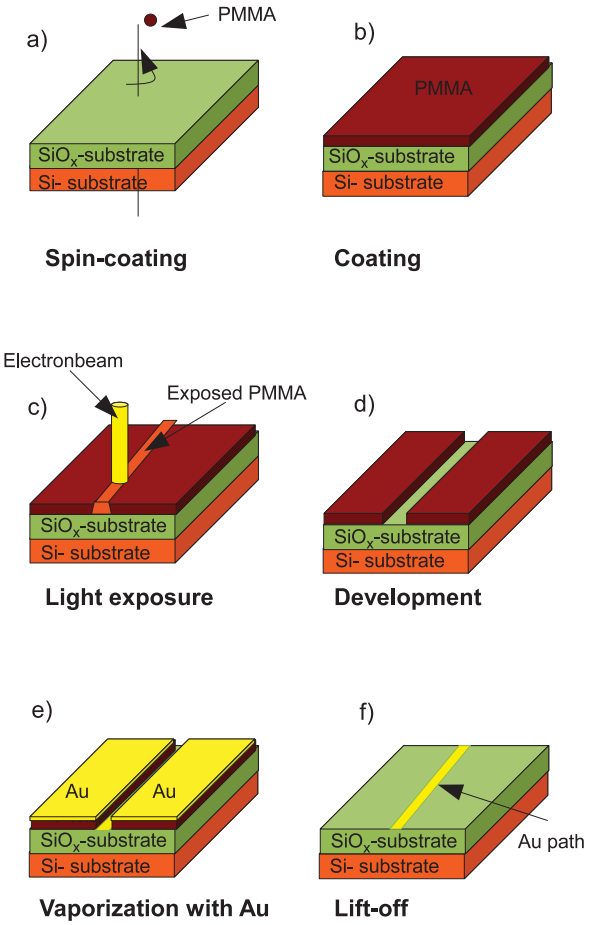

Figure 3.16: a) Spin coating of PMMA. b) Spin coated PMMA on the surface of the SiO_x substrate. c) The PMMA is exposed to the electron beam on a defined structure. d) After developing step of the electron beam exposed part of the PMMA. e) Evaporation of Au on the surface of the structure. f) After the lift off process the Au-structure is left.

on the top of the substrate as shown in figure 3.16e. Then the substrate with the evaporated gold is placed in a box with hot acetone (75°C) to remove the resist

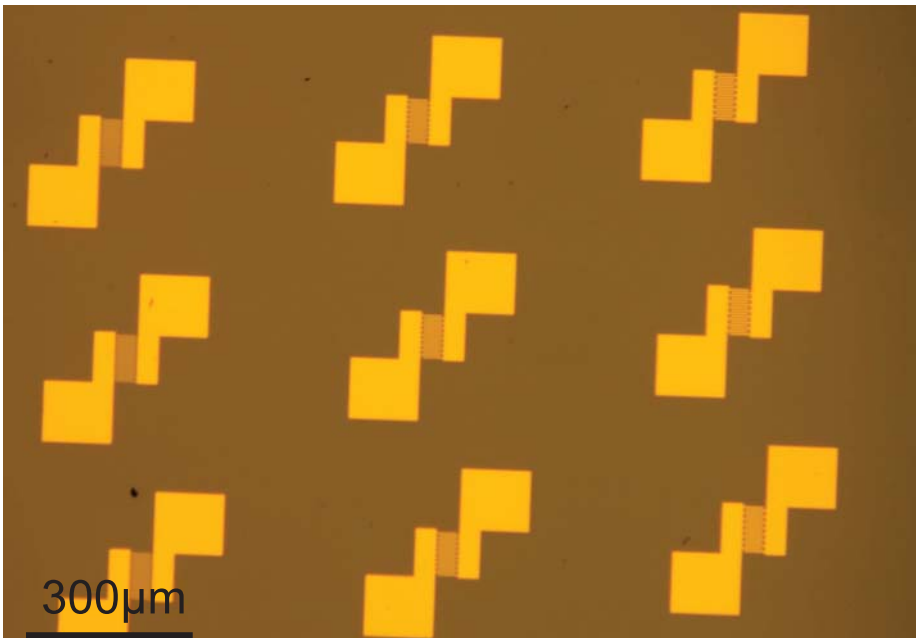

Figure 3.17: Picture taken with an optical camera. Nine interdigital structures can be seen exemplarily for the interdigital structures used for the thin film measurements produced via ink-jet printing.

(lift-off process). The gold film on the top of the resist is removed with this process and only the structure from the layout of the electron beam process stays on the subtrate (see figure 3.16f; here only one gold path is shown to make the drawing simple). A picture of the resulting interdigital structure can be seen in picture 3.17.

3.4.4 Functionalization process for silicon nanoparticles

Silicon nanoparticles have a wide variety of unique properties which have been successfully used to improve performances of solar cells, lasers and diodes [24, 26, 27, 40, 41]. Furthermore, Si is the second most common element in earth's crust [39], making it an ideal candidate for industrial applications: it is inexpensive,

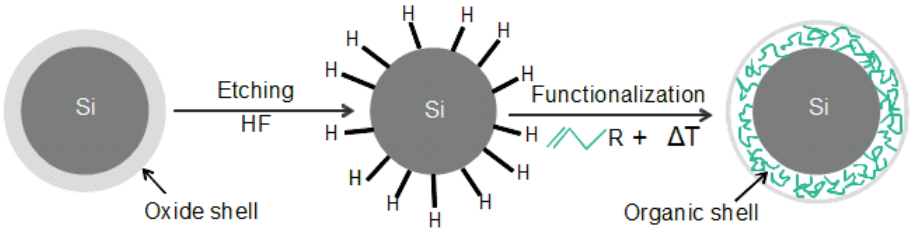

Figure 3.18: The functionalization process.

non-toxic and relatively easy to produce and define. Silicon nanoparticles have a high specific surface and their oxide shell is characterized by a high defect concentration [42, 43]. For certain applications, the only drawback is the oxide shell around the silicon core. This oxide shell decreases the electrical conductivity and also the optical properties of silion nanoparticles [44–46, 58]. In this work an investigation on the electrical properties of Si nanoparticles is presented. By removing the oxide shell via hydrosilylation, a step towards the production of stable surface oxidation of silicon nanoparticles is made [47–49]. The main drawback of hydrosilylation is the subsequent reoxidizing of the surface, therefore a method to prevent the reoxidation has to be found [51]. The surface functionalization with organic molecules is one of the most common answers to this problem, and it has been performed by several groups before [52–56]. The outcoming silicon-carbon bonds (Si-C) are strong and have a low electron polarisation due to the little difference of elektronegativity between C and Si [48, 57]. The optical properties of these functionalized silicon nanoparticles were already deeply investigated, but to the best of our knowledge their electrical properties are unknown.

The Si nanoparticles used in this work are functionalized as follows. The oxide layer covering the silicon nanoparticles is removed by etching in hydrofluoric acid. The etching process takes part under controlled N_2 atmosphere to avoid steady surface re-oxidation. A suspension of 40 mg of silicon nanoparticles in 4 mL of methanol is added to 10 mL of hydrofluoric acid (HF 50 wt%). The dispersion is stirred for 5 min at room temperature and then filtered on a polyvinylidenfluorid (PVDF) membrane filter with pore size of 100 nm. The functionalization is done on

the freshly etched silicon nanoparticles by a thermally induced hydrosilylation process by using the n-alkenes hexene (C_6), decene (C_{10}), dodecene (C_{12}), tetradecene (C_{14}) and octadecene (C_{18}). The etched particles are dispersed in the respective alkenes and are treated with an ultrasonic disperser. Then the dispersion is heated up to 120 °C (except C_6 which is heated up to 60 °C due to a low boiling point of 63 °C) for 12 h. In figure 3.18 the functionalization steps on silicon nanoparticles is schematically shown. The dark grey core represents a Si nanoparticle, while the light grey layer around the core represents the oxide shell. By etching the oxide shell is removed and the silicon core surface is hydrogen terminated. By functionalizing the etched silicon nanoparticle, the surface is covered with organic alkenes in the derived lenght. The resulting dispersion of functionalized silicon nanoparticles is finally centrifugated, washed and stored in vacuum condition for receiving dry, functionalized silicon particles.

4 Results and discussion for ZnO nanoparticles

The structural and electrical properties of the ZnO nanoparticles are characterized with regard to the influence of Al doping, the behavior in changing moisture atmosphere and as ink-jet printed ZnO thin film. The influence of the Al doping concentration is investigated as well as the difference of the electrical transport properties of the ZnO nanoparticles in synthetic air and hydrogen atmosphere. The investigation on the electrical properties in different moisture atmosphere supports the observed growing behavior of ZnO nanoparticles in moisture atmosphere [32]. With the help of ink-jet printing, a ZnO thin film is printed and investigated with a view on the possibility to use ink-jet printed ZnO films as hydrogen sensors.

4.1 Structural properties

The crystal structure of the ZnO nanoparticles is determined by XRD using a PANalytical X-ray diffractometer with Ni-filtered Cu-K_α (1.54 Å) radiation. Figure 4.1 shows the XRD results for ZnO doped with different molar percentages of Al (0%, 5.4%, 7.0%, 7.7%, 16.8%, and 37.6% of Al). The molar percentage of Al represents the mole of Al to moles of Al and Zn atoms. The nanoparticles have a spherical shape and a narrow size distribution observed from the transmission electron microscopy (TEM) measurements. The synthesis parameters (i.e. pressure and temperature) were kept constant for different Al molar percentages. Figure 4.1 gives the information that the crystal structure of doped and undoped ZnO are of wurtzite type. Particulary, we found the wurtzite lattice with a doping concentration of 37.6 %, which is in contrast with the finding of Nunes [80] and Lu [35]. For thin films, the solubility limit of Al in ZnO is 2% only [35]. On the other hand, the solubility limit of Al in ZnO prepared by magnetron sputtering [80] is about 20 to 30%. The CVD process used in this work allows a much more efficient

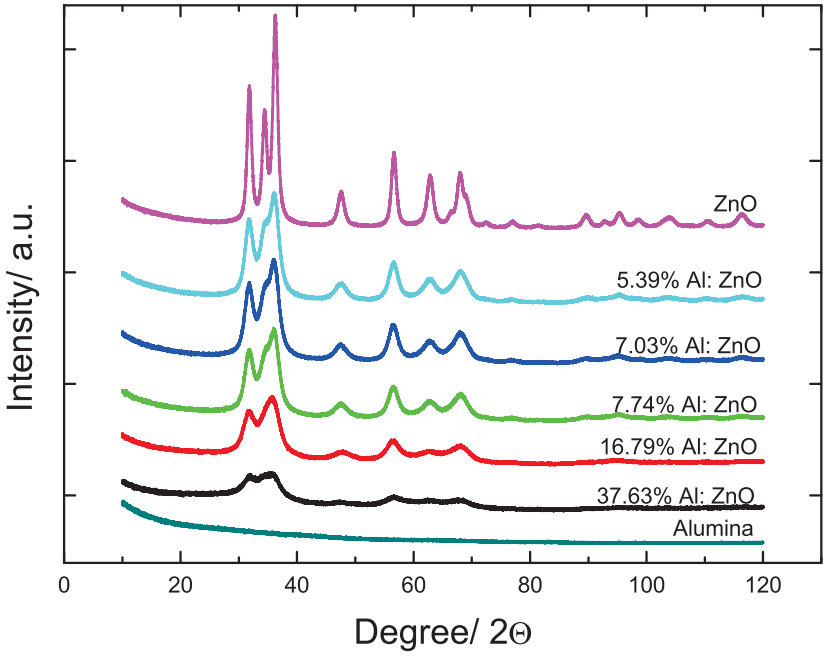

Figure 4.1: X-ray diffraction pattern of doped and undoped ZnO nanoparticle samples synthesized via a hotwall reactor.

incorporation of aluminum atoms compared to both the magnetron sputtering [80] and the wet chemical route [35]. By CVS a limit concentration of at least 37.6% of Al in ZnO is reached. However, this result has to be taken carefully since at high Al concentration a potentially formed Al_2O_3 is expected to be amorphous which is not visible in the XRD pattern. In figure 4.1 the broadening in the XRD signals for higher Al concentrations is clearly visible. The broadening of the XRD signal occurs because of the decreasing of the crystallite size of the ZnO nanoparticles with higher aluminum concentration. The crystallite size is calculated by Rietveld refinement of the XRD data and the results can be seen in figure 4.2, where the crystallite size is plotted as a function of the aluminum concentration. During the synthesis process, the addition of Al-combining impurities might slow down or even stop the coalescence step. Due to this effect and the existent impurity drags the growth rate is delayed even more for the higher alumina concentrations.

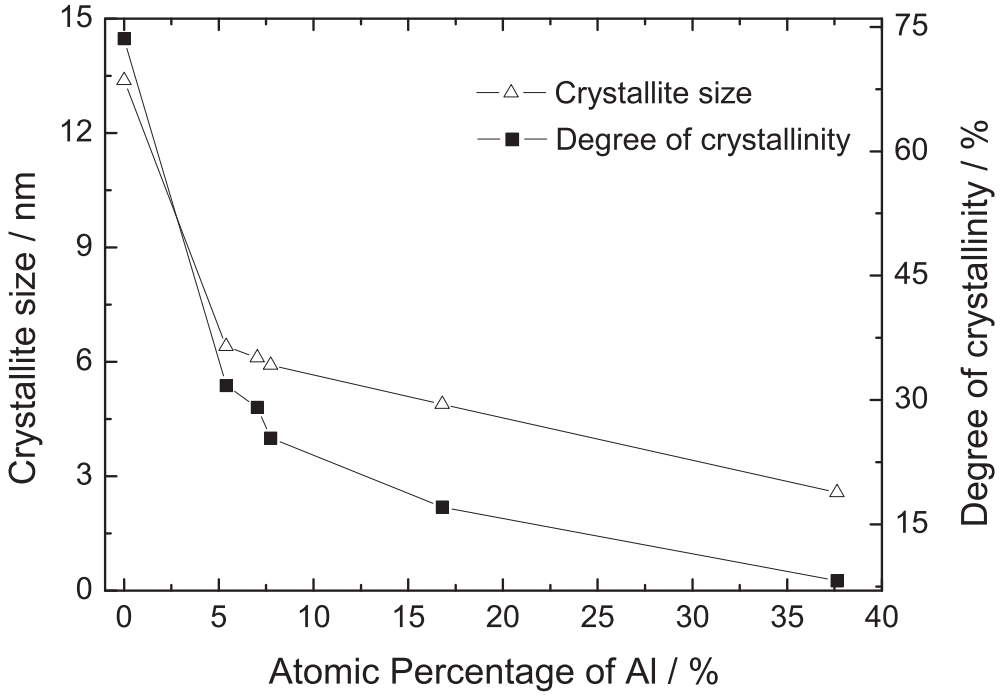

Figure 4.2: Crystallite size and degree of crystallinity as a function of the molar percentage of Al calculated from Rietveld refinement.

In figure 4.1 one can see the decreasing crystallite size with increasing Al content. The degree of crystallinity can be presented by the equation 4.1 where J represents the XRD signal from coherent scattering and B presents the background signal which comes from the incoherent scattering of the sample [81]:

$$\Gamma = \frac{\int J d\theta}{\int (J + B) d\theta}. \tag{4.1}$$

The integration is performed in the range of 20° $\leq 2\theta \leq$120°. Higher values of Γ indicate either the presence of a higher fraction of crystalline phases in the material or a lower density of defects. In figure 4.2 one can see the degree of crystallinity and the crystallite size as a function of the atomic percentage of Al. In this plot a clear dependence of the crystallite size and the degree of crystallinity on the doping

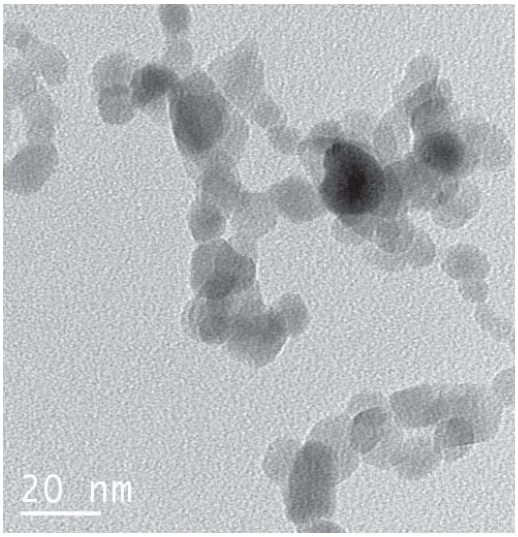

Figure 4.3: TEM image of ZnO nanoparticles with 5.4% of Al and a particle diameter of 7.4 nm.This sample is thermophoretically sampled directly from the reactor.

concentration is observed. The decrease in crystallinity has two reasons. First, the incorporation of Al atoms in the crystal-lattice may form a separate phase of amorphous alumina. Second, the generation of defects during the synthesis step increases with higher aluminum content due to a higher incorporation of dopant atoms. The TEM picture shown in figure 4.3 is an example of ZnO nanoparticles doped with 5.4% Al. It shows that the particles are almost spherical with some degree of agglomeration, and they exhibit a mean primary particle diameter of 7.4 nm. The TEM size measurement is consistent with the size calculated from the XRD signals. In figure 4.4 the lattice parameters a and c are presented as a function of the doping concentration. The small ionic radius of Al compared to Zn can account for the decrease of the lattice parameter c and the increase of the parameter a towards higher aluminum concentrations. The steep decrease of the lattice parameters for a doping concentration higher then 7% may result from Al atoms which are forced to occupy other lattice places, thus reaching the nominal dopant concentration but occupying different sites.

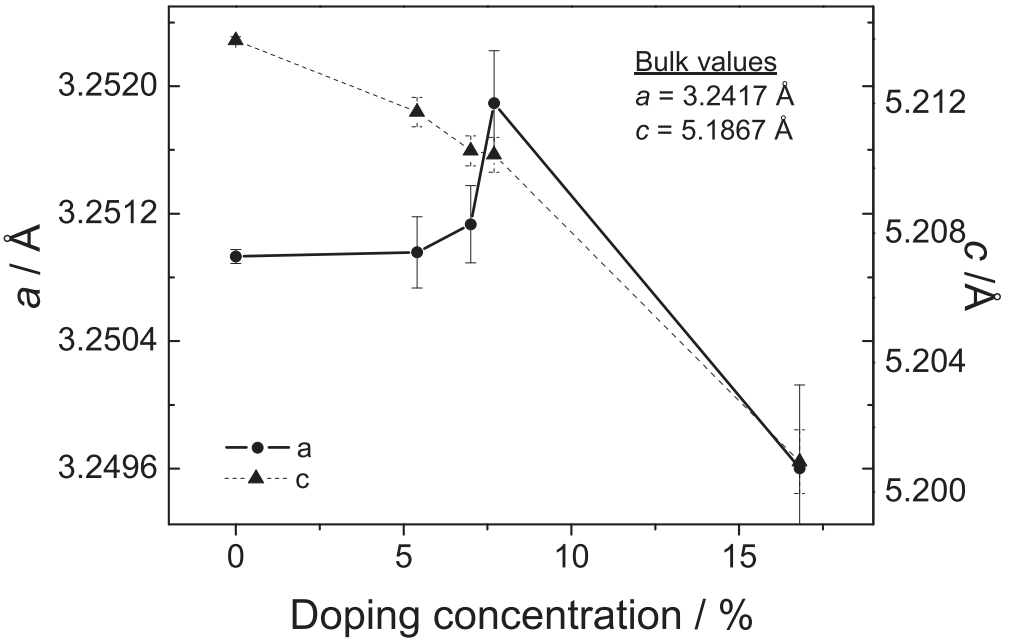

Figure 4.4: Influence of Al percentage on the lattice parameters a and c of the ZnO nanoparticles.

4.2 Electrical properties of ZnO nanoparticles

The results for ZnO nanoparticles are presented in this chapter. First, the influence of the gaseous environment on the electrical properties of ZnO nanoparticles for compacted powder is explained. Second, the electrical properties of aluminum doped ZnO nanoparticles synthesized with a hotwall reactor are presented. The last part in this chapter deals with the influence of moisture on the electrical properties of undoped ZnO nanoparticles.

4.2.1 Zinc oxide nanoparticles in different gaseous environments

The electrical properties of ZnO nanoparticles change in different gaseous environments. Especially the transport properties of ZnO nanoparticles in hydrogen atmosphere changes dramatically for the different doping concentrations. In this chapter the electrical properties of ZnO nanoparticles in synthetic air and in hydrogen atmosphere for different temperatures are presented. For the measurements shown in this chapter, the first three cycles, (one cycle means all measurements between 50 °C and 400 °C) are measured in hydrogen atmosphere and the following three cycles are measured in synthetic air (20.5% O_2 ultra high purity in N_2). After reaching 400 °C after the third cycle in hydrogen atmosphere, the measurement cell is cooled down in hydrogen atmosphere until the sample reaches room temperature. Then, the gaseous environment is changed from hydrogen atmosphere to synthetic air.

In figure 4.5 the Nyquist plot of one of the samples in hydrogen atmosphere is shown. Only data for the real part of the impedance are found without any frequency dispersion. The conductivity of all measured samples in hydrogen atmosphere is very high and shows pure ohmic behavior. In this data set the contributions from contact or transfer resistances from cables are not eliminated. In figure 4.6 the first cycle in hydrogen can be seen beside others. A strong increase in conductivity with increasing temperature can be observed. Cycle two (not shown) and three keeps the very high conductivity which is reached after the first cycle and they also show identical conductivity values. The strong increase in conductivity during the first cycle measured in hydrogen atmosphere is attributed to an

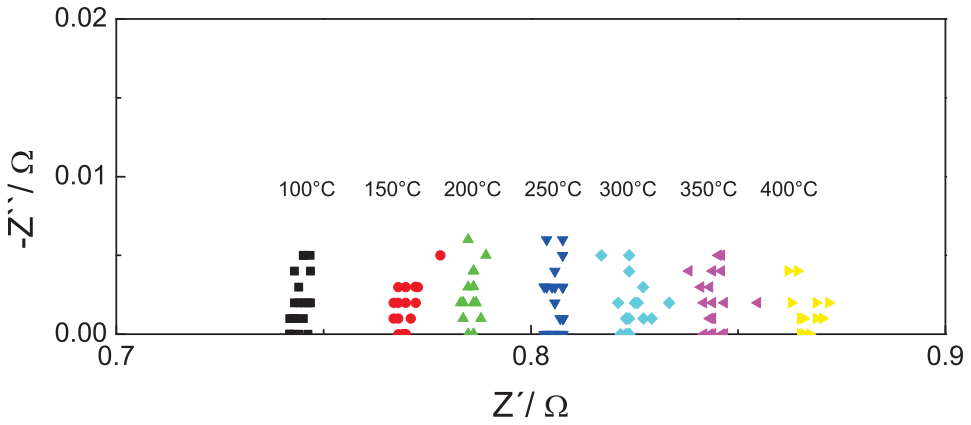

Figure 4.5: Nyquist plot for the measurements in hydrogen atmosphere for a selection of temperatures (e.g.here undopes ZnO nanoparticles). A pure ohmic transport behavior is observed.

annealing effect which is observed for all measured samples, even in synthetic air. For this reason all shown data points and calculations are done from the third cycle at each atmosphere to neglect any annealing effect or the influence on the doping concentration and the gaseous environment. Back to the measurements in hydrogen atmosphere, the observed high conductivity has to be explained. The increase in conductivity in hydrogen atmosphere is already well known from the literature. The work of You et al. shows I-U measurements for ZnO nanoparticles treated with a hydrogen plasma. They observed an increased current after the plasma treatment [82]. Liu et al. also showed the increase of the conductivity of ZnO films after annealing in hydrogen at different temperatures, and they explained it as consequence of hydrogen diffusion and formation of a shallow donor during the hydrogen treatment [40]. The increase in conductivity for the measurements in hydrogen atmosphere results from the generation of free charge carriers following the doping with hydrogen atoms. Our explanation of the underlying physics is repeated below using Kroeger-Vink-Notation [83] (see equation (4.2)). Zinc atoms on Zn sites (Zn_{Zn}), oxygen atoms on oxygen lattice site (O_O) in combination with the provided hydrogen atoms and a bonding of the hydrogen (atoms) to the lattice

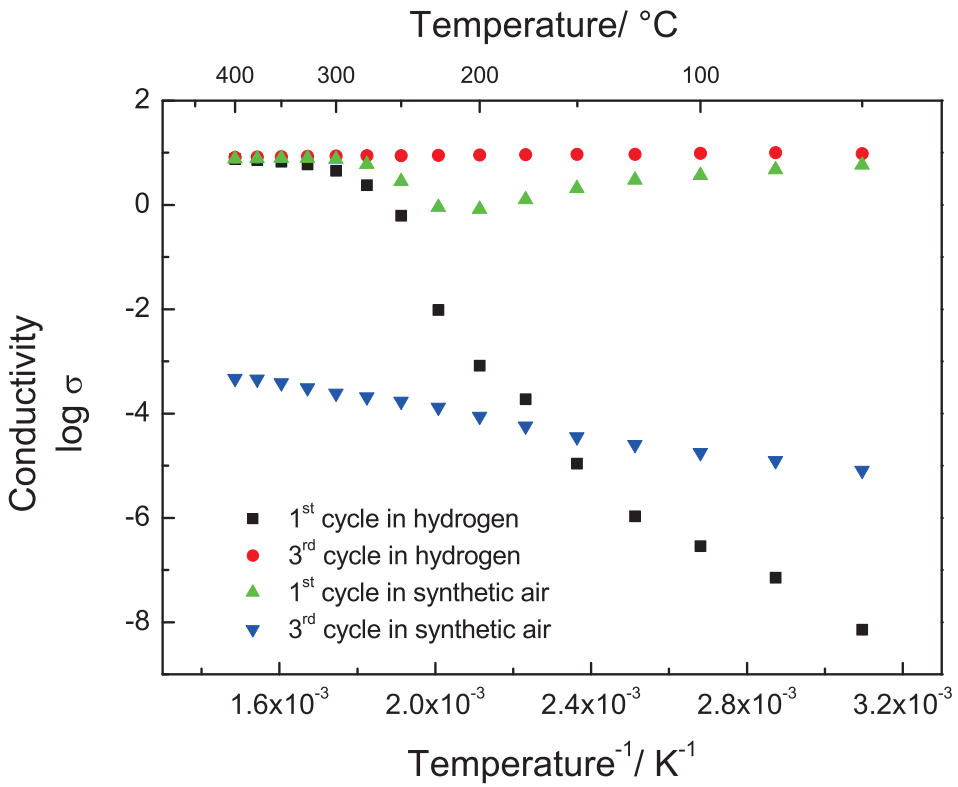

Figure 4.6: Temperature behavior for the first and third cycle in each atmosphere is shown. The measurements in hydrogen show a significant higher conductivity than the measurement in synthetic air (here as example the undoped ZnO nanoparticles).

oxygen result in hydroxyl groups on oxygen lattice sites (OH_O) and free electrons (e^-). The electrons generated by this process give an important contribution to the conductivity of the ZnO particles in hydrogen atmosphere compared to the measurements in synthetic air.

$$Zn_{Zn}^{x} + 2O_{O}^{x} + H_2(g) <=> Zn_{Zn}^{x} + 2OH_{O}^{\cdot} + 2e^- \tag{4.2}$$

In synthetic air the Nyquist plots show semicircles (except 16.79% Al and 37.6%) which can be seen in figure 4.7. The presence of semicircles implies that

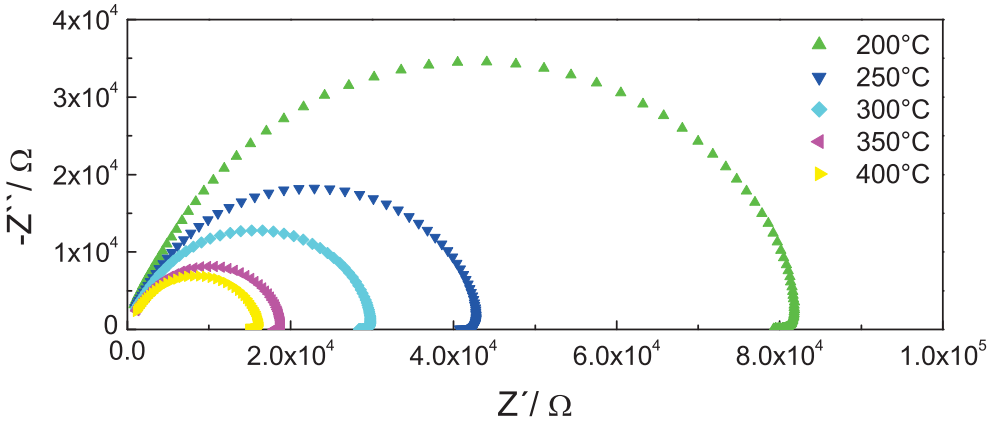

Figure 4.7: Nyquist plot for a selection of temperature for the measurements in synthetic air. An increase in conductivity with increasing temperature is observed and semiconducting behavior is found (here as example the undoped ZnO nanoparticles).

semiconducting transport processes are occuring in the system. The first cycle in hydrogen atmosphere has always a higher resistivity than the following cycles in the respective temperatures due to an annealing process which took place during the first heating ramp (see figure 4.6). The conductivity is about six orders of magnitude less compared to the measurements in hydrogen atmosphere. Other groups also observed an increase in conductivity by implanting hydrogen in ZnO thin films by five orders of magnitude [84]. Zhou et al. measured an increase of conductivity up to four orders of magnitude for hydrogen-implanted disc-shaped specimens [85] and theoretical calculations predict a shallow donor level in the ZnO which causes an increase in conductivity after hydrogen implanting [86]. The decrease in conductivity compared to the measurements in hydrogen atmosphere results from the release of the hydrogen atoms during the heating of the sample in synthetic air. This change in conductivity is observed for all undoped samples, as well as doped ZnO nanoparticles. After changing the environment from hydrogen atmosphere to synthetic air, the conductivity goes down some orders of magni-

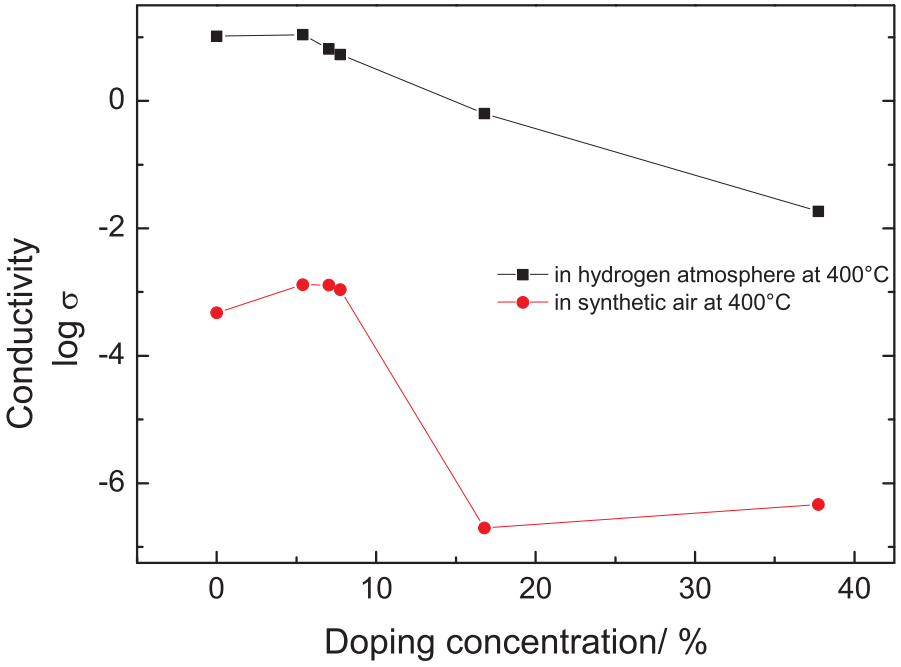

Figure 4.8: Conductivity for different doping concentrations of Al in ZnO in hydrogen atmosphere and in synthetic air.

tude. The same behavior is also observed for ZnO single crystals but not for ZnO nanoparticles so far [87].

The gaseous environment playes a big role in the transport process inside the ZnO nanoparticles. In figure 4.8 the conductivity as a function of the doping concentration at 400 °C is compared for the measurements in hydrogen atmosphere and in synthetic air. In hydrogen atmosphere the conductivity lies about two orders of magnitude higher than in synthetic air.

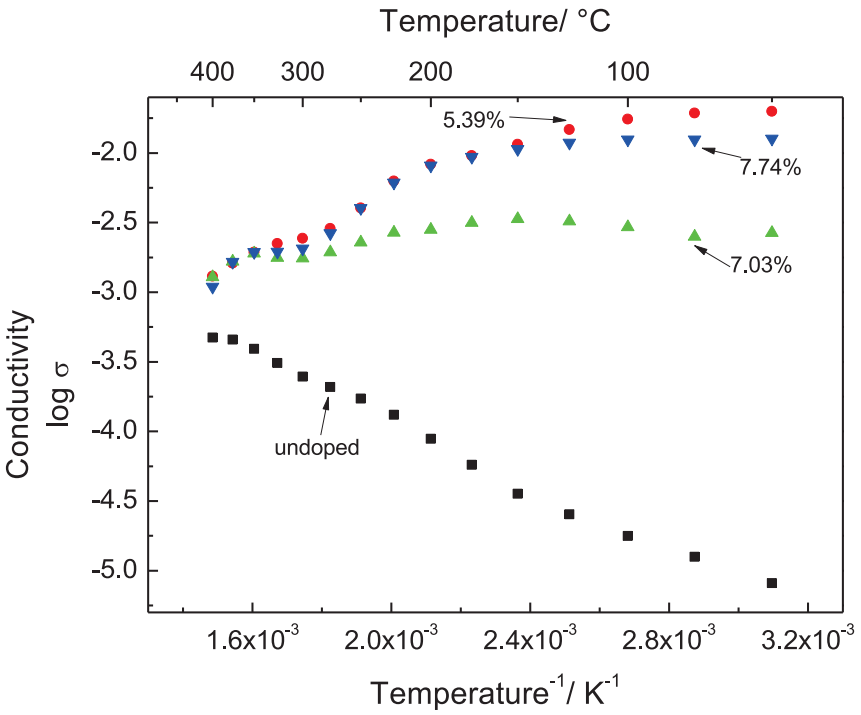

Figure 4.9: Conductivity for the aluminum doped ZnO nanoparticles in synthetic air (except the Al concentrations higher than 7.74%) as a function of the inverse temperature.

4.2.2 Influence of the aluminum doping of the ZnO nanoparticles

This chapter deals with the doping of ZnO nanoparticles with aluminum. The effect of different doping concentrations on the electrical properties are investigated in both, synthetic and hydrogen atmosphere, at different temperatures. In figure 4.10 the results for the measurements in hydrogen atmosphere are shown. The conductivity decreases with rising aluminum concentration and the samples doped with 16.79% and 37.63% of aluminum show conductivity values two orders of magnitude lower then all other doped materials. ZnO nanoparticles consist of

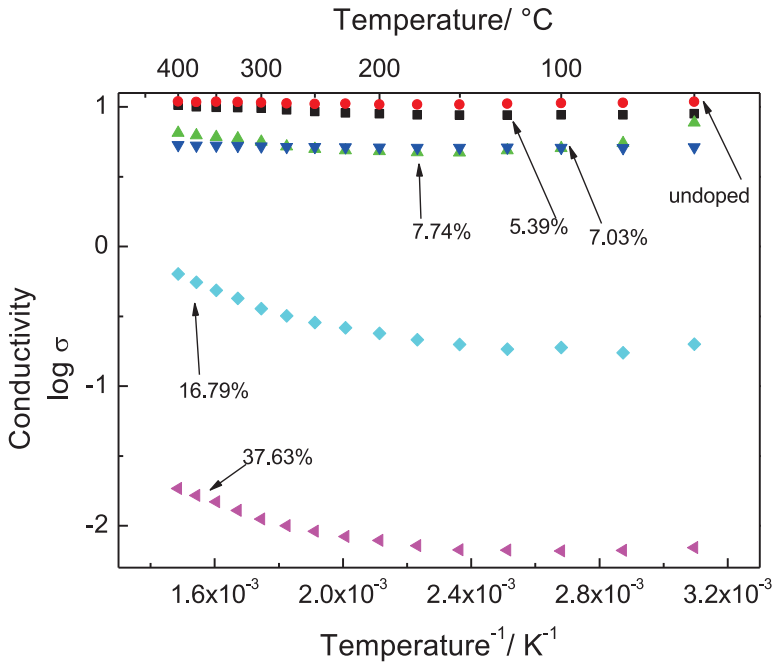

Figure 4.10: Conductivity as a function of the inverse temperature for aluminum doped ZnO nanoparticles in hydrogen atmosphere.

zinc and oxygen atoms at different lattice sites. A substitutional replacement of zinc ions in the lattice by Al ions or the incorporation of Al interstitials are possible. The incorporation of aluminum ions leads to the formation of free charge carriers, which can be described with the Kroeger-Vink-Notations (4.3) and (4.4):

$$2Al_2O_3 -> 4Al_{Zn}^{\cdot} + 4O_O^x + O_2(g) + 4e^- \tag{4.3}$$

$$2Al_2O_3 -> 4Al_i^{\cdots} + 3O_2(g) + 12e^-. \tag{4.4}$$

In hydrogen atmosphere the decrease of the overall conductivity with rising Al content is attributed to an increase in scattering processes at defects such as point defects (Al atoms) and extended defects (surfaces and interfaces). The charge carriers

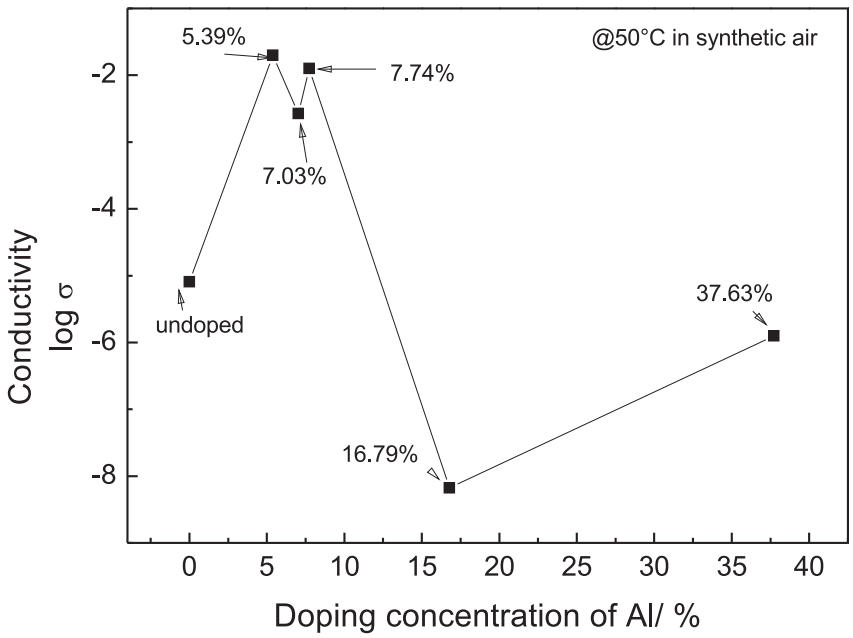

Figure 4.11: Conductivity as a function of the doping concentration of Al at 50°C in synthetic air.

resulting from the Al doping are thermally activated, and there are also charge carriers originating from the hydrogen doping in hydrogen atmosphere. In the lower temperature regime (175 °C) a positive temperature coefficient (ptc)conduction behavior in hydrogen atmosphere can be observed similar to a metallic-like transport behavior up to 7.7% of Al doping which comes from the hydrogen doping. Due to thermally activated charge carriers from the Al doping, the temperature coefficient switches, beginning from 175 °C and 37.6% Al the negative temperature coefficient behavior can also be observed above 200°C. Additionally, their comparably poor specific conductivity is caused by the strongly reduced crystallinity (see chapter 4.1).

In figure 4.9 the conductivity as a function of the temperature up to Al concentrations of 7.74% in synthetic air is shown. Doped ZnO nanoparticles with Al

content as high as 7.74% show very poor conductivity, which is compared with the low concentration doped ZnO nanoparticles in figure 4.11. This increase in conductivity can be explained by the increase of charge carriers due to the aluminum doping. The poor conductivity at higher Al contents is the result of a reduced crystallinity of the ZnO naoparticles. The conductivity of the material in air exhibits a distinct maximum at 5.39 - 7.74% of Al. A similar trend in conductivity has been observed for Al-doped ZnO films at a maximum of 4% of Al [35]. If one compares figures 4.4 and 4.11 the same trend can be seen. The smaller ionic radius of Al compared to Zn might be responsible for the decrease of the value of the lattice constant c with increasing Al level. The trend of the lattice constant a (first increases and then decreases) is more difficult to explain. Possibly, Al atoms preferentially occupy particular lattice sites at lower Al doping concentrations. The increase of Al concentration above a certain threshold limit (above 7.74%) forces Al atoms to occupy other lattice sites [32]. The lattice parameter a and the conductivity in synthetic air follow the same trend. The incorporation of Al atoms into the ZnO lattice causes a change of the lattice constant a and therefore a careful correlation between the site of the dopant atom and the conductivity can be made.

4.2.3 Influence of moisture

In this chapter the influence of moisture on the electrical properties of ZnO nanoparticles is presented. It is known, that ZnO nanoparticles synthesized in a hotwall reactor grow in moisture atmosphere [32]. Its influence on the electrical conductivity of ZnO nanoparticles was investigated, but the reproducibility and long-term measurements are not reported [88–91]. The thickness of the disks used for the impedance measurements is about 0.12 mm, and is handled like explained in chapter 3.4.2.1 and 3.4.2.2 for the measurements of the aluminum doped ZnO nanoparticles. The measurments are run under the same conditions as explained in chapter 3.4.2.2. During the first ramp, the impedance data are measured in argon atmosphere. Then the pellet is cooled down to 50 °C in argon atmosphere.

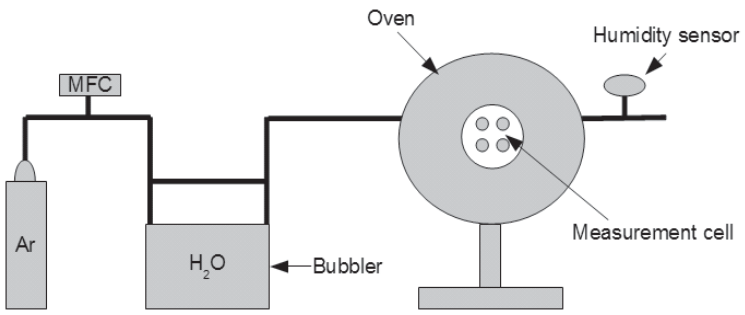

Figure 4.12: Set-up for the measurements at different relative humidity.

Similarly, the second and the third ramp are performed under the same conditions. Then the moisture is added using a water bubbler. An argon flow of 100 sccm is directed first through the water bubbler and then into the chamber (see figure 4.12). By heating the water bubbler the moisture level can be changed and the relative humidity (rH) is measured inside the chamber using a commercial humidity sensor (Hygrosens FF-IND-20mA). Dry atmosphere is achieved bypassing the

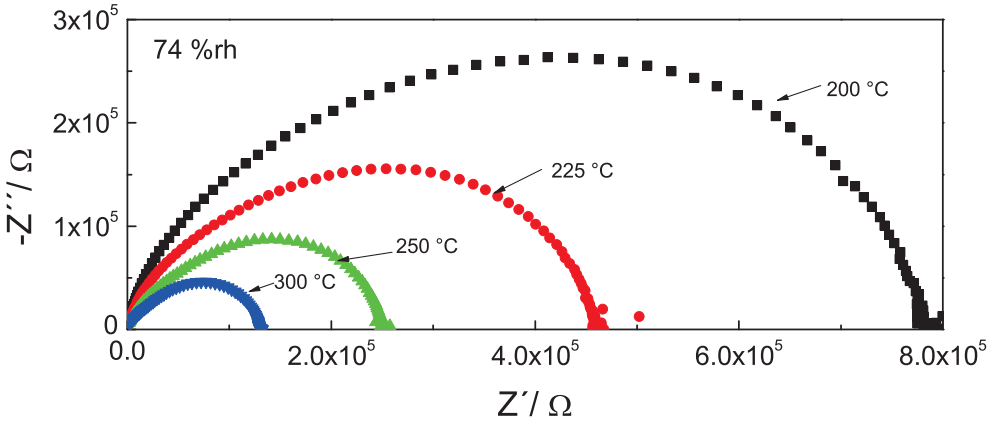

Figure 4.13: Nyquist plot for the measurements at different temperatures at 74 %rh.

bubbler with a flow of 100 sccm of argon. The relative humidity is adjusted first to 0 % rH (for dry argon atmosphere) and then to 56 % rH, 74 % rH, 97 % rH and 100 % rH. When the measurements at 100 % rH are finished, the relative humidity in the chamber is set to 69 % rH. The bubbler was disconnected from the water bubbler after the measurements at 69 % rH were finished and dry argon atmosphere with 0 % rH is achieved in the chamber again. Then the conductivity is measured again in dry argon atmosphere. The measured impedance spectra in moisture and dry argon exhibit semi-circles which are typical for semiconductors and expected for ZnO nanoparticles. In figure 4.13 selected Nyquist plots can be seen from the measurements at 74 % rH. For all other humidity concentrations and temperatures the same shape is observed. The Nyquist plot for the measurements at different moisture levels at 200 celsius is shown in figure 4.14 as example for all other moisture concentrations. In figure 4.15 the specific conductivity of the ZnO samples is plotted as a function of the inverse temperature for different moisture contents. The data are computed from the real part of the impedance (Z') measured between 10 Hz and 250 kHz. For the data points in figure 4.15 the values of the impedance at 177 Hz are used (any other value between 10 Hz and

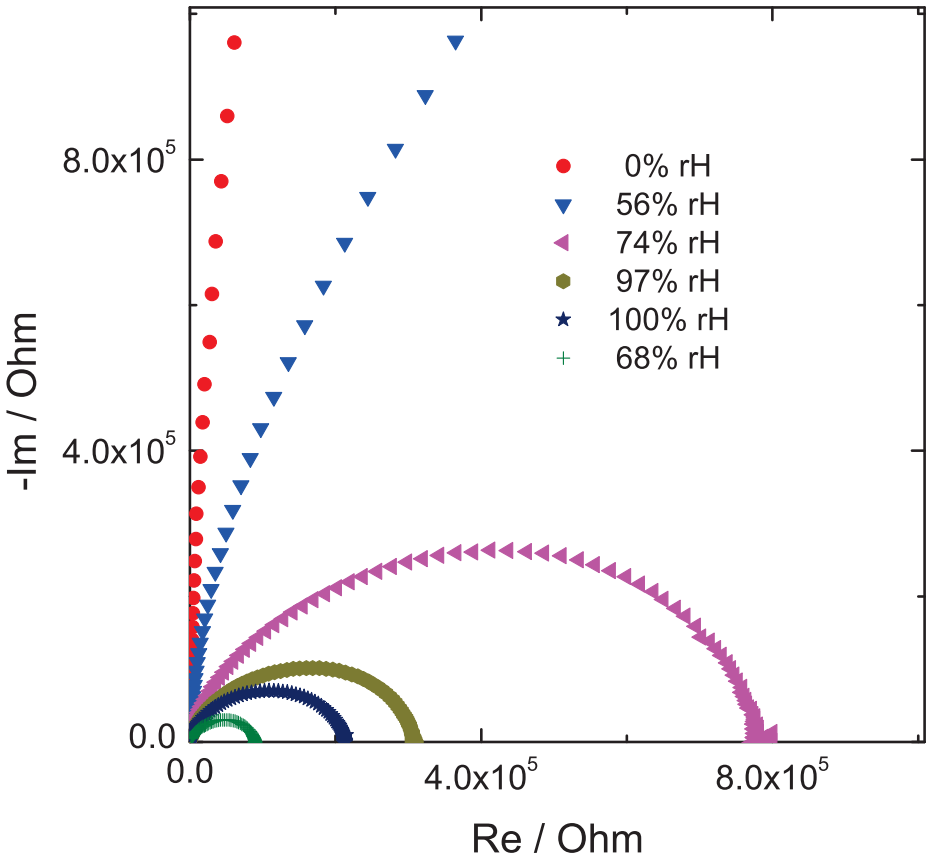

Figure 4.14: Conductivity as a function of the temperature for aluminum doped ZnO nanoparticles in hydrogen atmosphere.

250 Hz could be used due to the present DC-conductivity in this regime). In this frequency range, a pure DC-conductivity is found. The conductivity is plotted as a function of the inverse temperature for the different measured relative humidity concentrations up to 100 % rH for the first time. The conductivity increases with higher relative humidity due to the adsorption of water molecules on the surface of the ZnO nanoparticles, which ultimately leads to the formation of $Zn(OH)_2$. Due to a dissociative chemisorption, a displaced double ionized oxygen atom from the lattice reacts with protons originating from the dissociation of H_2O molecules

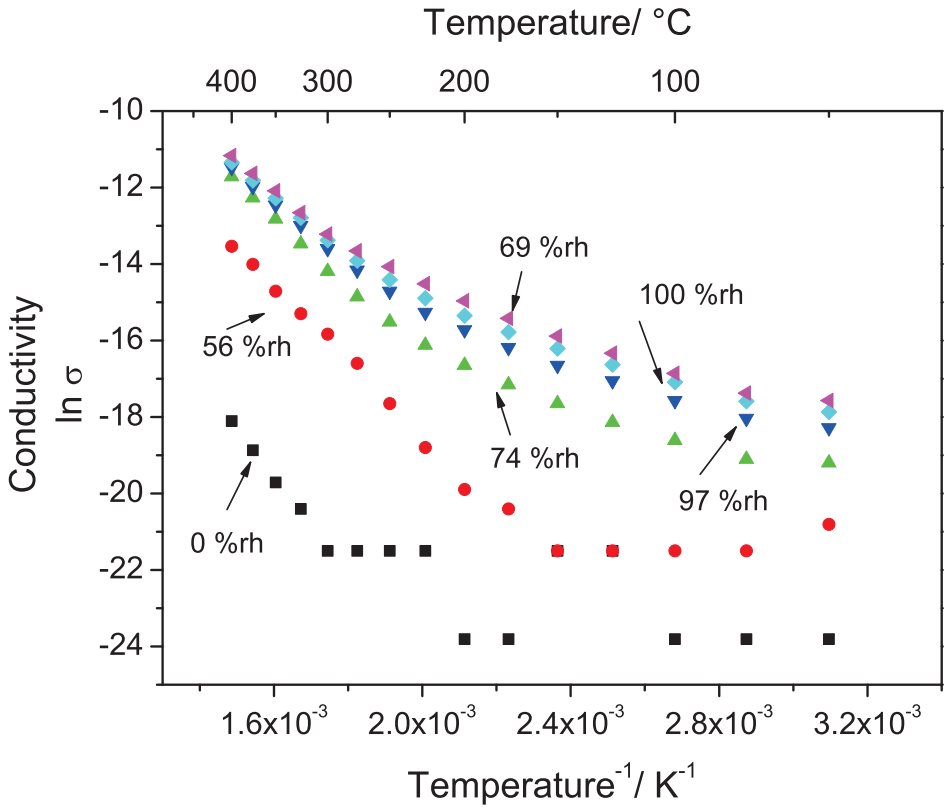

Figure 4.15: Conductivity as a function of the temperature for all moisture concentrations.

leading to two hydroxyl groups and releasing two electrons as shown in equation 4.5. As a result, the conductivity increases due to the accumulation of electrons at the surface [92].

$$2O_O^x + H_2O <-> 2OH_O^{\cdot} + \frac{1}{2}O_2 + 2e^{-}. \tag{4.5}$$

Additionally, it is known from literature, that the water molecules in the physisorped monolayer form hydrogen bridge bonds with additional water molecules. In the Grotthus chain reaction model [93], these water molecules can accept protons from the hydroxyl groups and the proton can move freely in the layer. This

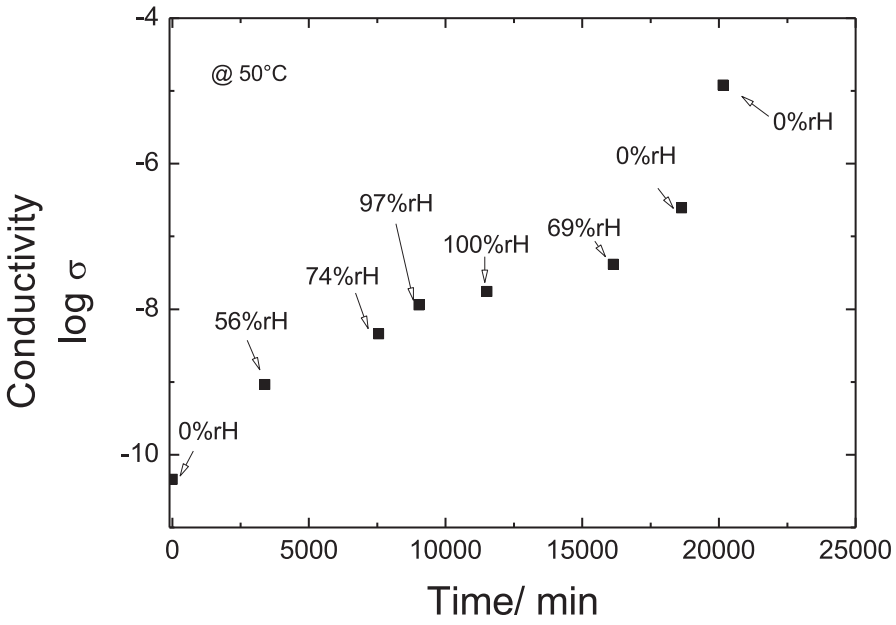

Figure 4.16: ZnO nanoparticles for different relative humidity. The conductivity still rises after removing any moisture from the system.

mechanism increases the proton conductivity and it enables for a further increase in electronic conductivity as every proton released from a surface hydroxyl group creates one electron.

By exposing the samples to 69 % rH after measuring at 100 % rH with high humidity concentrations, a decrease in conductivity is expected. Instead, the opposite behavior is observed. Figure 4.16 shows the conductivity for the different humidity concentrations at 50°C as a function of the sequence of the measurements. The measurements still show an increase in conductivity even after turning off the water bubbler and decreasing the relative humidity down to zero. After measuring the conductivity at the different moisture levels from 0 % rH to 100 % rH, the relative humidity is decreased down to 69 % rH and the sample is measured at this moisture level. Then the water bubbler was disconnected and pure, dry argon was flowing

through the measurement cell again. After reaching the 0 % rH the conductivity was measured again and surprisingly it was still increasing. After one day of dry argon purging the conductivity was still increasing. A decrease of the conductivity after decreasing the moisture level is expected but the conductivity is still increasing. An explanation for this behavior could come from the XRD pattern from the ZnO nanoparticles and from those annealed during the treatment in humid atmosphere (see 4.17). The Bragg reflections and the effect of the narrower reflec-

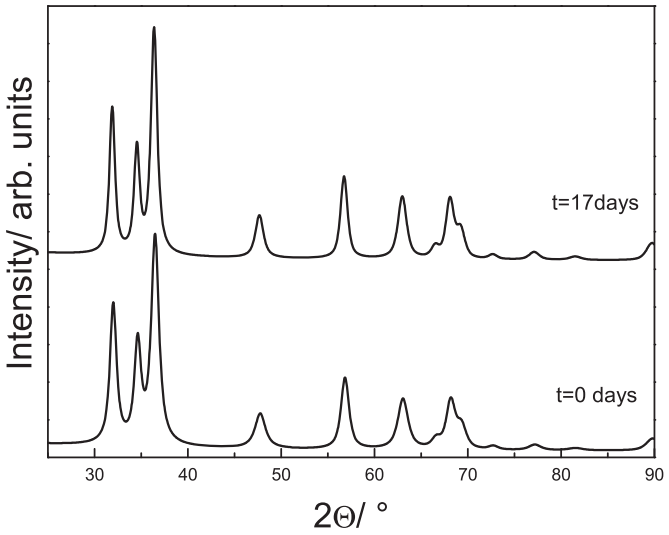

Figure 4.17: XRD pattern of ZnO nanoparticles before and after exposure to humid atmosphere. The Bragg reflections are getting narrower for the humidity exposed ZnO particles.

tions indicate an increase in crystallite size from Rietveld refinement from 13.3 nm to 17.6 nm [32]. Ali et al. found that the chemisorption of water molecules and the generation of hydroxyl groups in combination with interstitial oxygen, oxygen and zinc vacancies are responsible for the production of new ZnO layers and therefore the growth of the ZnO nanoparticles. The highest mobility of the point defects in the crystal structure have interstitial zinc atoms followed by interstitial oxygen atoms, zinc vacancies and oxygen vacancies [94]. The diffusion energy for the nanocrystals is lower compared to the diffusion energy for bulk ZnO, which

makes the diffusion process possible at 50 °C. The coexistance of hydroxyl groups and unprotonated oxygens may produce new ZnO layer. Related to the described growing process, the observed electrical behavior at different moisture concentrations can be explained as follows: due to the growth of the particles, the volume to surface ratio is adjusted to less surface area compared to the volume of the ZnO nanoparticles. The smaller surface area produces less and better particle-particle contacts. The decreasing number of particle-particle contacts cause a decrease in resistivity. After decreasing the humidity concentration the conductivity is still increasing. The ZnO nanoparticles grow due to the physisorped water molecules. In combination with zinc interstitials (Zn_i), new ZnO layer can be produced as described above. They show that the larger the particles, the smaller the volume density of particle-particle contacts in the sample. The growing process and therefore the conductivity improvement saturates if the dissociation of water molecules come to an end or the supply of defects is depleted.

5 Results and discussion for ZnO nanoparticle films

The previous findings obtained for the ZnO nanoparticles suggested the idea to build a simple gas-sensitive thin film produced by ink-jet printing made of ZnO nanoparticles synthesized with CVS. The main advantage of using ink-jet printing techniques is the possibility to deposit a small volume of ink precisely on demand without using a mask. The ink can also be handled without any extensive precautions. Some points have to be taken into account such as agglomerate size (for preventing clogging cartridges) and time-stability over a long time period. Also, drop spacing, firing voltage, frequency and plate temperature have to be optimized. If the optimal parameters are found, the ink can be fabricated with low costs, and the printing is very easy and fast to perform. In this chapter, the steps from the production of a stable ZnO dispersion until the testing of the hydrogen sensitivity of the ink-jet printed ZnO film is discussed.

5.1 Dispersion

The ink has to be stable as long as possible and must suit the structural requirements like particle size and agglomeration size to the nozzle of the printer. The ZnO nanoparticles are synthesized by CVS, (see chapter 3.3.3). The crystallite size measured by XRD is about 20 nm immediately after synthesis. Dispersions consisting of water and 7 wt% of ZnO are not stable, as it can be seen in figure 5.1c. In this figure the crystallite size given by the XRD measurements is also shown. By dispersing the ZnO nanoparticles in water, the agglomeration size of the particles increases up to 90 to 100 nm(DLS measurements). The agglomeration size has to be smaller than 200 nm because of the possible cartridge nozzle clogging. In figure 5.1c one can see the zeta-potential as a function of the pH. The zeta potential of the dispersion only made from water has a low zeta-potential. Three

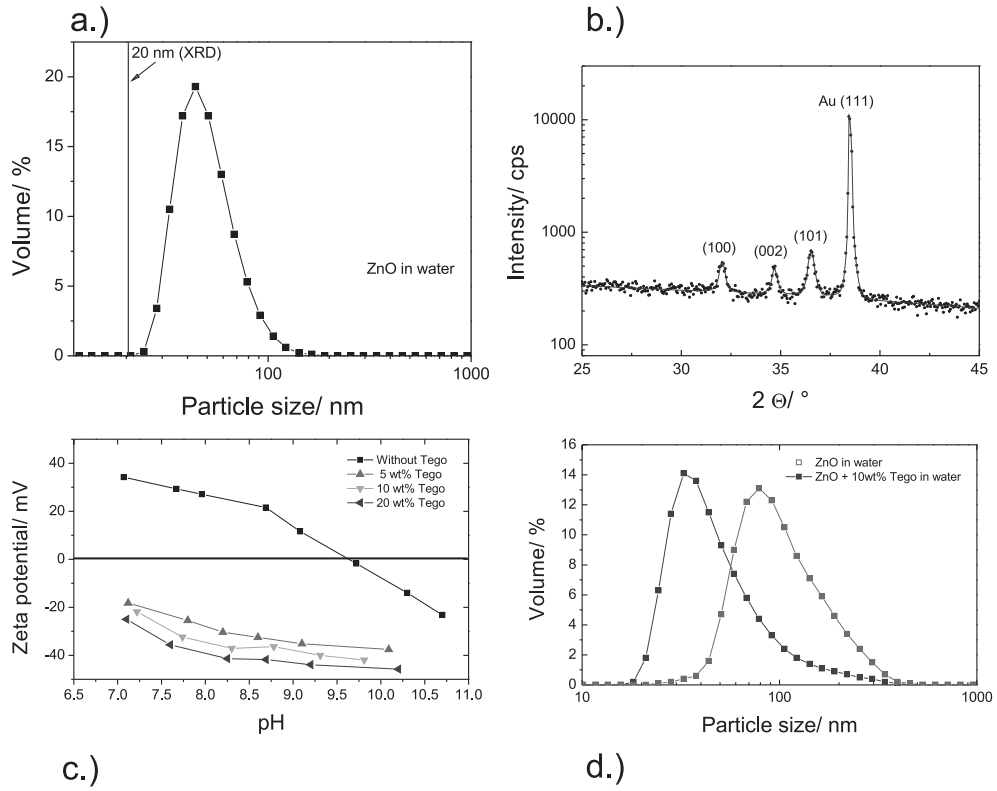

Figure 5.1: a.) Agglomerate size of the particles (DLS measurements) in the water-based dispersion and the crystallite size of the ZnO nanoparticles before the preparation of the dispersion. b.) XRD pattern of the ink-jet printed ZnO film based on the water dispersion with TEGO. c.) Zeta-potential of the different dispersions. d.) Comparison of the agglomeration size (DLS measurements) for the aquatic dispersion and the dispersion with additional TEGO.

more zeta-potential measurements can be seen in this figure, and they consist of ZnO nanoparticles in water with different concentrations of some polymeric stabilizer (5 wt%, 10 wt% and 20 wt% (TEGO (polyacrylic acid + sodium polyacrylate, Degussa)). For these three dispersions a much higher zeta-potential is observed and also the agglomeration size (shown in figure 5.1d) is decreased. The mean particle size estimated after fitting the data turned out to be about 44 nm, while

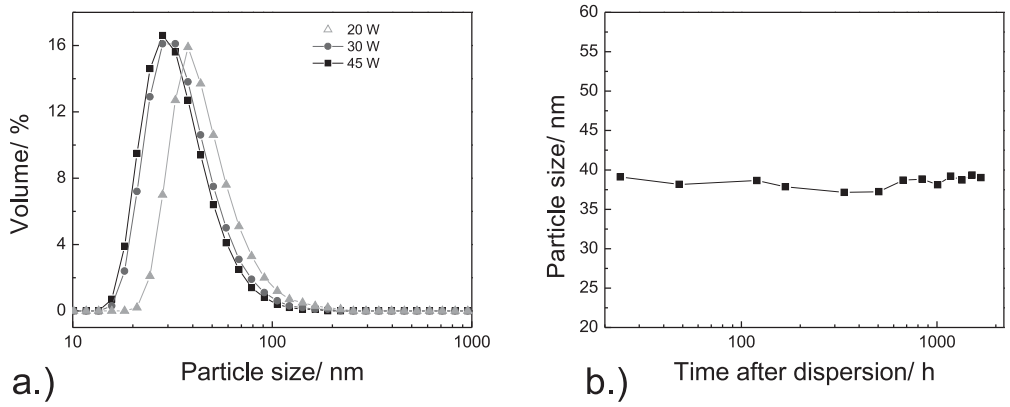

Figure 5.2: a.) Comparison of the agglomeration size of the dispersions with TEGO for different sonication power. b.) Stability of the dispersion (with 20 wt% of TEGO).

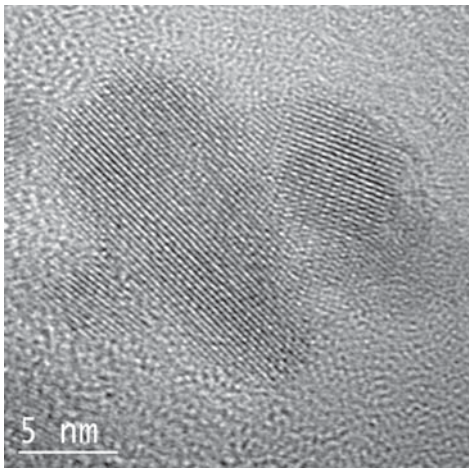

Figure 5.3: TEM picture for a dispersion produced with 20 wt% of TEGO.

the primary particle size estimated from XRD is about 20 nm. The XRD pattern can be seen in figure 5.1b. It clearly shows that the size of the particles in the ink

is very close to the size of the primary particles. Using TEGO as stabilizer, the dispersion is stable for several months (see figure 5.2) without any observable sedimentation. The dispersions with TEGO and especially the resulting agglomerate size is affected by the sonication power. The mixture of ZnO particles, water and TEGO is sonicated for different times to get the best dispersion. In figure 5.2 three different curves are shown which result from the difference of the used sonication power. At least a sonication power of 30 W is necessary to get the desired particle size. Also, the duration of the sonication process plays a role in the quality of the dispersions as shown in figure 5.2b. A ZnO ink of high quality can be produced as follows: the ZnO dispersions are produced from a mixture of 20 wt% of TEGO in water added to the ZnO powder. The mixture has to be sonicated at least at 30 W for more than 2.5 hours, otherwise agglomerates like the one shown in figure 5.3 would form. The dispersions have to be filtered (200 nm pores) due to the restricted diameter of the nozzle.

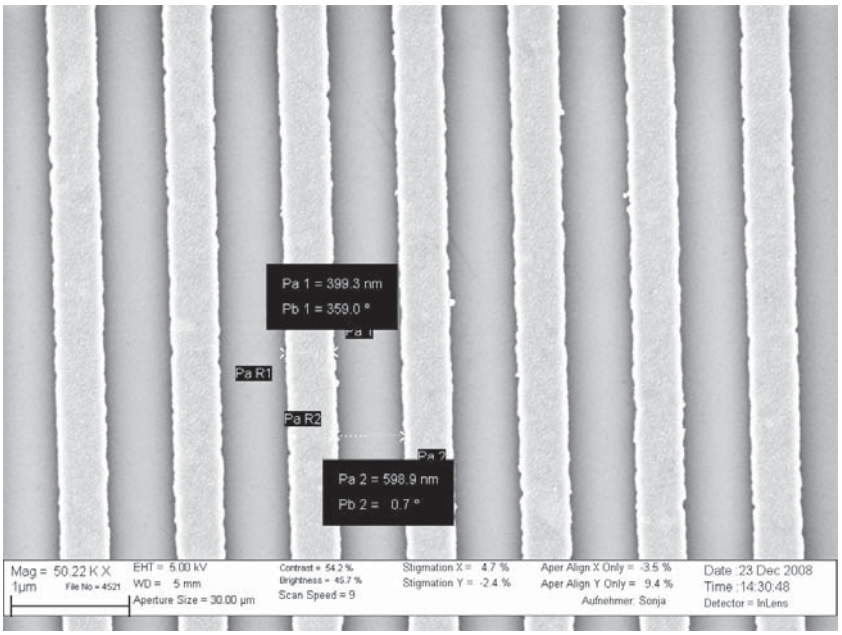

Figure 5.4: Enhanced SEM picture of a part of the interdigital structure.

5.2 Printing process and resulting sensor

The contacts of the interdigital capacitors consist of evaporated gold (for details see 3.4.3). The distance between the conductive paths is about 400 nm. In the SEM picture 5.4 a part of the interdigital structure is shown. The conductive paths have a spacing of about 600 nm and a width of almost 400 nm. The interdigital structure (dark grey) consists of several gold fingers which are not connected to each others. The SEM picture in figure 5.5 shows the whole interdigital structure where the ink-jet film will be printed on. The substrate where the film is to be printed must be tested before the printing process in order to make its surface hydrophilic and to remove all surface contanimations. This cleaning process is performed by treatment in piranha solution followed by washing in deionized water. The drying of the substrates is done with nitrogen. The printer device is a Dimatix 2800 ink-

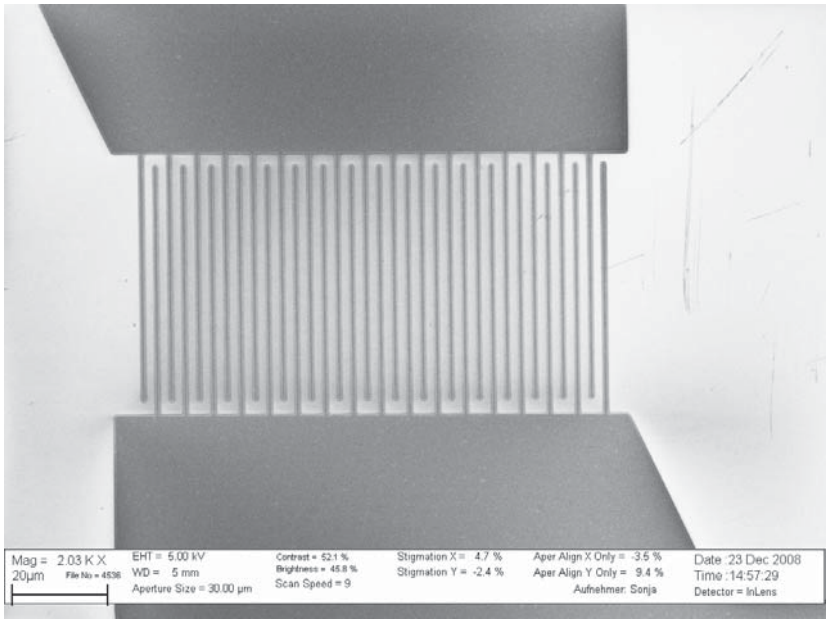

Figure 5.5: SEM picture of an interdigital structure on a SiO_2 substrate used for printing.

jet printer. During the printing process a frequency of 3 kHz and a firing voltage of 30 V are used. The substrate is placed on plates heated at 40 °C to remove the remaining solvent. The dispersion is filtered (200 nm pores) and used to fill the cartridge. The cartridge is filled with 1.5 mL and produces 10 pL droplets. The so obtained films are smooth and crack free, and a thickness between 100 nm and 250 nm can be obtained. By using always the same printing parameters, a high reproducibility of ink jet printed films can be achieved. The substrate with the interdigital structures on top is placed in a chip carrier. With the help of this chip carrier, the specific interdigital structures can be contacted via ultrasonic bonding and measured in the measurement cell for thin films. The impedance measurements are performed with a Solatron SI1255 in connection with a dielectric interface. The impedance measurement are performed between 25 °C and 200 °C in ambient air and in hydrogen atmosphere in the frequency range from 10 Hz -

10 MHz. The maximum temperature (200 °C) is limited by the glue fixing the substrate in the chip-carrier.

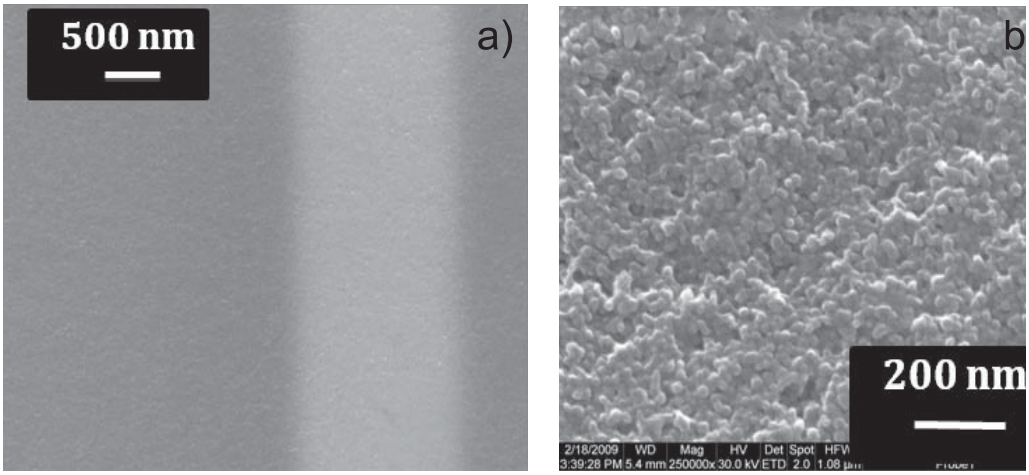

Figure 5.6: a) SEM picture of a part of the ink-jet printed film. One of the Au-paths can be seen. The film is very smooth and crack-free. b) SEM picture of the surface of the ink-jet printed film.

5.3 Hydrogen sensitivity of ink-jet printed ZnO films

The structural analyses after the ink-jet printing process shows a crystallite size of 36 nm. This increase of crystallite size of the particles compared to the initial crystallite size (20 nm) can be explained with a growing process of the ZnO nanoparticles in moisture (chapter 4.2.3). The ink-jet printed ZnO films have a high contact area and many particle-particle contacts which are required for electronic applications [95]. The film is very smooth and crack-free as it can be seen in figure 5.6a. In figure 5.7 some of the Nyquist plots for different temperatures in ambient atmosphere are reported. By increasing the temperature of the sample, the conductivity increases: this behavior is typical for semiconductors [59]. The increase in conductivity can be explained by a thermally-activated charge carrier transport in the particles. In hydrogen atmosphere the same temperature dependence is observed as it can be seen in figure 5.8. The activation energy of the ink-jet printed films is calculated from the slope obtained from the Arrhenius diagrams with the following relation in equation (5.1) where σ is the conductivity,

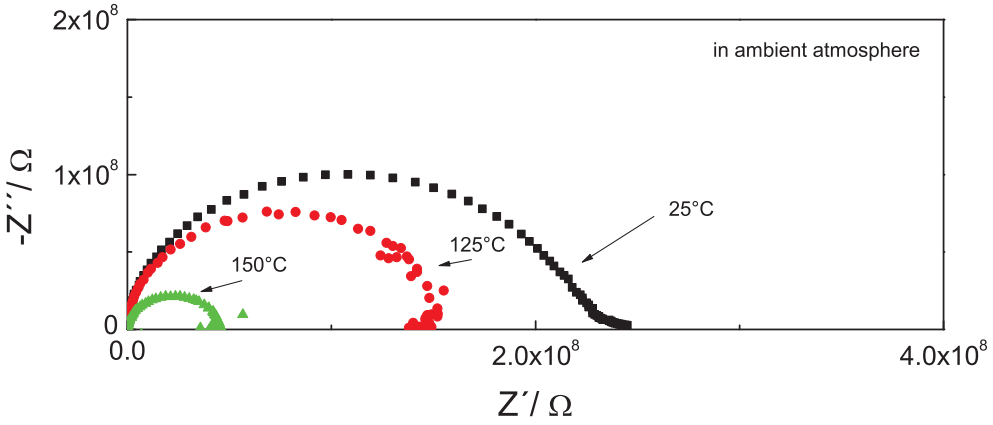

Figure 5.7: Nyquist plot of the measurements in ambient atmosphere at different temperatures.

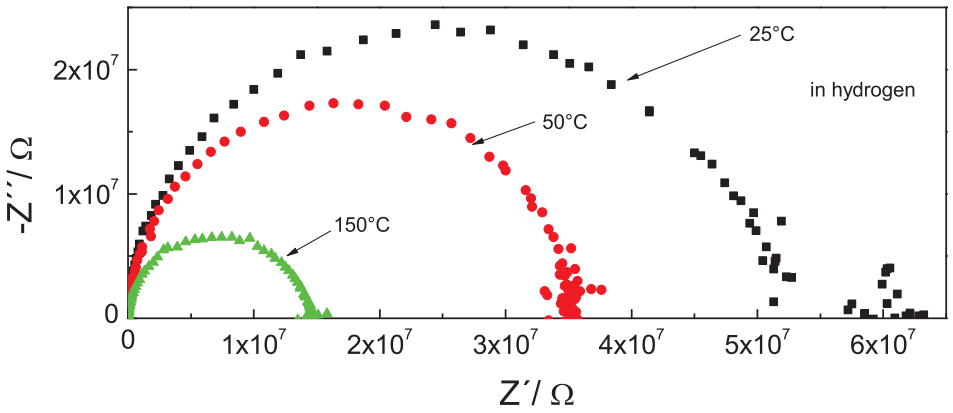

Figure 5.8: Nyquist plot of the measurements in hydrogen atmosphere at different temperatures.

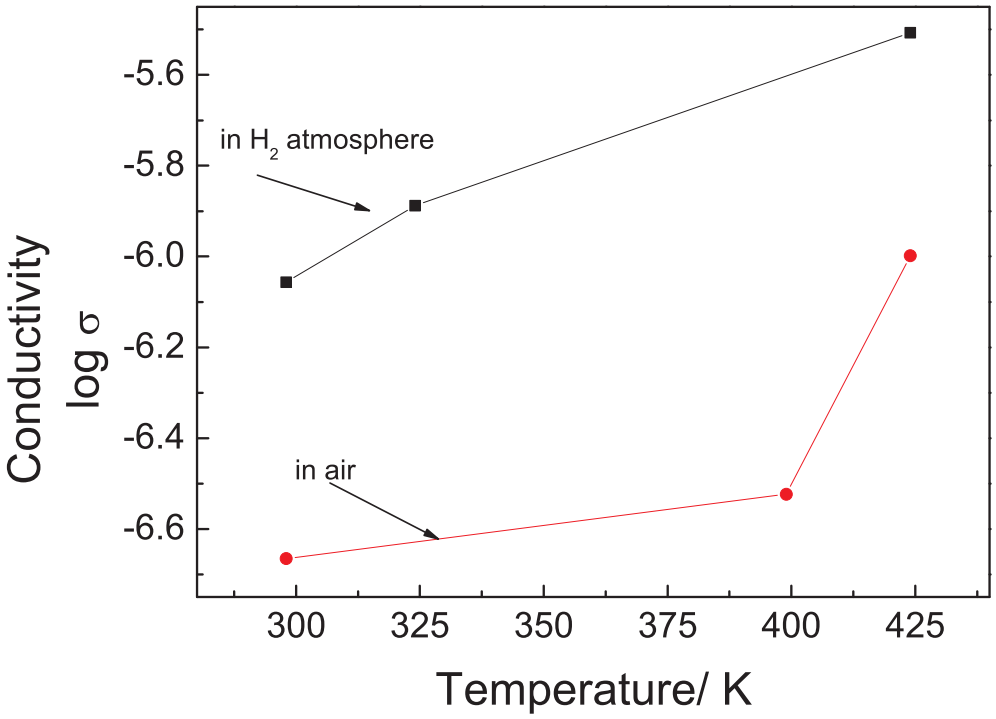

Figure 5.9: Conductivity as a function of the temperature in ambient and hydrogen atmosphere.

k_B is the Boltzmann constant, T the temperature and E_A the resulting activation energy:

$$\sigma = \sigma_0 \exp(\frac{-E_A}{k_B T}). \tag{5.1}$$

The activation energy of the sample at ambient atmosphere is about 101 meV, and for the measurements in hydrogen an activation energy of 108 meV is observed. In figure 5.9 the conductivity as a function of the temperature is plotted for the measurements at ambient atmosphere and in hydrogen. The increase of the conductivity in hydrogen atmosphere can be explained by a generation of free charge carriers due to the doping-like process explained in more detail in chapter 4.2.1 [40, 82]. The same sample exhibits a four times higher conductivity for measurements in hydrogen atmosphere compared to ambient atmosphere already at room temperature. This behavior shows a high potential even for applications at room

temperature. As sensing material, another very promising result is that no pre-annealing of the film is required because the packaging of the nanoparticles after the ink-jet printing process and the distance of the contact paths are already good enough to perform sensor measurements. The whole process is also reversible, except some very small differences after the first heating cycle attributed due to a very small annealing processes in the particle film.

6 Results and discussion for silicon nanoparticles

In this chapter, silicon nanoparticle powders synthesized in a microwave reactor are investigated with respect to their electrical properties. The average size is about 50 nm. The samples are investigated in air and in hydrogen atmosphere. As the next step, the silicon nanoparticles are etched to remove their oxide shell. This decreases the electrical resistivity and the conductivity rises up. The disadvantage of Si is the reoxidation due to its affinity to oxygen. A method has to be found to inhibit the etched silicon nanoparticles to reoxidize again. This is done by surface functionalization with different alkenes. The influence of the alkenes on the electrical properties of the particles is reported in this chapter. The discussion of the transport mechanism of silicon nanoparticles based on Mott's theory concludes this work.

6.1 Electrical properties of as-prepared silicon nanoparticles

The silicon nanoparticles investigated in this work have a mean particle size of 50 nm. In figure 6.1, the conductivity of undoped silicon nanoparticles as a function of the inverse temperature can be seen. The samples are measured three times in each atmosphere. For all conductivity plots and calculations of the activation energy only the third cycles are used. The first cycle always shows an increase of the conductivity which remains high when the sample is cooled down again. This effect can be explained by an annealing effect during the first heating ramp. The higher conductivity of the silicon nanoparticles compared to the untreated particles is caused by an annealing process during the heating process. For the second and the third cycle the same high conductivity is observed. Because the second and the third cycles always show the same values, the values of the third cycles are used for calculating for example the activation energy E_A of the material. For

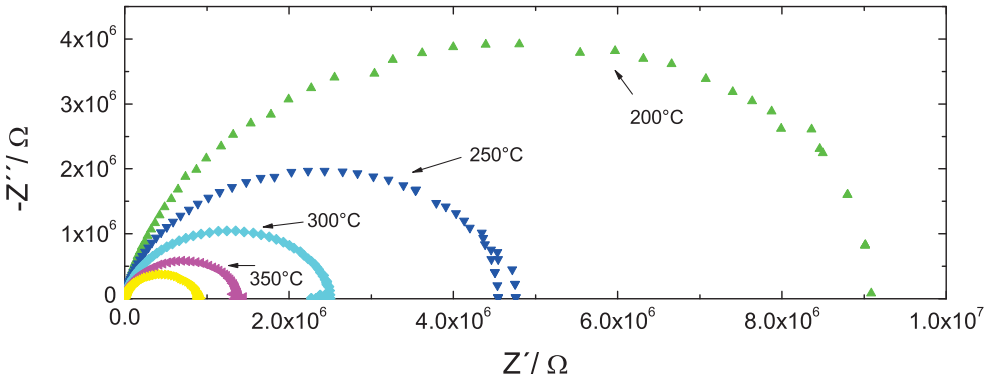

Figure 6.1: Nyquist plot of as-prepared silicon nanoparticles for a selection of temperatures in air.

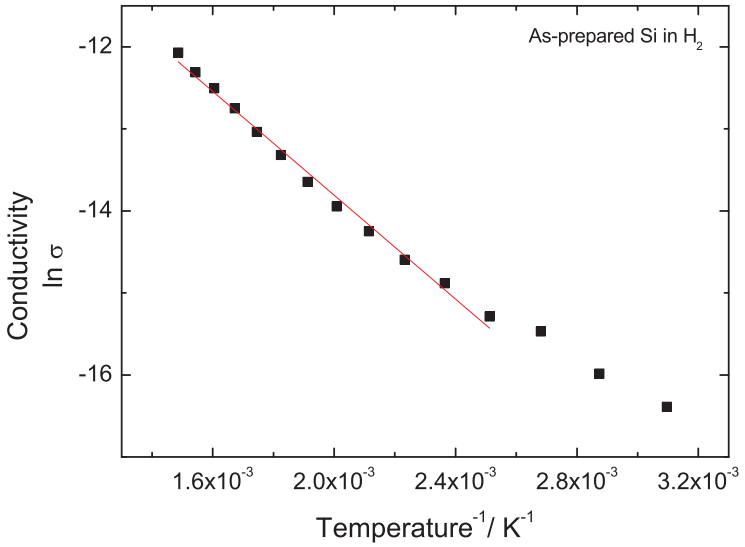

Figure 6.2: Arrhenius plot of as-prepared silicon nanoparticles with the fit for the calculation of the activation energy E_A.

all measured as-prepared silicon nanoparticles the thermally activated transport energy E_A is about 272 meV as can be seen in figure 6.2. In figure 6.3 the real part

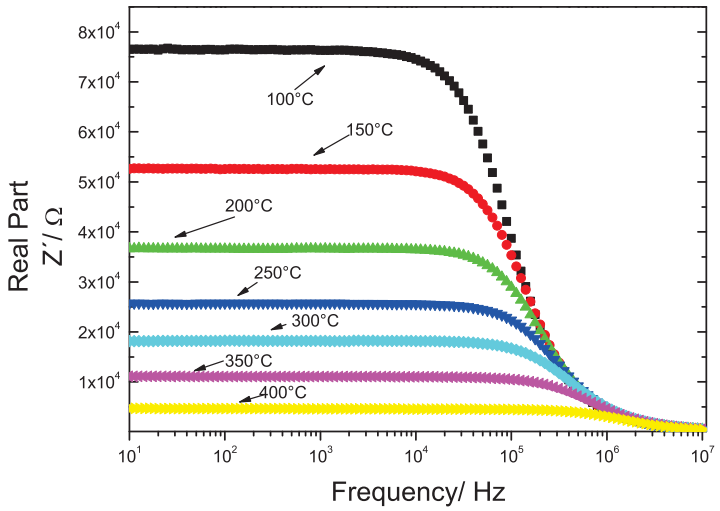

Figure 6.3: Overview on the resistivity of as-prepared silicon nanoparticles measured in hydrogen atmosphere.

of the impedance is shown as a function of the frequency for several temperatures. All these data points are extracted from the third measurement cycle as explained before. In this graph the increase in conductivity with rising temperature can be seen clearly. The conductivity for the measurement at 400 °C is about 15 times higher compared to measurements at 100 °C. All following electrical measurements on silicon nanoparticles, no matter if as-prepared, etched or functionalized, show the same behavior as the example shown in figure 6.3.

6.2 Electrical properties of etched silicon nanoparticles

In this chapter, the electrical properties of etched silicon nanoparticles are presented. The natural oxide shell at the surface of the silicon nanoparticles is removed with hydrofluoric acid (HF). Afterwards, the surface is hydrogen terminated. The etched particles are sensitive to ambient atmosphere and have to be handled quickly in this environment to prevent a regrowing of an oxide shell. This will be explained in this chapter more deeply. In figure 6.4, Fourier transformed infrared spectroscopy (FTIR) for as-prepared, freshly etched and aged etched silicon nanoparticles are shown. For the as-prepared particles the asymmetric stretching peak SiO_x between the wavenumbers 1075 and 1200 cm^{-1} can be seen very clearly. The stretching peaks of H-Si with silicon back banded to oxygen (H-Si-O-Si) between 2200 and 2300 cm^{-1} occur also due to the existing oxide shell around the silicon particles. After the etching process, the freshly etched particles are measured directly with the FITR to keep the reoxidation as small as possible. The FTIR spectra for the freshly etched particles show no peaks coming from the silicon-oxygen bonds anymore. The SiH_x peaks occurring at 2100 cm^{-1} come from the hydrogen termination of silicon surface atoms back bonded to silicon (H-Si-Si) as it is received by the etching process using HF. The etched particles are stored in ambient atmosphere for one day and measured again using the FTIR to see any reappearance of oxide which would give any information about a reoxidation of the particles. The lowermost FTIR spectrum in figure 6.4 represents the measurement on the silicon particles etched and stored in ambient atmosphere for one day. The regrowing oxide shell is represented by the reappearing SiO_x asymmetric stretching peaks and a decrease of the intensity of the SiH_x peaks from the hydrogen termination of the surface of the particles. The hydrogen termination of the silicon nanoparticles decreases due to the fact that the oxide shell is regrowing around the surface and replaces the hydrogen atoms. The results from the following electrical measurements can be explained nicely with the results from the FTIR measurements. In figure 6.5, the conductivity as a function of the inverse temperature can be seen for etched silicon nanoparticles. To compare the different conductivities of the (aged and) etched particles and as-prepared particles, the conductivities for these samples are shown. The etched silicon nanoparticles show a more than three

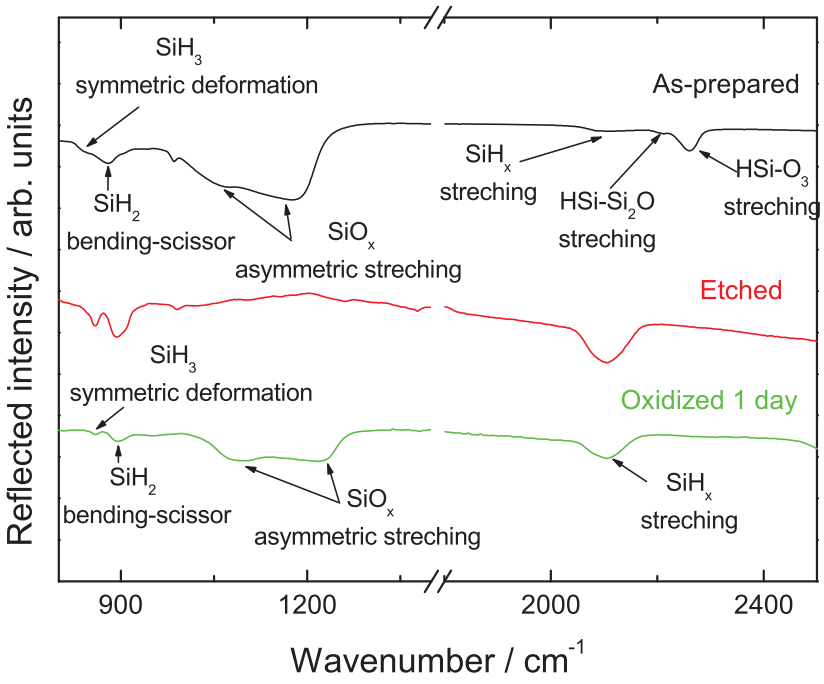

Figure 6.4: FTIR spectra of as-prepared and etched silicon nanoparticles. The reoxidation of the particles is observed very clearly, especially one day after the etching process took place.

orders of magnitude higher conductivity compared to the as-prepared particles. By removing the oxide shell around the silicon core, the transport of the electrons between the particles needs much less energy. The electrons do not have to pass the oxide shell anymore. The disadvantage of the etched silicon nanoparticles is the regrowth of the oxide shell in ambient atmosphere after the removal of the oxide shell and the resulting lower electrical conductivity compared to the freshly etched nanoparticles. In figure 6.5 the electrical measurements for the etched silicon nanoparticles 27 days and 188 days after the etching process can be seen. All samples are etched at the same time but stored for different durations in ambient atmosphere to see the influence of the regrowing oxide shell on the conductivity of the particles. The measurement for the silicon particles 26 days after the etching process shows a clear decrease in the conductivity compared to the freshly etched

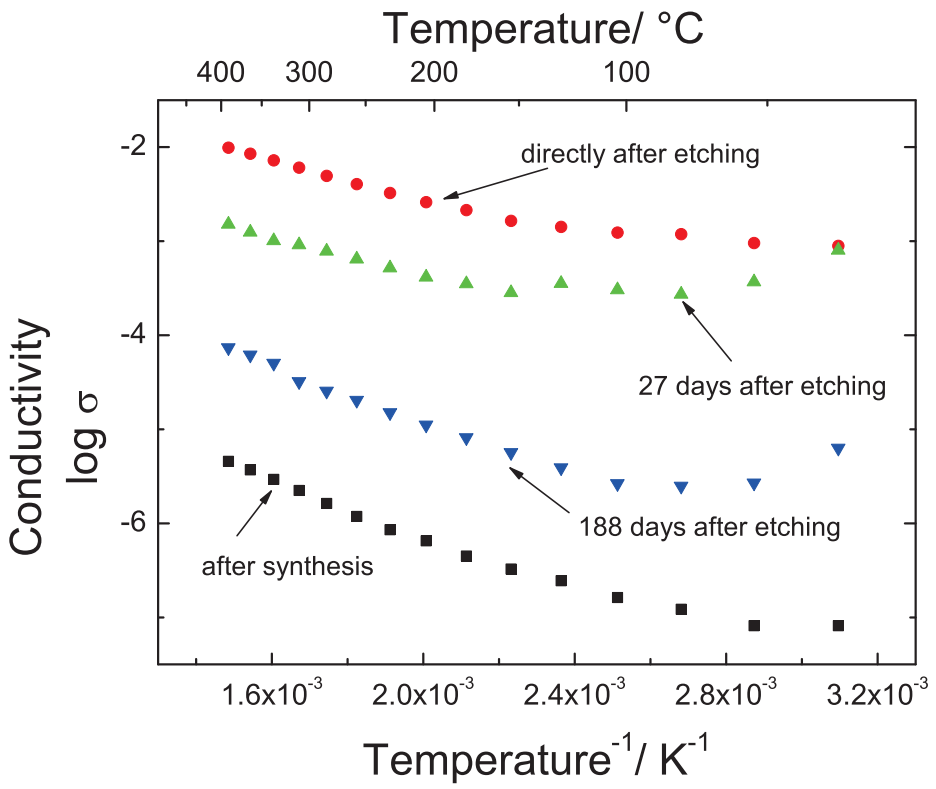

Figure 6.5: Conductivity for as-prepared and etched silicon nanoparticles as a function of the inverse temperature in hydrogen atmosphere.

particles. For the conductivity of the particles, which were stored in ambient atmosphere for 188 days, an even more decreased conductivity compared to the measurements of materials stored for 26 days can be observed. This behavior can be explained by the regrowing oxide shell and the effect, that the oxide is increasing in thickness over time [96]. The charge transport between the silicon particles is disturbed by the oxide shell. The conductivity for the etched particles stored for 188 days in air is even worse due to the growth of the oxide shell compared to the 26 days old particles. These observations are also supported by the FTIR spectra in figure 6.4. In this figure, the peaks from the oxide are reappearing again and getting stronger over time in contrast to the decreasing SiH_x peak from the hydrogen termination. The conductivity of the 188 day old sample is not reaching the low conductivity of the as-prepared particles. The EPR signal for the as-prepared

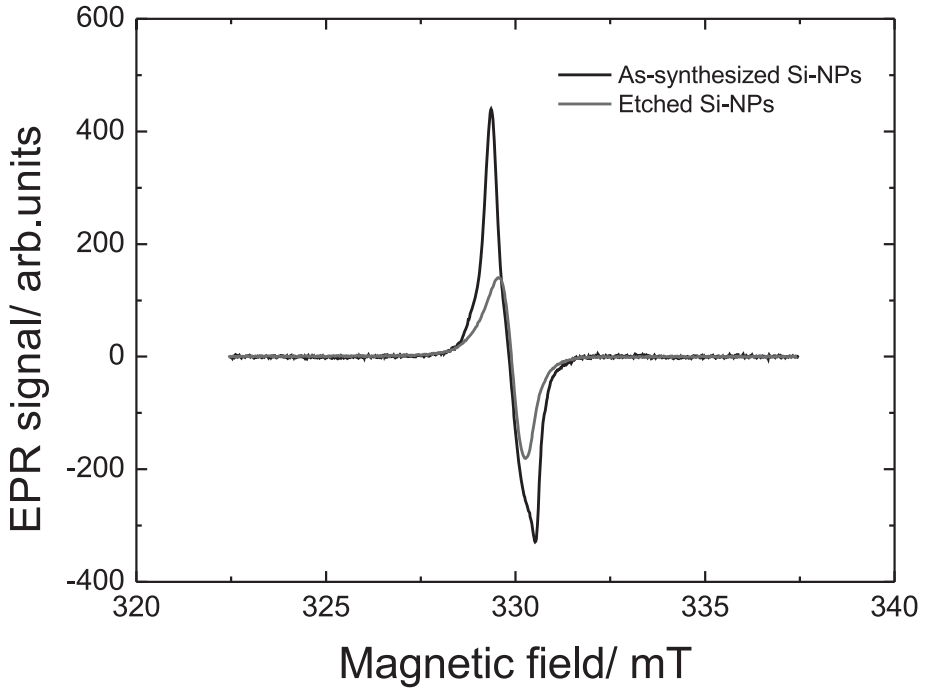

Figure 6.6: EPR measurement for as-prepared and etched silicon nanoparticles.

particles in figure 6.6 shows the dangling bond signal known from theory [97, 98] measured by electron paramagnetic resonance (EPR). For the measurements of the etched particles a strongly decreased signal can be observed (see figure 6.6). This behavior is correlated with a reduction of surface dangling bonds (Pb-centers) taking place during the etching procedure and resulting in a hydrogen-terminated particle surface. For the etched silicon nanoparticles no Pb-centers are observed but this behavior has no influence on the D-centers. This may lead to an explanation for the much higher conductivity for etched silicon nanoparticles because the etching process removes the oxide shell around the particles. The shell of as-synthesized particles has a high dangling bond concentration and hinders the

electrons to take part in the transport process in as-prepared silicon particles. Pi et. al [43] observed the opposite behavior for their etched silicon nanoparticles. This difference may come from a different particle size and especially from the different oxidation time after the etching process took place.

6.2.1 Explanation of the resistivity and capacity changes between as-prepared and etched silicon nanoparticles.

Despite the reoxidation of the freshly etched silicon nanoparticles, it is possible to distinguish between the different resistivity contributions of as-prepared and etched silicon nanoparticles. In figure 6.8 the Nyquist plot for the as-prepared silicon nanoparticles for a selection of temperatures is shown. The line in each of the semicircles represents the numerical fit to the measurements at the present temperature with an equivalent circuit diagram model. For the as-prepared silicon particles an equivalent circuit diagram consisting of two serial connected RC-elements (resistivity and capacity in parallel) and a single resistor was fitted. The mean deviation of the fit for as-prepared particles for each data point is about 1.2%. In figure 6.9 the Nyquist plot of a selection of measurement for etched particles can be seen. The line in each of these semicircles represents also the result from the fit. For the etched particles, an equivalent cirquit diagramm consisting of a single resisitor and an RC-element (the resistivity and the capacitor of the RC-element are in parallel) in series leads to the best it result.The mean deviation for this model is about 0.9% for each data point. In figure 6.7, a schematic view of the arrangement of silicon nanoparticles between the two contacts in the measurement set-up can be seen. In figure 6.7a and c, the contributions to the overall resistivity are shown for as-prepared silicon nanoparticles. The dark grey color represents the core of the silicon particles and the light grey ring around the core represents the oxide shell. The plates on each side in the pictures are the platinum contacts on both sides of the sample. The different resistivity contributions for the as-prepared silicon nanoparticles are fitted with the equivalent circuit diagram in 6.7c. The different colors of the resistivities which are represented in the equivalent cirquit show their electrical origin. The labels of the elements are as follows: c = core, p-p = particle-particle and p-e = particle-electrode contacts. In figure 6.7b, the

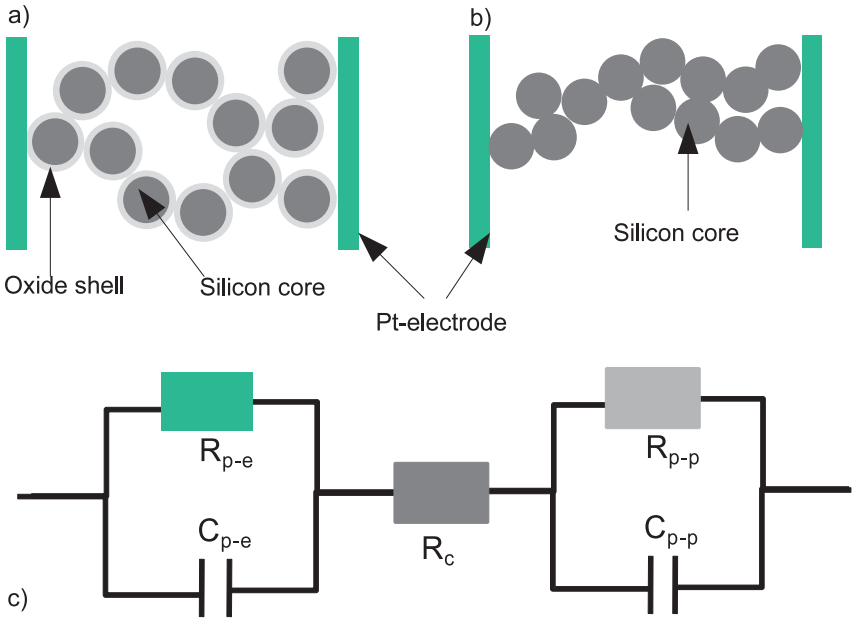

Figure 6.7: Explanation of the different resistivity contributions which occur before and after surface etching.

shematic view of the arrangement of etched silicon nanoparticles is shown which is in principal the same as for the as-prepared particles except the missing oxide shell around the particles. This arrangement could also be fitted with the same equivalent circuit as for the as-prepared particles but the resulting values are different. The capacity C of a parallel-plate capacitor is defined by equation (6.1) where ϵ_0 is the permittivity constant and ϵ_r the material permittivity multiplied with the area A and divided by the distance d of the particles [99]:

$$C = \epsilon_0 \epsilon_r \frac{A}{d}. \tag{6.1}$$

The permittivity of the silicon is an evidence for the energy storage of the electric field between the two particles. The permittivity of etched particles is much bigger than that of the as-prepared particles due to the missing oxide shell. The energy between the oxide shells is kind of storage area for the electric field. By

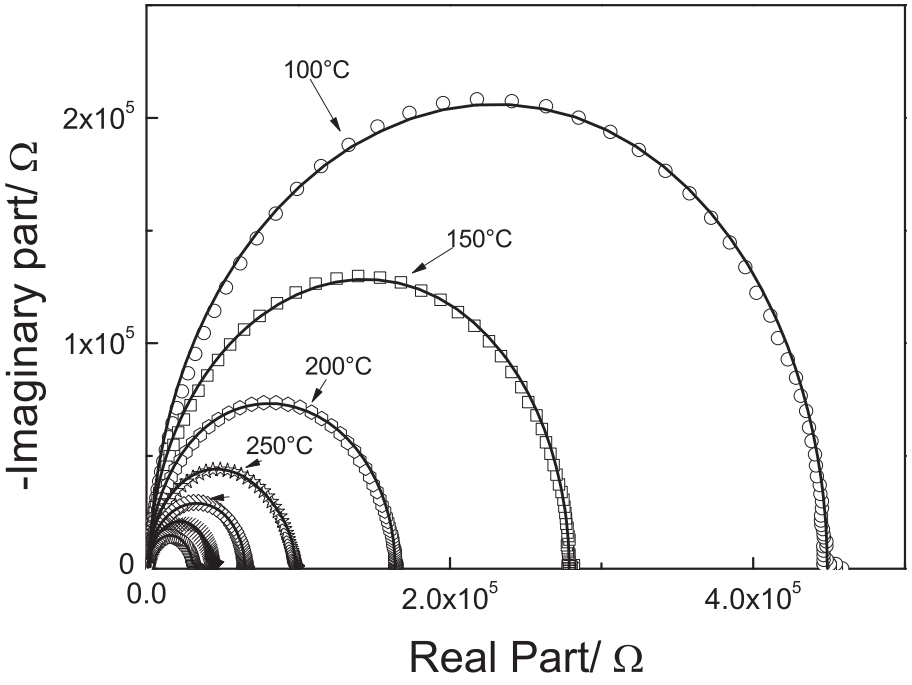

Figure 6.8: Nyquist plot of as-prepared particles and the fit of the chosen equivalent circuit diagram. The equivalent circuit diagram consists of two serial connected resistivity-capacity elements in parallel and one resistivity element.

etching the oxide shell this storage is possibly removed and the permittivity for the etched silicon nanoparticles increases. The removal of the oxide of the particles decreases also the distance between the core of two silicon nanoparticles and this increases the capacitiy of the material ($C \propto \frac{1}{d}$). Both particle ensembles (as-prepared and etched) are fitted with the same equivalent circuit diagram but the resulting values change apparently for the resistivity-capacity element which represents the particle-particle contacts. The change is coming mostly from the changing permittivity and the reduced distance between the silicon cores compared to the as-prepared particles. With this information it is possible to seperate the contribution of the resistivity of silicon nanoensembles. In general, this means that there is a substantial influence of the etching process that changes the elec-

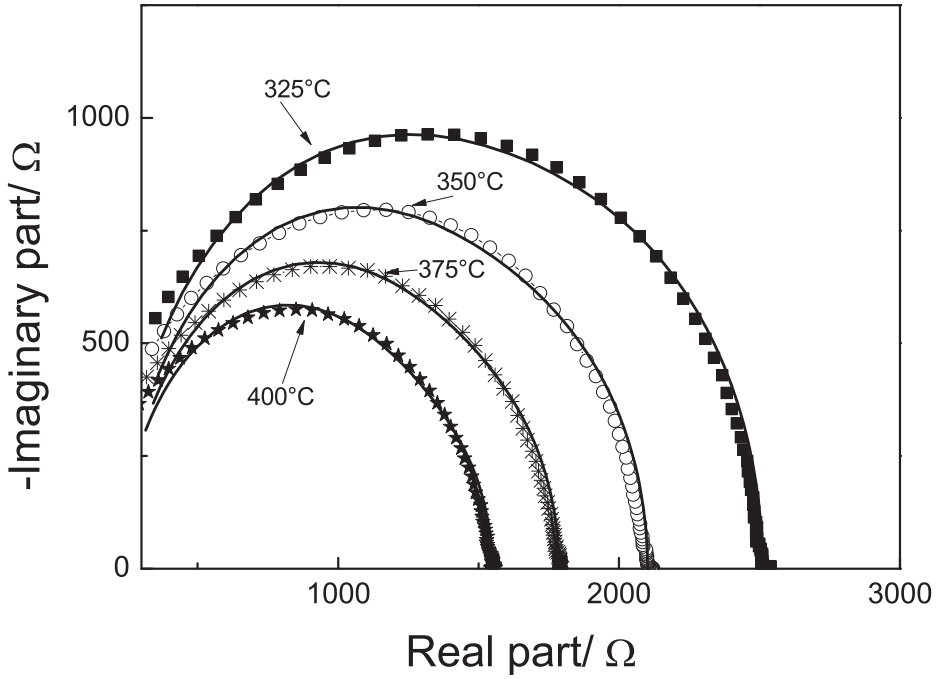

Figure 6.9: Nyquist plot of a selection of freshly etched silicon nanoparticles in hydrogen atmosphere with the calculated fit of a resistivity-capacity and one resistivity elements in series.

tric properties of silicon nanoparticles. The removal of the oxide shell decreases remarkably the overall resistivity of the silicon nanoparticles.

6.3 Transport properties of functionalized silicon nanoparticles

In chapter 6.2, the disadvantage of etched silicon nanoparticles were demonstrated very clearly. The regrowing oxide shell decreases the conductivity directly after the etching process rapidly. In this chapter, a method will be explained to avoid regrowing of the oxide shell and with this, keeping the conductivity high. For this, a diversity of organic alkenes with different lenghts are used for the functionalization process. The success of this functionalization and the influence of the lengths of the alkenes are explained. In figure 6.11, the conductivities of the silicon

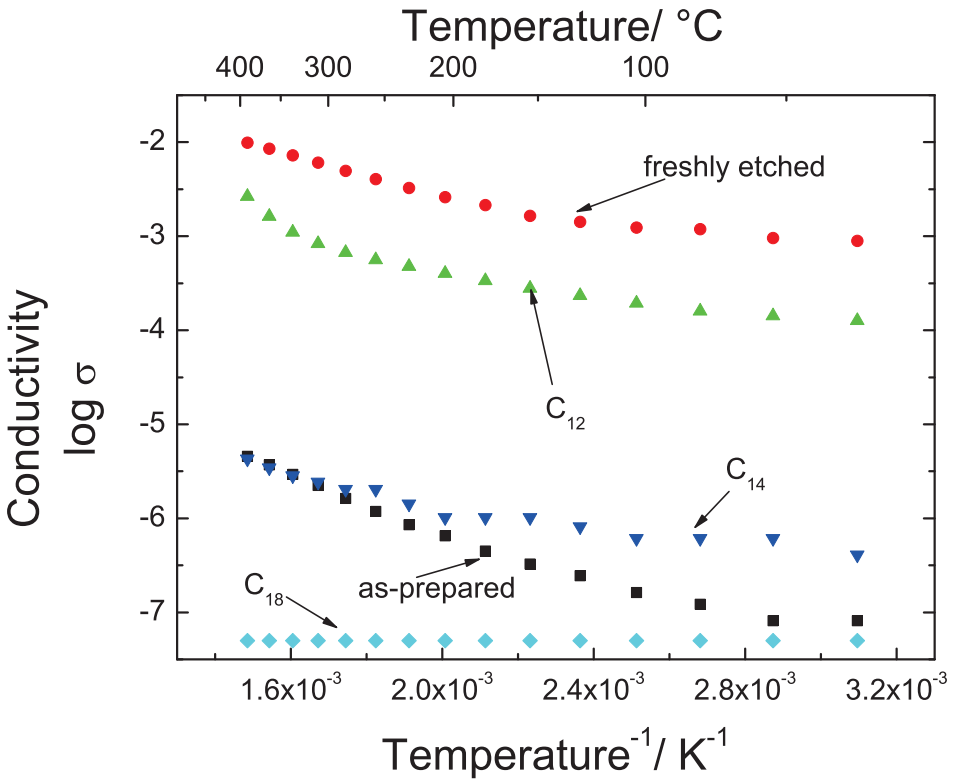

Figure 6.10: Conductivity as a function of the temperature for the silicon nanoparticles functionalized with alkenes with carbon lengths of C_{12} and longer in hydrogen atmosphere.

nanoparticles functionalized with the shorter alkene molecules (C_6, C_{10}, C_{12}) is shown as a function of the inverse temperature. In figure 6.10, the conductivities for the silicon nanoparticles functionalized with longer organic alkenes (C_{12},

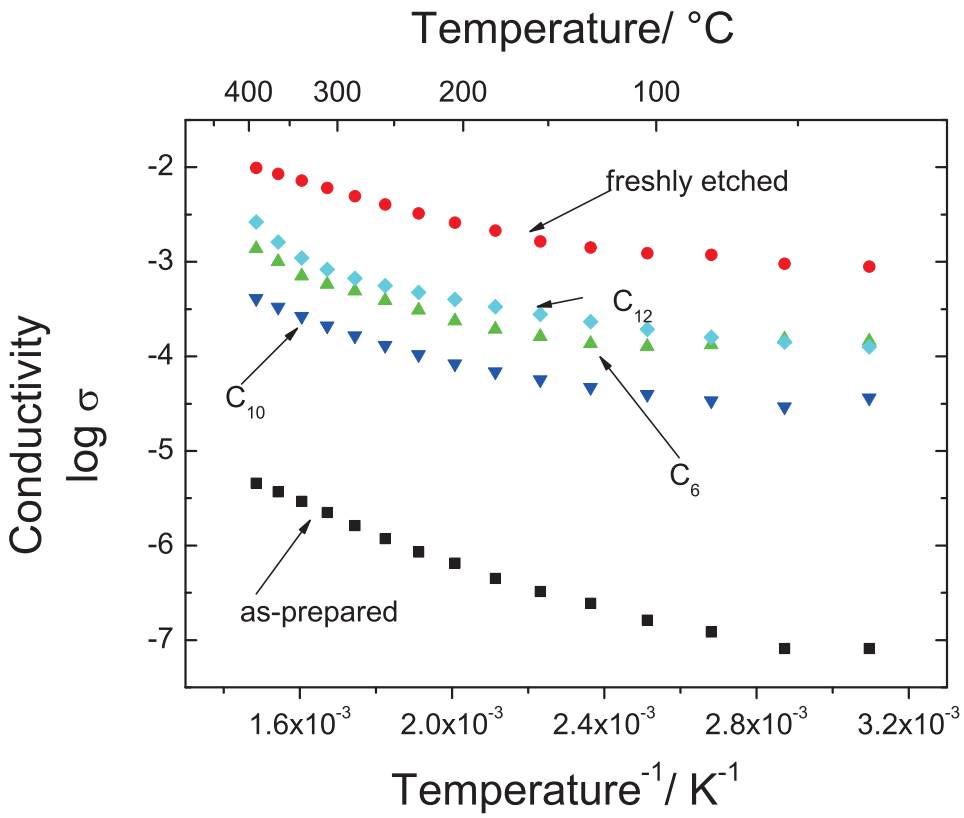

Figure 6.11: Conductivity as a function of the temperature for the silicon nanoparticles functionalized with alkenes with carbon lengths of C_{12} and shorter in hydrogen atmosphere.

C_{14}, C_{18}) are shown as a function of the inverse temperature. By comparing the particles functionalized with shorter alkenes to the values of the as-prepared and freshly etched silicon nanoparticles it is obvious, that all values for the conductivity of functionalized silicon nanoparticles are lying between these two lines. The particles functionalized with dodecene (C_{12}) have the highest conductivity compared to the hexene (C_6) and decene (C_{10}) functionalized particles. For the silicon nanoparticles with longer alkyl chains the conductivity is worse compared to silicon particles functionalized with shorter alkyl chains. For the tetradecyl (C_{14}), functionalized particles a conductivity a little higher compared to the as-prepared

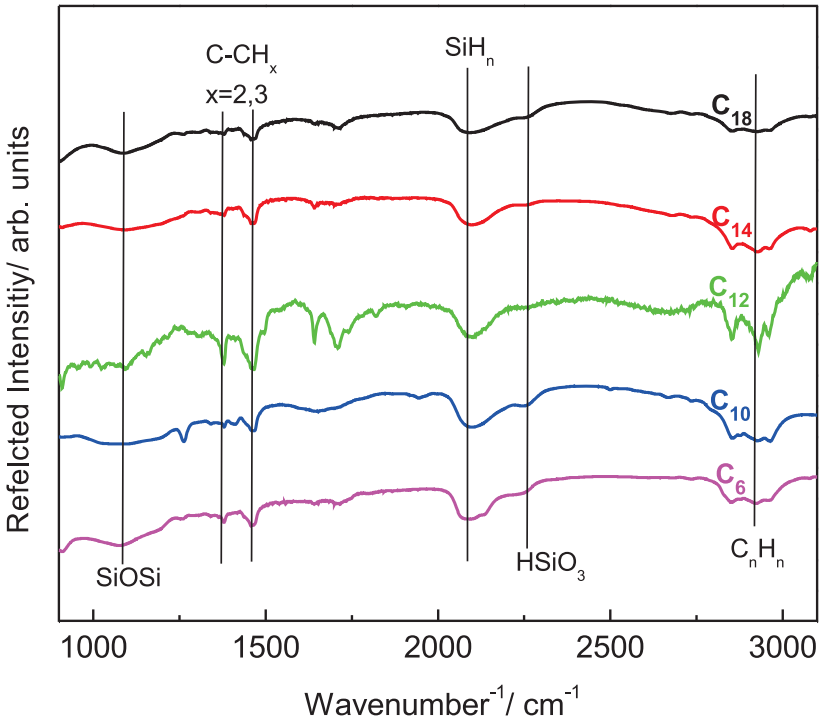

Figure 6.12: FTIR spectra of all functionalized Si-NPs directly after the functionalization process.

particles is observed and for the octadecene (C_{18}) functionalized particles the conductivity is even worse than for the as-prepared particles (the conductivity appears to be constant due to the effect that the conductivity is lower than the measurement range of the impedance spectrometer). The decrease in conductivity for all functionalized particles compared to the freshly etched ones can be explained by the effect of the organic shell around the silicon core which increases the barrier for the charge carrier transport between the particles. The particles functionalized with C_{14} and C_{18} show the lowest conductivity of all functionalized particles and are in the range of the conductivity of the as-prepared particles. The coverage of the surface of these two types of particles is quite large due to a steric hindrance of the carbon chains around the surface. This steric hindrance also allows a slight

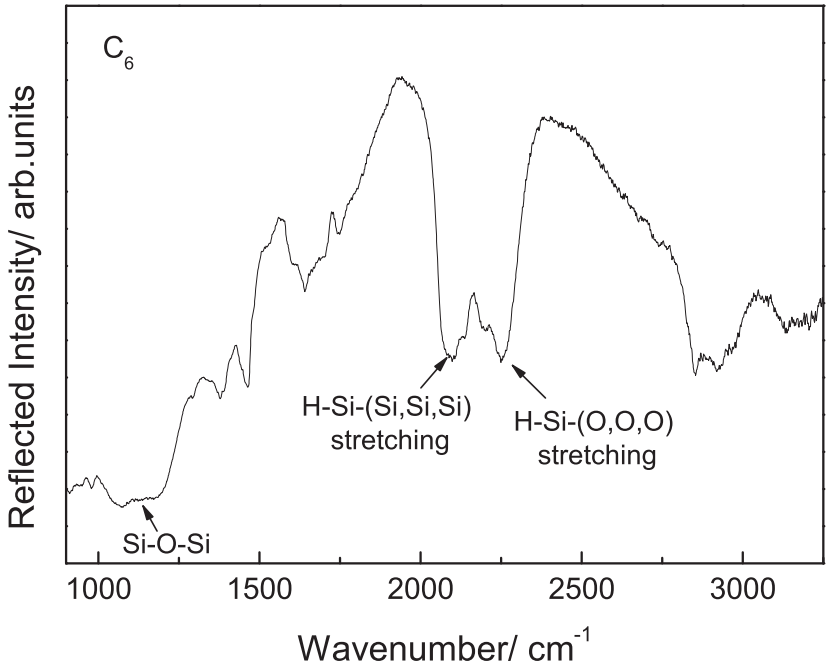

Figure 6.13: FTIR spectrum of C_6 functionalized silicon nanoparticles. The peaks which indicates the reoxidation can be clearly seen.

reoxidation of the particles due to diffusion of oxygen atoms. In figure 6.12 the FTIR spectra for all functionalized silicon particles are shown directly after the functionalization process. In the FTIR spectra for the C_{14} and C_{18} functionalized particles, a small $HSiO_3$ peak is observed which reflects a regrowing of the oxide shell [100]. The FTIR spectra for the particles functionalized with C_6 and C_{10} also show the $HSiO_3$ peak and in addition, a clearly visible Si-O-Si peak at $1100\,cm^{-1}$ (also see figure 6.13 for C_6). This behavior explains the lower conductivity for the C_{10} and C_6 functionalized particles compared to the dodecene (C_{12}) terminated particles. The FTIR spectrum for the C_{12} functionalized particles is not showing any Si-O-Si peak and also no $HSiO_3$ peak (see figure 6.12 and 6.14). The functionalization process seems to work very well for this lengths of organic alkenes (C_{12}) which can also be seen in the peaks between 1200 and $1900\,cm^{-1}$, where the peaks

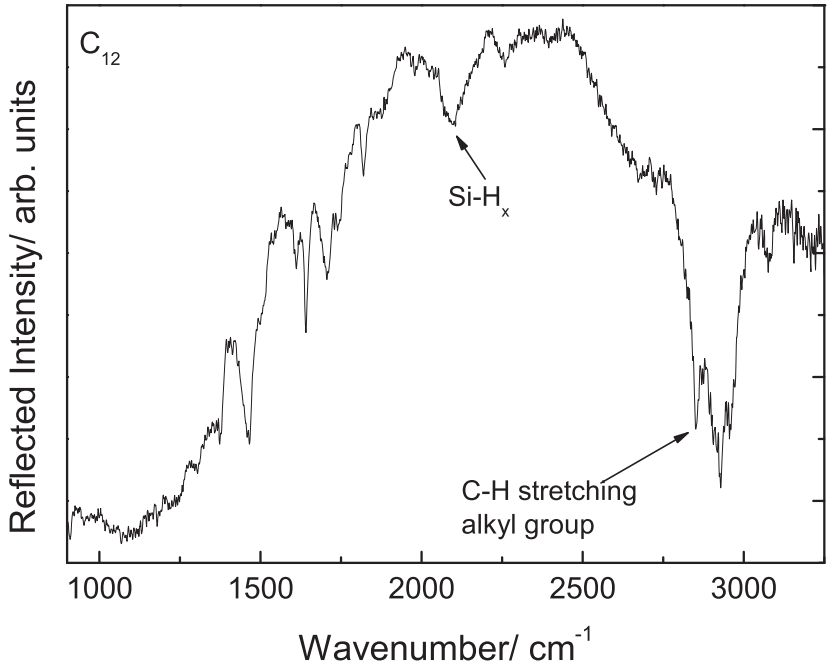

Figure 6.14: FTIR spectrum of C_{12} functionalized silicon nanoparticles. A clear peak of the alkylation process can be observed but no oxide peak.

(C-CH_x) for the functionalization with alkenes are expected. In figure 6.15, the conductivity of the freshly functionalized silicon nanoparticles with dodecyl and the same particles 188 days after the functionalization procedure (during this time they were stored in normal air) can be seen as a function of the inverse temperature. This measurement shows the stability of the dodecene terminated silicon nanoparticles which were stored in normal air for 188 days. The conductivity is decreased less than half an order of magnitude compared to the dodecene terminated particles which are measured directly after functionalization. This functionalization process using dodecene as organic alkene to prevent the reoxidation of the silicon nanoparticles is the most promising functionalization type.

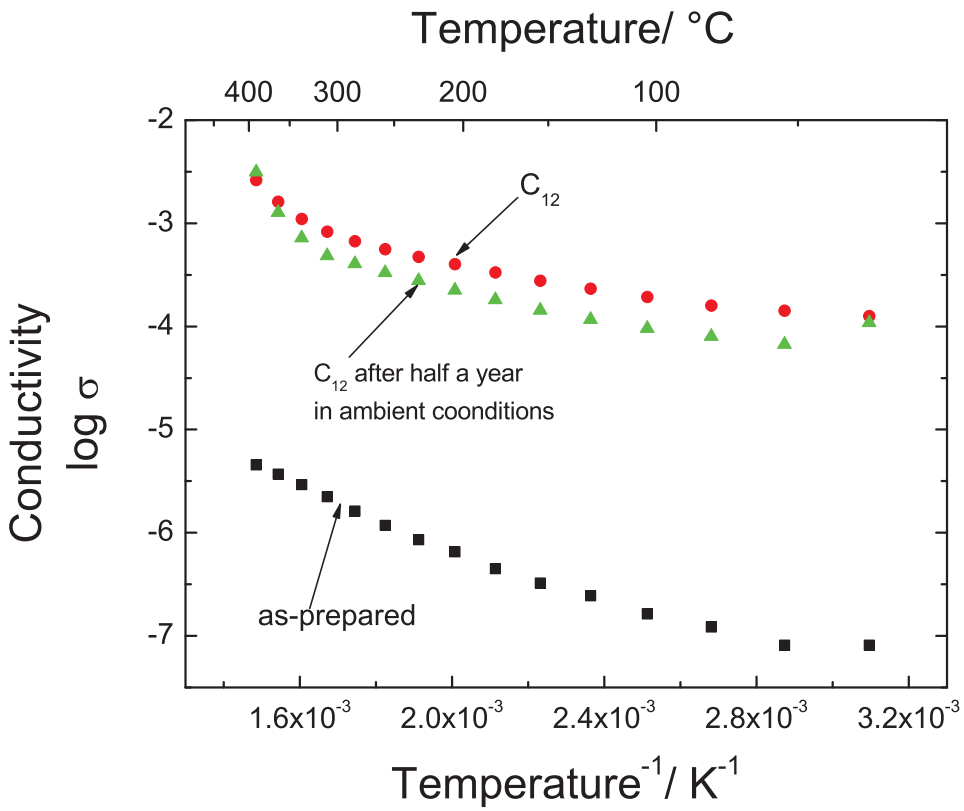

Figure 6.15: Stability of the dodecene terminated silicon nanoparticles for different times after the functionalization process in comparison to the conductivity of the unprepared silicon nanoparticles.

6.4 Variable range hopping and charge carrier transport in silicon nanoparticles

The theory of Mott is used to explain the low temperature behavior of the resistivity in disordered sytems with localized states. The possibility of hopping of electrons between two energetic states is possible when the hopping energy E_{Hop} is high enough in the system. This energy is given by the absorption of phonons and the distance of the hopping between two energetic states. This is the so called hopping distance R_{Hop}. The hopping energy ranges normally between 0.1 and 0.2 eV. The modeling of the results with the theory of Mott is the most promising for silicon nanoparticles even the measurements took place at much higher temperatures than normally used for the explanation with Mott's theory and with this the existance of localized states in the system is different. At low temperatures, the electrons prefer to take longer times for the hopping process and also travel longer distances to find energetically lower levels. In figure 6.16, the plot of $\ln(\sigma\ \sqrt{T})$ as a function of $T^{-1/4}$ can be seen. With the help of figure 6.16 and the theory of Mott's variable range hopping (VRH), it is possible to calculate the density of the local states N_{EF} and with this the hopping distance and the hopping energy [61–66]. The slope m of the plots in figure 6.16 in combination with a dimensionless constant λ_{vrh}, the spatial extension α of the wave function $\exp(-\alpha R)$ and the Boltzmann constant k_B leads to equation (6.2) to calculate the density of the local states:

$$N_{\mathrm{EF}} = \frac{\lambda_{\mathrm{vrh}}\alpha}{k_{\mathrm{B}}m^4}. \tag{6.2}$$

The hopping distance R_{Hop} and the hopping energy E_{Hop} are calculated with the equations (6.3) and (6.4):

$$R_{\mathrm{Hop}} = \left(\frac{9}{8\pi\alpha k_{\mathrm{B}} T N_{\mathrm{EF}}}\right)^{1/4}, \tag{6.3}$$

$$E_{\mathrm{Hop}} = \frac{3}{4\pi(R_{\mathrm{Hop}})^3 N_{\mathrm{EF}}}. \tag{6.4}$$

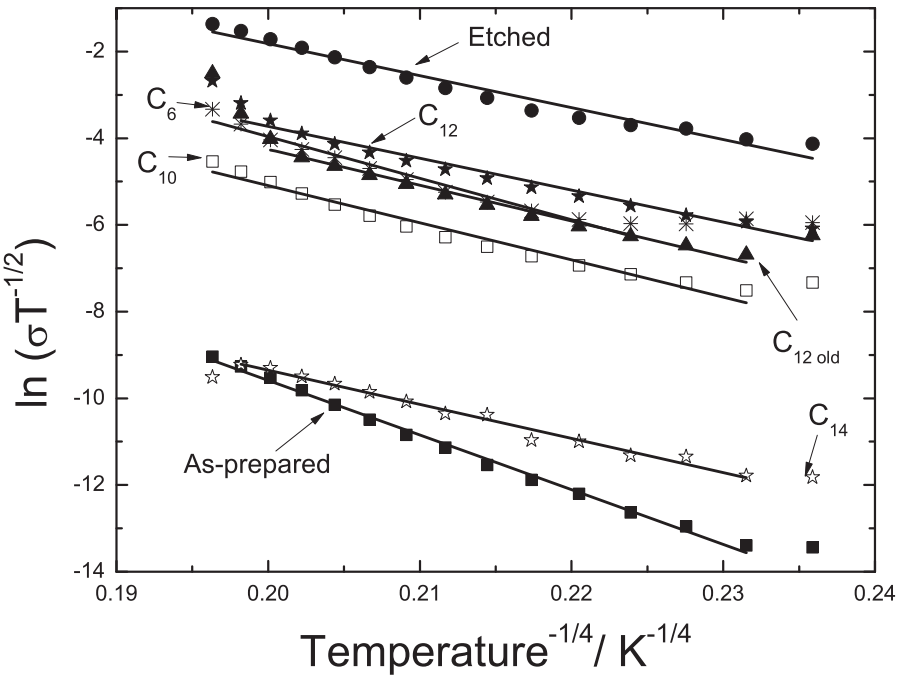

Figure 6.16: Plot of $\ln(\sigma\sqrt{T})$ as a function of $T^{-1/4}$ and the calculated slopes for each sample.

According to the paper of Mott et al. [61], the dimensionless constant λ_{vrh} is set to 16 and the degree of localization of α=$1 * 10^7 \mathrm{cm}^{-1}$. The calculated values for the density of states are shown in table 6.1. In figure 6.18, the hopping distance

Table 6.1: Densitiy of states for the different samples.

Sample	Density of states N_{EF} $(\frac{1}{J\mathrm{cm}^3})$
As-prepared	$7.34 \cdot 10^{17}$
Etched	$6.26 \cdot 10^{18}$
C_6	$2.20 \cdot 10^{18}$
C_{10}	$3.45 \cdot 10^{18}$
C_{12}	$5.26 \cdot 10^{18}$
C_{14}	$2.89 \cdot 10^{18}$
C_{12old}	$3.99 \cdot 10^{18}$

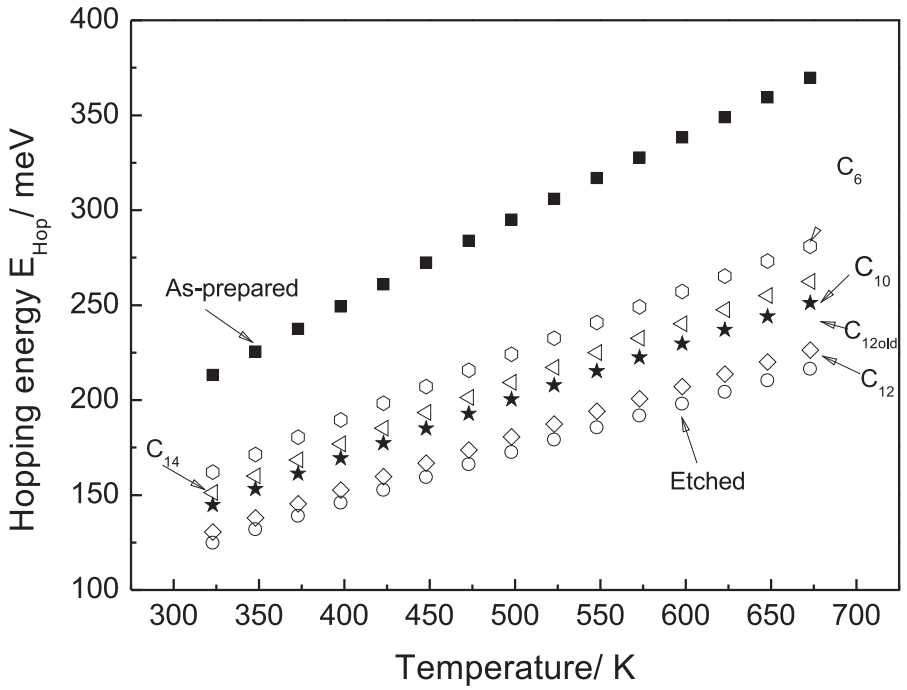

Figure 6.17: Temperature dependence of the calculated hopping energies for each sample.

as a function of the temperature can be seen. The longest hopping distances are observed for the as-prepared silicon nanoparticles. All other functionalized particles show much shorter hopping distances. In figure 6.17, the hopping energy is shown as a function of the temperature for all samples. With the influence of the hopping distance, it is not surprising that the hopping energies for the as-prepared particles are the highest. These results are in agreement with the postulation of Davis and Mott [61], where the calculated values for the hopping energy must be greater than $k_{\mathrm{B}}T$. The conductivity of the material depends on the amount of free charge carriers and the mobility. The mobility is given by the hopping processes while the charge carrier concentration depends on the amount of defects in the material. For the as-prepared silicon nanoparticles the hopping distances and

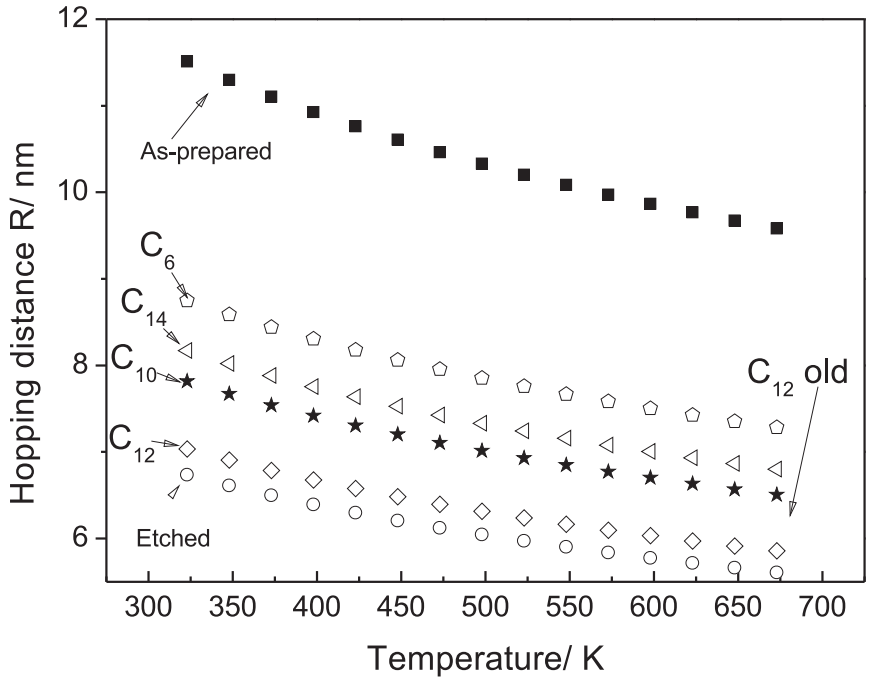

Figure 6.18: Hopping distance as a function of the temperature for as-prepared, etched and the functionalized samples.

energies are the highest of all measured samples (see figure 6.17). The oxide shell around the particles has a thickness of about 2 nm and the amount of defects is quite high. After the etching process the oxide shell and therefore the most defects are removed and with this the hopping barrier is decreased which results in a higher conductivity and lower hopping distances and energies. The hopping distances for all functionalized particles are presented in figure 6.19 at 50 °C. The hopping distance for the as-prepared silicon nanoparticles is the highest with about 11 nm. The distance itself is a contribution of the oxide shells of the two particles between which the hopping process takes place. The hopping distance does not need to be the shortest but the energetically lowest. This is the reason for the hopping distance of 11 nm for as-prepared particles and not just the hopping distance of the addition of the thickness of the oxide shell of the two particles. The etched

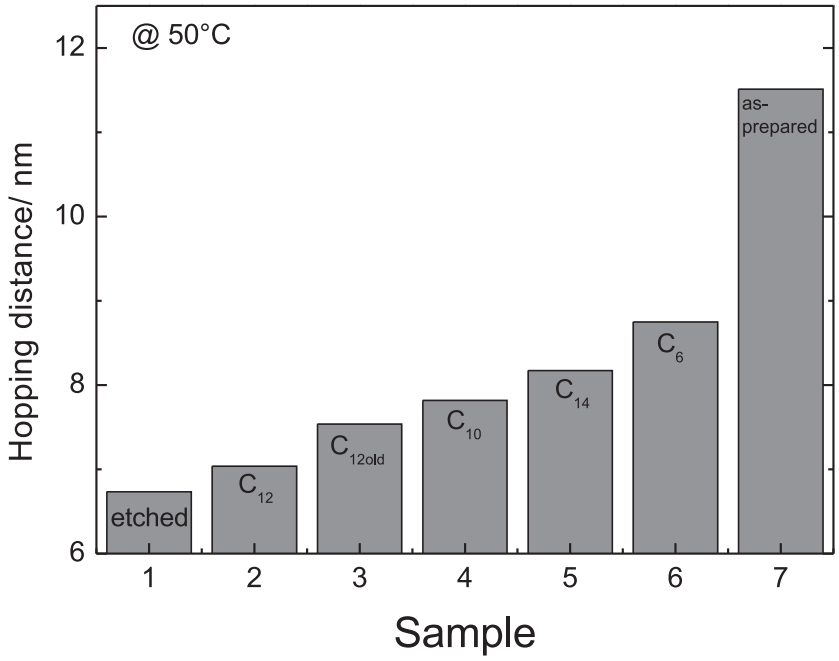

Figure 6.19: Hopping distance of the silicon nanoparticles for the different samples at 50°C

silicon nanoparticles have the lowest hopping distance of about 6.5 nm due to the missing oxide shell around the surface of the silicon nanoparticles. If one compares the hopping distances between as-prepared and etched silicon nanoparticles, it is striking that the difference between them is the sum of the thickness of the two oxide shells. All functionalized silicon nanoparticles have longer hopping distances than the etched particles. The C_6, C_{10} and C_{14} functionalized particles have longer hopping distances compared to the dodecene (C_{12}) terminated particles. This effect occurs because the oxide shell is regrowing for the particles which are functionalized which alkenes (see figure 6.12). The hopping distances and energies are a little bit higher for the dodecene functionalized particles stored half a year in normal air (C_{12old}) due to the coverage of the surface with dodecene. The increased hopping distance of the C_{12} terminated particles, which was measured after half a year again, is a result of a very slow reoxidation process. The hopping energy is the

same because it is only dependent on the calculated hopping distance (see equation (6.4)).

7 Summary

Nanomaterials are investigated in detail due to their outstanding chemical and physical properties compared to bulk material. Their properties can be tuned by, e.g., changing their size or composition or by exposing them to different gases or temperatures. This work deals with zinc oxide (ZnO) and silicon (Si) nanoparticles, to show their possible applications in electronic devices. Transparent conductive oxides (TCO) are optically transparent and electrically conductive. The most often used TCO materials are indium tin oxide (ITO) and ZnO but indium is expensive and it should be replaced by more abundant and thus less expensive material. Aluminum-doped ZnO nanoparticles are a promising alternative for ITO due to the already well-characterized optical properties. However, the electronic properties of ZnO nanoparticles as TCO have not been investigated in detail before. Therefore, the electrical transport mechanism of ZnO nanoparticles was investigated and a device made of ZnO nanoparticles via ink-jet printing was produced as a demonstrator for an electronic application. The electrical properties of mechanically compacted pellets prepared from nanosized ZnO powders are investigated using impedance spectroscopy. The impedance of the samples is measured in hydrogen and in synthetic air between room temperature and 400°C. In both atmospheres, the measurements show two different electrical transport processes depending on the temperature and the doping level. The resulting conductivity in hydrogen atmosphere for undoped ZnO nanoparticles is two orders of magnitudes higher than for the measurements in synthetic air. By investigating the doping of the ZnO with Al, the best parameters can be found to replace ITO in the future. Because of this, one part of this thesis deals with the electrical properties of ZnO nanoparticles with varying Al-concentrations and in different atmospheric conditions. In air, the ZnO particles show a lower conductivity than in hydrogen atmosphere due to the generation of free electrons in hydrogen atmosphere. In air, the electrical conductivity increases with rising Al concentrations between 5.39-

7.74% of Al. With higher Al concentrations, the conductivity goes down due to a strongly decreased crystallinity of the ZnO particles. In hydrogen atmosphere the conductivity of the doped ZnO nanoparticles decreases with higher Al concentrations. The decreasing conductivity for higher Al concentration in hydrogen atmosphere results from strongly increased scattering processes between the charge carriers due to high carrier concentration in the hydrogen atmosphere.

The influence of moisture in the environment was also investigated for the ZnO nanoparticles. Increased conductivity with increasing moisture was already well known, but the reversibility regarding the change of the surrounding atmosphere has not been investigated before. It was found, however, that the conductivity of ZnO nanoparticles stays at high even after completely removing moisture from the atmosphere. This effect can be described by a non-reversible growth of the ZnO nanoparticles in the presence of moisture and this behavior is important to know in the case of using ZnO nanoparticles in electronic application in non-vacuum conditions.

To replace ITO in applications, transparent conductive layers with good electrical and optical properties are required. ZnO dispersions are prepared and printed on pre-structured substrates by ink-jet printing to investigate the electrical and sensing properties of printed films. An ink-jet printed hydrogen sensor was fabricated from a stable ZnO dispersion which showed a good sensitivity for hydrogen. The resulting conductivity in hydrogen atmosphere is about five times higher already at room temperature (at 177 Hz (ohmic behavior)) compared to the measurements in air. This simple fabricated ink-jet-printed sensor showed great potential for applications as a hydrogen sensor.

Silicon is one of the most abundant material in the world and has the advantage that it is already very well established in the microelectronics technology [23]. One of the major challenges with respect to these applications is to stabilize the silicon particles against oxidation. Silicon nanoparticles have the big disadvantage of a very poor conductivity due to the stable oxide shell around the Si core and therefore, electrical investigations of Si nanoparticles are rare. Etched Si nanoparticles have a much higher conductivity than the as-prepared material, but a stable surface functionalization to avoid a reoxidation of the particles has not been found

yet. Therefore, the main aim was to characterize the electrical properties of Si nanoparticles with different surface modifications to find a good candidate for a stable surface modification of the etched Si nanoparticles which electrical conductivity is still well enough for electronic applications. When the native oxide shell of the as-prepared Si nanoparticles is removed, a re-oxidation of the silicon nanoparticles can be observed after a few hours from measurements of the electrical properties. Surface functionalization with organic ligands can prevent or decrease oxidation. A fast and efficient process to functionalize silicon nanoparticles with n-alkenes was introduced in this work. The used Si nanoparticles were synthesized from the gas phase in a microwave plasma-reactor and have an average size of about 50 nm. The Si particles were etched in hydrofluoric acid and functionalized with alkenes of various chain lengths. The electrical properties of these different Si particles were investigated by using impedance spectroscopy. The etched Si particles have the highest conductivity and the C_{18} terminated and the as-prepared particles the lowest conductivity. The chain length of the alkenes used for surface functionalization varied between C_6 (hexene) and C_{18} (octadecene). For the functionalized Si nanoparticles, a dependence of the conductivity regarding the lengths of the used alkenes could be observed. The particles functionalized with alkenes longer than C_{12} showed poor conductivity. Obviously, in these cases, the surface coverage becomes too thick for efficient transport of charge carriers and in addition, a regrowing of the oxide shell after only one day was observed with FTIR measurements. It seems that in the case for longer alkenes, steric hindrances of the ligands occurs which allows for oxygen transport towards the surface possible. For the Si particles functionalized with alkenes shorter than C_{12}, a reduced conductivity compared to the particles functionalized with C_{12} was observed. FTIR measurements showed a fast reoxidation of the Si particles functionalized with C_6 and C_{10} which results in the strongly reduced conductivity. The best results showed the Si particles functionalized with C_{12} and compared to the conductivity of the freshly etched Si particles, the conductivity is about one order of magnitude lower. The C_{12}-functionalized particles were stable for at least half a year at ambient conditions which is a very promising result for the search of a surface stabilization of Si nanoparticles. The transport processes in the silicon ensembles can be described by a variable range hopping transport process and the hopping

distances are calculated and compared with the thickness of the surface coverage (oxide shell or organic alkenes), which are comparable with the hopping distances of the charge carriers.

The electrical properties of the investigated ZnO and Si nanoparticles were investigated successfully. The electrical properties of ZnO nanoparticles doped with aluminum were shown. In atmosphere with variable hydrogen content, the electrical conductivity can be tuned until the semiconducting behavior of the ZnO reaches metallic transport behavior. The non-reversibility of conductivity and size of ZnO nanoparticles in moist atmosphere must be considered when using ZnO in applications where the material is exposed to moisture. An ink-jet-printed ZnO film on a sensor structure was prepared and tested successfully in air and in hydrogen atmosphere and demonstrated the great potential to use ZnO films as hydrogen sensors.

The characterization of the electrical properties of Si nanoparticles with different surface modification was demonstrated and a surface modifications was found to keep the conductivity of the particles high and prevent them from reoxidation. A stable surface modification was received by etching the particles and functionalize them with dodecene (C_{12}). The dodecene-functionalized Si nanoparticles showed the best long-term stability of more than half a year and the conductivity remains high. Hence, this functionalization can be used to prevent aging of Si nanoparticle-based electronic devices from oxidation.

The detailed investigation of the two nanomaterial systems provided in this work significantly contributed to promote the applicability of nanoparticles in electronic applications.

Bibliography

1. Higher-capacity lithium-ion batteries. *Technology Review* **22** (2006).
2. New nanotechnology products hitting the market at the rate of 3-4 per week. *ScienceDaily* **25** (2008).
3. Schmidt-Mende, L. & MacManus-Driscoll, J. ZnO - nanostructures, defects, and devices. *Mater. Today* **10,** 40–48 (2007).
4. Law, M., Greene, L., Johnson, J., Saykally, R. & Yang, P. Nanowire dye-sensitized solar cells. *Nat. Mater.* **4,** 455–459 (2005).
5. Goebbert, C., Nonninger, R., Aegerter, M. A. & Schmidt, H. Wet chemical deposition of ATO and ITO coatings using crystalline nanoparticles redispersable in solutions. *Thin Solid Films* **351,** 79–84 (1999).
6. Rakhshani, A. E., Makdisi, Y. & Ramazaniyan, H. A. Electronic and optical properties of fluorine-doped tin oxide films. *J. Appl. Phys.* **83,** 1049–1057 (1998).
7. Bamiduro, O., Mustafa, H., Mundle, R., Konda, R. B. & Pradhan, A. K. Metal-like conductivity in transparent Al:ZnO films. *Appl. Phys. Lett.* **90,** 252108–3 (2007).
8. Gordon, R. *MRS Bulletin* **25,** 52–57 (2000).
9. Fortunato, E., Ginley, D., Hosono, H & Paine, D. *MRS Bulletin* **32,** 242 (2007).
10. Bhosle, V., Tiwari, A. & Narayan, J. Metallic conductivity and metal-semiconductor transition in Ga-doped ZnO. *Appl. Phys. Lett.* **88,** 032106–3 (2006).
11. Minami, T. Present status of transparent conducting oxide thin-film development for Indium-Tin-Oxide (ITO) substitutes. *Thin Solid Films* **516,** 5822–5828 (2008).

12. Berry, J., Ginley, D. & Burrows, P. Organic light emitting diodes using a Ga:ZnO anode. *Appl. Phys. Lett.* **92** (2008).

13. Ho, P. *et al.* Molecular-scale interface engineering for polymer light-emitting diodes. *Nature* **404,** 481–484 (2000).

14. Kim, H. *et al.* Doped ZnO thin films as anode materials for organic light-emitting diodes. *Thin Solid Films* **420-421,** 539–543 (2002).

15. Masato, S., Masatoshi, H., Susumu, K. & Hiroyasu, S. Characteristics of Indium-Tin-Oxide/Silver/Indium-Tin-Oxide Sandwich Films and Their Application to Simple-Matrix Liquid-Crystal Displays. *Jpn. J. Appl. Phys.* **40,** 3332–3336 (2001).

16. Feng, T., Ghosh, A. & Fishman, C. Efficient electron-beam-deposited ITO/-n-Si solar cells. *J. Appl Phys.* **50,** 4972–4974 (1979).

17. Valle, G., Hammer, P., Pulcinelli, S. & Santilli, C. Transparent and conductive ZnO:Al thin films prepared by sol-gel dip-coating. *J. Eur. Ceram. Soc.* **24,** 1009–1013 (2004).

18. Baruwati, B., Kumar, D. & Manorama, S. Hydrothermal synthesis of highly crystalline ZnO nanoparticles: A competitive sensor for LPG and EtOH. *Sens. Actuators B* **119,** 676–682 (2006).

19. Liao, L. *et al.* Size Dependence of Gas Sensitivity of ZnO Nanorods. *J. Phys. Chem. C* **111,** 1900–1903 (2007).

20. Hartner, S., Khalil, A., Ali, M., Winterer, M. & Wiggers, H. Ink-jet printed ZnO nanoparticles thin film for sensing applications. **2,** 535–537 (2010).

21. Khalil, A. *et al.* Stable aqueous dispersions of ZnO nanoparticles for ink-jet printed gas sensors. *Proceedings IEEE,* 440–441 (2010).

22. Meyers, S. *et al.* Aqueous inorganic inks for low-temperature fabrication of ZnO TFTs. *J. Am. Chem. Soc.* **130,** 17603–17609 (2008).

23. Jaroniec, M. Silicon beyond the valley. *Nat. Chem.* **1,** 166–166 (2009).

24. Niesar, S., Dietmueller, R., Nesswetter, H., Wiggers, H. & Stutzmann, M. Silicon/organic semiconductor heterojunctions for solar cells. *Physica Status Solidi (A) Applications and Materials* **206,** 2775–2781 (2009).

25. Kortshagen, U., Liu, C.-Y. & Holman, Z. Hybrid solar cells from P3HT and silicon nanocrystals. *Nano Lett.* **9,** 449–452 (2009).

26. Canham, L. Optoelectronics: Gaining light from silicon. *Nature* **408,** 411–412 (2000).

27. Park, N.-M., Kim, T.-S. & Park, S.-J. Band gap engineering of amorphous silicon quantum dots for light-emitting diodes. *Appl. Phys. Lett.* **78,** 2575–2577 (2001).

28. Weigel, K. & Dreyer, R. Zinc oxide - Production, market and applications. *World of Metallurgy - ERZMETALL* **61,** 314–317 (2008).

29. Gupta, T. Application of zinc oxide varistors. *J. Am. Ceram. Soc.* **73,** 1817–1840 (1990).

30. Tsukazaki, A. *et al.* Repeated temperature modulation epitaxy for p-type doping and light-emitting diode based on ZnO. *Nat. Mater.* **4,** 42–46 (2005).

31. Hammarberg, E., Prodi-Schwab, A. & Feldmann, C. Microwave-assisted polyol synthesis of aluminium- and indium-doped ZnO nanocrystals. *J. Colloid. Interface. Sci.* **334,** 29–36 (2009).

32. Ali, M. & Winterer, M. ZnO Nanocrystals: Surprisingly Alive. *Chem. Mat.* **22,** 85–91 (2010).

33. Calvert, P. Inkjet Printing for Materials and Devices. *Chem. Mat.* **13,** 3299–3305 (2001).

34. Tekin, E., Smith, P. & Schubert, U. Inkjet printing as a deposition and patterning tool for polymers and inorganic particles. *Soft Matter* **4,** 703–713 (2008).

35. Lu, J. G. *et al.* Structural, optical, and electrical properties of (Zn,Al)O films over a wide range of compositions. *J. Appl. Phys.* **100,** 073714–11 (2006).

36. Hidayat, D., Ogi, T. & Iskandar, K. F.and Okuyama. Single crystal ZnO:Al nanoparticles directly synthesized using low-pressure spray pyrolysis. *Mat. Sci. Eng. B-Solid* **151,** 231–237 (2008).

37. Howatt, G. N., Breckenridge, R. G. & Brownlow, J. M. Fabrication of thin ceramic sheets for capacitors. *J. Am. Ceram. Soc.* **30,** 237–242 (1947).

38. Shen, W., Zhao, Y. & Zhang, C. The preparation of ZnO based gas-sensing thin films by ink-jet printing method. *Thin Solid Films* **483,** 382–387 (2005).

39. Lee, S. *et al.* Optical properties of silicon nanoparticles by ultrasound-induced solution method. *Japanese Journal of Applied Physics, Part 2: Letters* **43,** L784–L786 (2004).

40. Liu, W. *et al.* Annealing temperature dependent electrical and optical properties of ZnO and MgZnO films in hydrogen ambient. *Appl. Surf. Sci.* **255,** 6745–6749 (2009).

41. Buriak, J. High surface area silicon materials: Fundamentals and new technology. *Phil. Trans. R. Soc. A* **364,** 217–225 (2006).

42. Gelloz, B., Kojima, A. & Koshida, N. Highly efficient and stable luminescence of nanocrystalline porous silicon treated by high-pressure water vapor annealing. *Appl. Phys. Lett.* **87,** 1–3 (2005).

43. Pi, X. D., Mangolini, L., Campbell, S. A. & Kortshagen, U. Room-temperature atmospheric oxidation of Si nanocrystals after HF etching. *Phys. Rev. B* **75,** 085423– (2007).

44. Ledoux, G., Gong, J. & Huisken, F. Effect of passivation and aging on the photoluminescence of silicon nanocrystals. *Appl. Phys. Lett.* **79,** 4028–4030 (2001).

45. Li, X., He, Y., Talukdar, S. & Swihart, M. Process for preparing macroscopic quantities of brightly photoluminescent silicon nanoparticles with emission spanning the visible spectrum. *Langmuir* **19,** 8490–8496 (2003).

46. Stegner, A. *et al.* Electronic transport in phosphorus-doped silicon nanocrystal networks. *Phys. Rev. Lett.* **100,** – (2008).

47. Gupta, A., Swihart, M. & Wiggers, H. Luminescent colloidal dispersion of silicon quantum dots from microwave plasma synthesis: Exploring the photoluminescence behavior across the visible spectrum. *Adv. Funct. Mater.* **19,** 696–703 (2009).

48. Brook, A. & Yu, Z. Reactions of amines with silenes and acylsilanes. *Organometallics* **19,** 1859–1863 (2000).

49. Li, X., He, Y. & Swihart, M. Surface Functionalization of Silicon Nanoparticles Produced by Laser-Driven Pyrolysis of Silane followed by HNO3 Etching. *Langmuir* **20,** 4720–4727 (2004).

50. Reboredo, F. & Galli, G. Theory of alkyl-terminated silicon quantum dots. *J. Phys. Chem. B* **109,** 1072–1078 (2005).

51. Gupta, A. & Wiggers, H. Surface chemistry and photoluminescence property of functionalized silicon nanoparticles. *Physica E* **41,** 1010–1014 (2009).

52. Buriak, J. & Allen, M. Photoluminescence of porous silicon surfaces stabilized through Lewis acid mediated hydrosilylation. *J. Lumin.* **80,** 29–35 (1998).

53. Buriak, J. *et al.* Lewis acid mediated hydrosilylation on porous silicon surfaces. *J. Am. Chem. Soc.* **121,** 11491–11502 (1999).

54. Linford, M., Fenter, P., Eisenberger, P. & Chidsey, C. Alkyl monolayers on silicon prepared from 1-alkenes and hydrogen-terminated silicon. *J. Am. Chem. Soc.* **117,** 3145–3155 (1995).

55. Boukherroub, R., Morin, S., Wayner, D. & Lockwood, D. Thermal route for chemical modification and photoluminescence stabilization of porous silicon. *Physica Status Solidi (A) Applied Research* **182,** 117–121 (2000).

56. Schmeltzer, J., Porter Jr., L., Stewart, M. & Buriak, J. Hydride, abstraction initiated hydrosilylation of terminal alkenes and alkynes on porous silicon. *Langmuir* **18,** 2971–2974 (2002).

57. Patai, S. & Rappoport, Z. *The chemistry of organic silicon compound* (John Wiley and Sons, New York, 1989).

58. Nelles, J., Sendor, D., Petrat, F.-M. & Simon, U. Electrical properties of surface functionalized silicon nanoparticles. *J. Nanopart. Res.* **12,** 1367–1375 (2010).

59. Ibach, H. & Lüth, H. *Festkörperphysik. Einführung in die Grundlagen* (-Springer, 1999).

60. Kittel, C. *Einführung in die Festkörperphysik* (Oldenbourg Wissenschaftsverlag, 2005).

61. Mott, N. & Davis, E. *Electronic process in nanocrystalline materials* (Clarendon, Oxford, 1970).

62. Mott, N. Philos. Mag. *Philos. Mag.* **22,** 961 (1975).

63. Mott, N. & Davis, E. Philos. Mag. *Philos. Mag.* **22,** 903 (1970).

64. Mott, N. *Philos. Mag.* **19,** 961 (1975).

65. Mott, N. o. *Philos. Mag.* **19,** 835 (1969).

66. Khan, Z. Electrical and optical properties of thin film of amorphous silicon nanoparticles. *Appl. Surf. Sci.* **255,** 8874–8878 (2009).

67. University, L. *Material Science 435:Photonic Materials, Lecture 24*

68. Ou, Q., Matsuda, T., Mesko, M., Ogino, A. & Nagatsu, M. Cathodoluminescence property of ZnO nanophosphors prepared by laser ablation. *Jpn. J. Appl. Phys.* **47,** 389–393 (2008).

69. Carter, C. & Norton, M. *Ceramic Materials, Part IV* 181–200 (Springer, 2007).

70. Petermann, N. *et al.* Plasma synthesis of nanostructures for improved thermoelectric properties. *J. Phys. D: Appl. Phys.* **44,** 174034 (2011).

71. Hartner, S., Ali, M., Schulz, C., Winterer, M. & Wiggers, H. Electrical properties of aluminum-doped zinc oxide (AZO) nanoparticles synthesized by chemical vapor synthesis. *Nanotechnology* **20,** 445701 (2009).

72. McDonald, J. Homogeneous Nucleation of Vapor Condensation. II. Kinetic Aspects. *Am. J. Phys.* **31,** 31–41 (1963).

73. Hinds, W. *Aerosol Technology* (Wiley-Interscience, 1999).

74. Tsantilis, S. & Pratsinis, S. Soft- and Hard-Agglomerate Aerosols Made at High Temperatures. *Langmuir* **20,** 5933–5939 (2004).

75. Lutterotti, L., Bortolotti, M., Ischia, G., Lonardelli, I. & Wenk, H.-R. Rietveld texture analysis from diffraction images. *Z. Kristallogr. Suppl.* **2007,** 125–130 (2007).

76. Albertsson, J., Abrahams, S. & Kvick, A. *Acta Crystallogr. B* **45,** 34 (1989).

77. *Software Visfit 1.0b* Universität Duisburg-Essen (1998).

78. Dobisz, E. A. *et al.* Reduction and elimination of proximity effects. *Journal of Vacuum Science & Technology B* **11,** 2733–2740 (1993).

79. Brands, M., Posth, O. & Dumpich, G. Magnetoresistance of carbon-covered Co nanowires. *Superlattices Microstruct.* **37,** 380–387 (2005).

80. Nunes, P. *et al.* Effect of different dopant elements on the properties of ZnO thin films. *Vacuum* **64,** 281–285 (2002).

81. Gedde, U. *Polymer Physics* (Springer, 1995).

82. You, J. B. *et al.* Enhancement of field emission of the ZnO film by the reduced work function and the increased conductivity via hydrogen plasma treatment. *Appl. Phys. Lett.* **94,** 262105–3 (2009).

83. Kröger, F. & Vink, H. Relations between the Concentrations of Imperfections in Crystalline Solids. **Volume 3** (eds Seitz, F. & Turnbull, D.) 307–435 (1956).

84. Arita, M., Konishi, H., Matsuda, K., Masuda, M. & Hayashi, Y. Effects of Hydrogen Introduction on Electrical and Optical Properties of Cd-doped Ge Oxide and Zn Oxide Thin Films. *Mater. Trans.* **43,** 1142–1145 (2002).

85. Zhou, Z. *et al.* Effects of dopants and hydrogen on the electrical conductivity of ZnO. *J. Eur. Ceram. Soc.* **24,** 139–146 (2004).

86. Van de Walle, C. G. Defect analysis and engineering in ZnO. *Physica B* **308-310,** 899–903 (2001).

87. Thomas, D. G. & Lander, J. J. Hydrogen as a Donor in Zinc Oxide. *J. Chem. Phys.* **25,** 1136–1142 (1956).

88. Kulwicki, B. Humidity Sensors. *J. Am. Ceram. Soc.* **74,** 697–708 (1991).

89. Tai, J.-H. W.-P.and Oh. Humidity sensing behaviors of nanocrystalline Al-doped ZnO thin films prepared by sol gel process. *J. Mater. Sci. : Mater. Electron.* **13,** 391–394 (2002).

90. Fang, F., Futter, J., Markwitz, A. & Kennedy, J. UV and humidity sensing properties of ZnO nanorods prepared by the arc discharge method. *Nanotechnology* **20,** 245502 (2009).

91. Barsan, N. & Weimar, U. Understanding the fundamental principles of metal oxide based gas sensors; the example of CO sensing with SnO 2 sensors in the presence of humidity. *J. Phys.: Condens. Matter* **15,** R813– (2003).

92. Yadav, B., Pandey, N., Srivastava, A. & Sharma, P. Optical humidity sensors based on titania films fabricated by sol-gel and thermal evaporation methods. *Meas. Sci. Technol.* **18,** 260 (2007).

93. Agmon, N. The Grotthuss mechanism. *Chem. Phys. Lett.* **244,** 456–462 (1995).

94. Kunat, M., Girol, S. G., Burghaus, U. & Wöll, C. The Interaction of Water with the Oxygen-Terminated, Polar Surface of ZnO. *J. Phys. Chem. B* **107,** 14350–14356 (2003).

95. Okamura, K., Mechau, N., Nikolova, D. & Hahn, H. Influence of interface roughness on the performance of nanoparticulate zinc oxide field-effect transistors. *Appl. Phys. Lett.* **93,** 083105–3 (2008).

96. Liptak, R., Kortshagen, U. & Campbell, S. Surface chemistry dependence of native oxidation formation on silicon nanocrystals. *J. Appl. Phys.* **106** (2009).

97. Stegner, A. R. *et al.* Doping efficiency in freestanding silicon nanocrystals from the gas phase: Phosphorus incorporation and defect-induced compensation. *Phys. Rev. B* **80,** 165326– (2009).

98. Gupta, A. *Study of Surface Modified Silicon Nanoparticles for Printable Optoelectronics* PhD thesis (University of Duisburg-Essen, 2011).

99. Küpfmüller, k., Mathis, W. & Reibinger, W. *Theoretische Elektrotechnik* (Springer, 2008).

100. Lucovsky, G., Yang, J., Chao, S. S., Tyler, J. E. & Czubatyj, W. Oxygen-bonding environments in glow-discharge-deposited amorphous silicon-hydrogen alloy films. *Phys. Rev. B* **28,** 3225– (1983).

Appendix A

List of own publications

Book chapter

1. **S. Hartner**, D. Schwesig, I. Plümel, D.E. Wolf, A. Lorke and H. Wiggers
   Electrical transport in semiconductor nanoparticle arrays: Conductivity, Sensing and Modeling.
   NanoScience and Technology, Springer 231-271 (2012)

Peer reviewed articles

1. **S. Hartner**, M. Ali, C. Schulz, M. Winterer and H. Wiggers
   Electrical properties of aluminum-doped zinc oxide (AZO) nanoparticles synthesized by chemical vapor synthesis.
   Nanotechnology, 20, 445701 (2009)
2. A.S.G. Khalil, **S. Hartner**, M. Ali, H. Wiggers and M. Winterer
   Stable aqueous dispersions of ZnO nanoparticles for ink-jet printed gas sensors.
   Journal of Nanoscience and Nanotechnology 11 (12), 10839-10843 (2011)
3. **S. Hartner**, A. Gupta and H. Wiggers
   Electrical properties of silicon nanoparticles: Influence of surface etching, surface re-oxidation and surface functionalization.
   Submitted 2012
4. **S. Hartner**, M. Ali, M. Winterer and H. Wiggers
   Electrical Properties of ZnO Nanoparticles during Annealing in Humid Atmosphere.
   Will be submitted

Conference articles

1. **S. Hartner**, A. Gupta and H. Wiggers
   Electrical properties of functionalized nanoparticles.
   Nanotech., 1, 376-378 (2010)
   ISBN: 978-1-4398-3401-5

2. **S. Hartner**, A.S.G. Khalil, M. Ali, M. Winterer and H. Wiggers
   Ink-jet printed ZnO nanoparticles thin film for sensing applications.
   Nanotech., 2, 535-537 (2010)
   ISBN: 978-1-4398-3402-2

3. A.S.G. Khalil, **S. Hartner**, M. Ali, A. Gupta, H. Wiggers and M. Winterer
   Stable aqueous dispersions of ZnO nanoparticles for ink-jet printed gas sensors.
   3rd International Nanoelectronics Conference (INEC), 440-441 (2010)
   DOI: 10.1109/INEC.2010.5424503

4. A. Gupta, **S. Hartner** and H. Wiggers
   Optical and electrical properties of silicon nanoparticles.
   3rd International Nanoelectronics Conference (INEC), 616-617 (2010)
   DOI: 10.1109/INEC.2010.5424734

Conference contributions

Talks

1. **S. Hartner**, T. Hülser, H. Wiggers and A. Lorke.
   Impedanzspektroskopie an halbleitenden Nanopartikelsystemen.
   Meeting SFB 445, September 2006 Rietzlern, Austria

2. **S. Hartner**, H. Wiggers, A. Lorke.
   Electrical properties of compacted zinc oxide nanoparticles.
   DPG Frühjahrstagung, 26.März- 30.März, 2007,Regensburg, Germany

3. **S. Hartner**, H. Wiggers, A. Lorke.
   Electrical Magnetotransport and Transport Properties of Compacted ZnO Nanoparticles.
   DPG Frühjahrstagung, 25.2- 29.2, 2008, Berlin, Germany

4. **S. Hartner**, H. Wiggers, A. Lorke.
   Electrical properties of compacted zinc oxide nanoparticles.
   Mitarbeiterworkshop SFB 455, September 2008, Duisburg, Germany

5. **Sonja Hartner**, Moazzam Ali, Markus Winterer, Hartmut Wiggers.
   Transport Properties of Compacted Al doped ZnO Nanoparticles under different Atmospheres.
   41st Heyrovsky Discussion on Electrochemical Impedance Analysis, June 15-19, 2008, Jihlava, Czech Republic

6. **S. Hartner**, M. Ali, M. Winterer, H.Wiggers.
   Electrical Transport in doped ZnO Nanoparticles.
   2nd International Symposium on Transparent Conductive Oxides, 22.10- 26.10, 2008, Hersonissos, Crete, Greece **(Best Young Scientist Oral Award)**

7. **S. Hartner**, M. Ali, M. Winterer, H.Wiggers.
   Electric transport in aluminum-doped ZnO nanoparticles under different atmospheres.
   2nd International Symposium on Transparent Conductive Oxides, 22.10- 26.10, 2008, Hersonissos, Crete, Greece

8. **Sonja Hartner**, Moazzam Ali, Markus Winterer, Hartmut Wiggers.
   Electrical Transport in doped ZnO Nanoparticles synthesized in the Gasphase.
   Nanotech 2009, 3.05-7.05, 2009, Houston, USA

9. **Sonja Hartner**, Anoop Gupta, Hartmut Wiggers.
   Influence of doping and Oxide layeron the Conductivity of Silicon Nanoparticles.
   Nanotech 2009, 3.05- 7.05, 2009, Houston, USA

10. **S. Hartner**, A. Gupta and H. Wiggers.
    Electrical Properties of Functionalized Silicon Nanoparticles.
    MRS Spring Meeting, 5.4- 9.4, 2010, San Francisco, USA

11. **Sonja Hartner**, Anoop Gupta, Hartmut Wiggers.
    Influence of doping and Oxide Layer on the Conductivity of Silicon Nanoparticles.

World Congress on Particle Technology (WCPT6), 26.4.- 29.4., 2010, Nürnberg, Germany

12. **Sonja Hartner**, Anoop Gupta, Hartmut Wiggers.
Electrical Properties of Functionalized Silicon Nanoparticles.
Nanotech 2010, 21.06- 25.06, 2010, Anaheim, USA

13. **Sonja Hartner**, Ahmed S. G. Khalil, Moazzam Ali, Markus Winterer, Hartmut Wiggers.
Ink-Jet printed ZnO Nanoparticle Thin Films for sensing applications.
Nanotech 2010, 21.06- 25.06, 2010, Anaheim, USA

14. **Sonja Hartner**.
Investigations of the Electrical Properties of Nanoparticles Synthesized in the Gas-Phase.
SFB- Abschlussmeeting, 27.09- 01.10, 2010, San Servolo, Venice, Italy

15. **Sonja Hartner** , Ahmed S. G. Khalil, Moazzam Ali, Markus Winterer, Hartmut Wiggers.
Ink-Jet printed ZnO nanoparticle Films and their Electrical Properties.
TCM 2010, 17.10- 21.10, 2010, Analipsi, Crete, Greece

16. **Sonja Hartner**, Anoop Gupta, Hartmut Wiggers.
Functionalized Silicon Nanoparticles and their Stability in different Conditions.
MRS Fall Meeting 29.11- 03.12, 2010, Boston, USA

17. **Sonja Hartner**, Moazzam Ali, Ahmed S.G. Khalil, Markus Winterer, Hartmut Wiggers.
Ink-Jet Printed ZnO Nanoparticle Thin Films on self-fabricated Interdigital Structures.
MRS Fall Meeting, 29.11- 03.12, 2010, Boston, USA

18. **S. Hartner**, R. F. Bywalez, A. Gupta, H. Wiggers.
Stabilization and electrical properties of freestanding silicon nanoparticles for electronic applications.
Nanotoday, 11.12- 15.12, 2011, Waikoloa Beach, USA

Poster

1. **S. Hartner**, K. Hitzbleck, H. Wiggers, A. Lorke.
   Synthesis and Electrical Characterisation of Phosphorus-doped Silicon Nanoparticles.
   International Workshop on Semiconducting Nanoparticles, 7.1-8.12, 2006 Duisburg, Germany

2. **Sonja Hartner**, Moazzam Ali, Hartmut Wiggers, Axel Lorke, Markus Winterer.
   Magnetotransport and Transport Properties of Compacted ZnO Nanoparticles.
   MRS Spring Meeting, 24.3- 28.3, 2008, San Francisco, USA

3. **Sonja Hartner**, Hartmut Wiggers, Moazzam Ali, Cedrik Meier, Axel Lorke.
   Magnetotransport and transport properties of mechanically compacted ZnO and GeOx Nanoparticles.
   Materials Science and Engineering, 1.09- 4.09, 2008, Nürnberg, Germany

4. **Sonja Hartner**, Cedrik Meier, Axel Lorke, Hartmut Wiggers.
   Electrical Characterization of Microwave Synthesized Germanium Nanoparticle Ensembles.
   MRS Fall Meeting, 1.12-5.12, 2008, Boston, USA

5. **Sonja Hartner**, Moazzam Ali, Markus Winterer, Hartmut Wiggers.
   Transport Processes in doped ZnO Nanoparticles under different Atmospheres.
   MRS Fall Meeting, 1.12- 5.12, 2008, Boston, USA

6. **Sonja Hartner**, Moazzam Ali, Markus Winterer, Hartmut Wiggers.
   Electrical Properties and Growth of ZnO Nanoparticles in Humid Atmosphere.
   MRS Fall Meeting, 30.11- 03.12, 2009, Boston, USA

7. **S. Hartner**, M. Ali, M. Winterer and H. Wiggers.
   Investigating Electrical Properties of ZnO Nanoparticles: Controlled "Annealing" of nanocrystals with Moisture.
   MRS Spring Meeting, 5.4-9.4, 2010, San Francisco, USA

8. **Sonja Hartner**, Moazzam Ali, Markus Winterer, Hartmut Wiggers.
   Changing Electrical Properties due to growing ZnO Particles in different Humidity Conditions.
   World Congress on Particle Technology (WCPT6), 26.4- 29.4, 2010, Nürnberg, Germany

List of other conference contributions

1. Tim Hülser, Hartmut Wiggers, **Sonja Hartner**, Axel Lorke.
   Sensing investigations of tungsten oxide nano-particle thin films using Impedance Spectroscopy.
   DPG Frühjahrstagung, 26.3-30.3, 2007, Regensburg, Germany (Poster)
2. Cedrik Meier, Stephan Lüttjohann, Matthias Offer, **Sonja Hartner**, Hartmut Wiggers, Axel Lorke.
   Silicon and Germanium Nanoparticles: Spectroscopy and Electronic Transport.
   DPG Frühjahrstagung, 25.2- 29.2, 2008, Berlin, Germany (Invited Talk)
3. Anoop Gupta, **Sonja Hartner**, Hartmut Wiggers.
   Optical and Electronic Properties of Silicon Nanoparticles.
   IEEE International NanoElectronics Conference (INEC), 3.01-8.01, 2010, Hong Kong, China (Talk)
4. A. S. G. Khalil, **Sonja Hartner**, M. Ali, H. Wiggers and M. Winterer.
   Stable Aqueous Dispersion of ZnO Nanoparticles for Ink-Jet Printed Gas Sensor.
   IEEE International NanoElectronics Conference (INEC), 3.01-8.01, 2010, Hong Kong, China (Talk)
5. A. Abdali, **Sonja Hartner**, H. Wiggers, C. Schulz.
   Molybdenum oxide nanoparticles from pressure flame synthesis for semiconductor and sensing applications.
   MRS Fall Meeting, 29.11- 03.12, 2010, Boston, USA (Talk)
6. Nils Petermann, Niklas Stein, André Becker, Benedikt Stoib, **Sonja Hartner**, Ralf Theissmann, Roland Schmechel, Martin S. Brandt, Gabi Schierning, Hartmut Wiggers.

N−type SiGe nanocomposites: Synthesis, compaction and thermoelectric properties.
EMRS Spring Meeting,09.05- 13.05, 2011, Nice, France (Talk)

7. Robert Bywalez, **Sonja Hartner**, Anoop Gupta and Hartmut Wiggers.
Freestanding, Stabilized Silicon Nanoparticles for Photovoltaic Applications.
MRS Fall Meeting, 28.11-02.12, 2011, Boston, USA (Poster)